Biophysical Journal
Article

Biophysical Society

Structural diversity of photoswitchable sphingolipids for optodynamic control of lipid microdomains

Nina Hartrampf,[1,2] Samuel M. Leitao,[3,4] Nils Winter,[1] Henry Toombs-Ruane,[1] James A. Frank,[1,5] Petra Schwille,[3] Dirk Trauner,[1,6,*] and Henri G. Franquelim[3,*]

[1]Department of Chemistry, Ludwig Maximilian University of Munich, Munich, Germany; [2]Department of Chemistry, University of Zurich, Zurich, Switzerland; [3]Cellular and Molecular Biophysics Department, Max Planck Institute of Biochemistry, Martinsried, Germany; [4]Institute for Bioengineering, École Polytechnique Fédérale de Lausanne, Lausanne, Switzerland; [5]Vollum Institute, Oregon Health & Science University, Portland, Oregon; and [6]Department of Chemistry, New York University, New York City, New York

ABSTRACT Sphingolipids are a structurally diverse class of lipids predominantly found in the plasma membrane of eukaryotic cells. These lipids can laterally segregate with other rigid lipids and cholesterol into liquid-ordered domains that act as organizing centers within biomembranes. Owing the vital role of sphingolipids for lipid segregation, controlling their lateral organization is of utmost significance. Hence, we made use of the light-induced *trans-cis* isomerization of azobenzene-modified acyl chains to develop a set of photoswitchable sphingolipids with different headgroups (hydroxyl, galactosyl, phosphocholine) and backbones (sphingosine, phytosphingosine, tetrahydropyran-blocked sphingosine) that are able to shuttle between liquid-ordered and liquid-disordered regions of model membranes upon irradiation with UV-A ($\lambda = 365$ nm) and blue ($\lambda = 470$ nm) light, respectively. Using combined high-speed atomic force microscopy, fluorescence microscopy, and force spectroscopy, we investigated how these active sphingolipids laterally remodel supported bilayers upon photoisomerization, notably in terms of domain area changes, height mismatch, line tension, and membrane piercing. Hereby, we show that the sphingosine-based (Azo-β-Gal-Cer, Azo-SM, Azo-Cer) and phytosphingosine-based (Azo-α-Gal-PhCer, Azo-PhCer) photoswitchable lipids promote a reduction in liquid-ordered microdomain area when in the UV-adapted *cis*-isoform. In contrast, azo-sphingolipids having tetrahydropyran groups that block H-bonding at the sphingosine backbone (lipids named Azo-THP-SM, Azo-THP-Cer) induce an increase in the liquid-ordered domain area when in *cis*, accompanied by a major rise in height mismatch and line tension. These changes were fully reversible upon blue light-triggered isomerization of the various lipids back to *trans*, pinpointing the role of interfacial interactions for the formation of stable liquid-ordered domains.

SIGNIFICANCE Sphingolipids are predominantly found at the plasma membrane of cells and are recurrently associated to segregated liquid-ordered domains with important cellular functions (e.g., signaling). Controlling the lateral organization of lipids within microdomains is thus of utmost significance. In this work, we took advantage of the light-triggerable *trans-cis* isomerization of azobenzene-modified acyl chains and designed novel photoswitchable sphingolipids with varying headgroups and sphingoid backbones. By combining atomic force and fluorescence microscopies, we were able to evaluate the ability of these photoswitchable lipids to reversibly alter the properties and amount of lipid domains on phase-separated model membranes by light, having identified the importance of sphingoid base functionality for a differential optical control of liquid-ordered properties by photoswitchable sphingolipids.

INTRODUCTION

Sphingolipids are a major component of eukaryotic (notably mammalian) membranes and play a crucial role in signaling inside cells (1–3). Members of this lipid class, like ceramide (Cer) or sphingomyelin (SM), have a backbone formed from sphingosine and have been widely studied in terms of their biophysical properties, behavior on membrane models, and affinity to other lipids (4–11). Another important, but less studied, class of sphingolipids is phytosphingolipids, which

Submitted September 30, 2022, and accepted for publication February 27, 2023.

*Correspondence: dirktrauner@nyu.edu or hgfranq@biochem.mpg.de

Dirk Trauner's present address is Department of Chemistry, University of Pennsylvania, Philadelphia, Pennsylvania.

Henri G. Franquelim's present address is Interfaculty Center for Bioactive Matter, Leipzig University, Leipzig, Germany.

Nina Hartrampf and Samuel M. Leitao contributed equally to this work.

Editor: Erdinc Sezgin.

https://doi.org/10.1016/j.bpj.2023.02.029

are abundant in plants and fungi (12–14). These lipids have phytosphingosine as a sphingoid base (2), a backbone with increased polarity compared with sphingosine. Sphingolipids are also largely localized in the plasma membranes of eukaryotic cells when compared with inner organelle membranes (3). Here, they are usually linked to so-called lipid rafts (15), liquid-ordered (L_o) phase domains composed of rigid lipid species (sphingolipids and saturated phospholipids) and sterols, thought to be a means by which cells organize or segregate important proteins within the membrane (16–18). In addition, sphingolipids have been shown to be distributed asymmetrically in the plasma membrane, being highly enriched on the outer leaflet (19).

From a molecular point of view, sphingolipids can form stable H-bond and hydrophobic interactions with other sphingolipids (e.g., SM) and cholesterol (Chol) (2,20). While *in vivo* such lipid interactions are assumed to be transient and lead to the formation of nanoscopic domains (21,22), these can, e.g., be observed in vitro on supported membrane model systems, as segregated rigid L_o phase microdomains embedded in a fluid bulk liquid-disordered (L_d) membrane phase (23–27). The presence of hydroxyl (–OH) groups on the backbone of sphingolipids are particularly relevant for the formation of L_o domains, as interfacial H-bonding markedly stabilizes the interactions among sphingolipids and Chol (20,28). In fact, the central role of the 3-OH moiety on the sphingosine backbone of sphingolipids, like Cer or SM, has been thoroughly scrutinized (13,29–35). Likewise, the presence of a second 4-OH hydroxyl group on phytosphingosine-based lipids, like PhCer, further strengthens H-bonding and domain thermostability (13). In contrast, hindering H-bonding by adding a methyl, ethyl, or tetrahydropyranyl (THP) group at the 3-OH hydroxyl severely affected the molecular packing and ability of those blocked sphingolipids to interact with Chol (29,36). Indeed, functionalization of the 3-OH of SM by THP greatly decreases gel-phase stability (lowering the melting temperature by 10°C), impedes tight contacts with Chol, and increases the rate of sterol desorption from vesicles containing this blocked SM analog (29).

As lipid segregation plays a crucial physiological role in biomembranes, new tools to investigate and control membrane phase properties are urgently needed. In that regard, strategies based on photopharmacology (37,38), which take advantage of the high spatiotemporal precision of light, are particularly appealing. In 2016, we reported that photoswitchable Cers (ACes), which have an azobenzene photoswitch incorporated in the lipid fatty acid chain, enable optical control of lipid raft-mimicking microdomains within synthetic membranes (39). While recent advancements demonstrated the potential of azobenzene-modified photoswitchable lipids for controlling/altering membrane properties without significant physiological perturbations (39–47), the structural diversity of these photoactive molecules is nonetheless still fairly limited. This stands in stark contrast to the impressive diversity of sphingolipids found in nature. Indeed, diverse sphingolipids can serve as docking sites for various toxins (e.g., Shiga toxin binds to Gb3 (48) or cholera toxin B binds to GM1 (49)) or can even modulate the uptake of viruses by the cells (e.g., SV40 requires GM1 as receptor (50) or HIV-1 gp120 surface protein binds to GalCer on epithelial cells (51)). Hence, controlling their lateral organization within membranes is of vital importance. An expanded palette of photoswitchable sphingolipids could therefore offer new photoresponsive *N*-acyl azobenzene sphingolipids with more complex headgroup functionalities and other types of sphingoid backbones.

In our present work, we then aimed to develop a new set of photoswitchable sphingolipids with increased functionalization and incorporate these various photoswitchable lipids (photolipids) into L_d-L_o phase-separated supported model membranes. Our main goal was to investigate the influence of these modifications on the reversible remodeling of membrane microdomains upon photoswitching, as well as on fundamental mechanical properties of lipid bilayers. To this end, we performed atomic force microscopy (AFM) combined with fluorescence confocal microscopy, following the generated changes in domain area, height, and line tension.

MATERIALS AND METHODS

Synthesis of *N*-acyl azobenzene-modified sphingolipids

A protocol for the synthesis and analysis of all photolipids can be found in the supporting material. Also, a schematic overview of all synthesis can be found on page 28 of the supporting material.

Membrane model systems

Throughout this work, small unilamellar vesicles (SUVs) and supported lipid bilayers (SLBs) were used as lipid membrane model systems. These were primarily composed by *N*-stearoyl-D-*erythro*-sphingosylphosphorylcholine (C18-SM, or simply SM), 1,2-dioleoyl-*sn*-glycero-3-phosphocholine (DOPC), and Chol, which were purchased from Avanti Polar Lipids (Alabaster, AL, USA), into which different photolipids, notably Azo-Cer, Azo-PhCer, Azo-THP-Cer, Azo-α-Gal-PhCer, Azo-β-Gal-Cer, Azo-SM, or Azo-THP-SM, were mixed. Also, native *N*-stearoyl-D-*erythro*-sphingosine (C18-Cer), D-galactosyl-β-1,1′-*N*-stearoyl-D-erythro-sphingosine (C18-β-Gal-Cer), and *N*-stearoyl-4-hydroxysphinganine (C18-PhCer) were used as controls. Unless otherwise stated, the typical lipid composition was DOPC:Chol:SM:photolipid with a 10:6.7:5:5 mol ratio. For fluorescence detection, lipid mixtures were also doped with 0.1 mol % Atto655-DOPE, purchased from ATTO Technology (Siegen, Germany).

First, all lipid stock concentrations were determined in duplicate on a Mettler-Toledo UMX2 ultrabalance (Greifensee, Switzerland) with an accuracy of ± 0.1 μg. SUVs were then obtained through bath sonication of multilamellar vesicles. Briefly, the desired lipid mixtures dissolved in choloform:methanol (7:3) were added to a glass vial, and the solvent was then evaporated using N_2 flow, followed by vacuum drying in a desiccator. Lipids were rehydrated by adding HEPES buffer (10 mM HEPES, 150 mM NaCl [pH 7.4]), reaching a final lipid concentration of 10 mM, and then vigorously vortexed forming a suspension of multilamellar vesicles. These

were then diluted to 1 mM with HEPES buffer and sonicated in an ultrasonic bath for 10–20 min until the suspension became clear, giving rise to SUVs.

SLBs were prepared by deposition and fusion of SUVs on top of freshly-cleaved mica glued on a borosilicate coverglass, as described elsewhere (39). Shortly, SUV suspensions (at 1 mM lipid concentration) were deposited in the presence of 2 mM CaCl2 on freshly cleaved mica. The samples were then incubated for 20 min at 65°C, rinsed with HEPES buffer, and allowed to slowly cool down to room temperature for at least 1 h.

UV-visible (UV-vis) spectral and size characterization of vesicles with azo-sphingolipids

The mean number-normalized diameters and monodispersity of the formed SUVs were checked via dynamic light scattering using a Zetasizer Nano ZSP (Malvern Instruments, Worcestershire, UK), with an incident wavelength of 633 nm and a backscatter detection angle of 173°. Measurements were performed at 25°C and a total lipid concentration of 100 μM using disposable polystyrene cuvettes and a thermal equilibration time of 2 min.

UV-vis spectra of the various azo-sphingolipids embedded within SUVs were collected with Hellma SUPRASIL precision quartz cuvettes (10 mm light path) on a Jasco V-650 spectrophotometer (Tokyo, Japan) before and after illumination with UV-A or blue lights. More precisely, SUV suspensions at 150 μM lipid concentration, composed of DOPC:Chol:SM:photolipid (10:6.7:7:3 mol ratio), were here utilized.

Because of the high polydispersity of the SUVs (Fig. S1), we also examined the UV-vis spectra of extruded large unilamellar vesicles with a DOPC:Chol:SM:photolipid composition (10:6.7:5:5 mol ratio). These samples were then solubilized with 0.1% (v/v) Triton X-100 to eliminate the contribution of scattering and to more easily detect a possible shift in the main azobenzene peak. Extrusion was performed on an Avestin Lipofast extruder (Ottawa, Canada) by passing the multilamellar vesicle suspensions 21 times through polycarbonate membrane filters with 100 nm pore size.

Laser scanning confocal fluorescence microscopy

Fluorescence microscopy was performed on a Zeiss LSM510 Meta laser scanning microscope (Jena, Germany) using a water immersion objective (C-Apochromat, 40 × 1.2 W UV-VIS-IR). Samples were excited with the 633 nm line of a He-Ne laser for Atto655 excitation. Images were typically recorded with 1 Airy unit pinhole and 512 × 512 pixel resolution. Image analysis was performed using Fiji software (http://fiji.sc/Fiji).

Segmentation methods

In order to quantify the lipid domain (L_o phase), the confocal data were processed by a custom-made MATLAB script for batch processing. The algorithm performs basic segmentation operations based on thresholding (Otsu's method), morphological erosion, and dilation operations. The output is an image in Portable Network Graphic format of the positive mask of the dark regions corresponding to the lipid domains and a text file containing the calculated area ratio of the domains for each image.

AFM and force spectroscopy

AFM was performed on a JPK Instruments Nanowizard Ultra (Berlin, Germany) mounted on the Zeiss LSM510 Meta laser scanning confocal microscope (Jena, Germany). High-speed and normal-speed AFM, both in AC mode, were done with USC-F0.3-k0.3 ultrashort cantilevers from Nanoworld (Neuchâtel, Switzerland) with typical stiffness of 0.3 N/m. The cantilever oscillation was tuned to a frequency of 100–150 kHz, and the amplitude was kept below 10 nm. Images were acquired with a typical 256 × 256 pixel resolution. Scan rate was set to 12.5–150 Hz for high-speed AFM (i.e., line acquisition taking 6.7–80 ms and full frames 1.7–20.5 s) and to 2–6 Hz for normal-speed AFM. All measurements were performed at room temperature. The force applied on the sample was minimized by continuously adjusting the set point and gain during imaging. Height, error, deflection, and phase-shift signals were recorded, and images were line fitted as required. Data were analyzed using JPK data processing software v.6.0.55 (JPK Instruments) and Gwyddion v.2.49 (Czech Metrology Institute, Jihlava, Czechia).

Line tension (γ) was determined as previously reported (52) using the equation by Cohen and co-workers (53):

$$\gamma = \frac{\sqrt{B_s K_s B_r K_s}}{\sqrt{B_r K_s} + \sqrt{B_s K_s}} \cdot \frac{\delta^2}{h_0^2} - \frac{1}{2} \cdot \frac{\left(J_s B_s - J_r B_r\right)^2}{\sqrt{B_r K_s} + \sqrt{B_s K_s}}, \quad (1)$$

with δ being the L_d-L_o height mismatch; h the monolayer thickness with $h_o = (h_r + h_s)/2$; B the elastic splay modulus; K the tilt modulus; and J the spontaneous curvature of the monolayer. Herein, the subscripts r and s refer to the L_o (rigid) and L_d (soft) membrane phases, respectively. For calculating the effective heights, we used the height mismatches obtained for the various samples and considered a thickness of the L_d bilayer of 3.9 nm, as measured in Fig. S7. Finally, as described by Cohen and co-workers (53) and García-Sáez et al. (52), and since the values of the elastic moduli of the model here employed are unknown, we assumed the case of flexible/soft "raft" domains with $B_r = B_s = 10$ k_BT, $K_r = K_s = 40$ mN/m, and $J_r = J_s = 0$.

Force spectroscopy measurements were performed using uncoated silicon cantilevers CSC38 from MikroMasch (Tallinn, Estonia), with a spring constant of 0.12 N/m, as previously described (54,55). Shortly, sensitivity and spring constant calibration were done via the thermal noise method. The total z-piezo displacement was then set to 300 nm, the indenting approach speed was set to 800 nm/s, the retraction speed was 200 nm/s, and the maximal setpoint was set to 5–7 nN. Force measurements were carried out at different points of the lipid bilayers. An average of 200 and 900 approach force curves per illumination state were, respectively, acquired for DOPC:Chol:Azo-THP-SM (10:6.7:10 mol ratio) and DOPC:Chol:Azo-Cer (10:6.7:10 mol ratio) SLBs. The collected curves were then baseline subtracted (offset and tilt) and corrected for cantilever bending using the JPK data processing software v.6.0.55 (JPK Instruments). Identification of the breakthrough events (and respective force values) was done using the step fit, offset, and statistical quantification functions on the JPK data processing software. Finally, the retrieved yield forces were plotted as histograms using OriginPro2015 (OriginLab, Northampton, MA, USA).

Compound switching on SUVs and SLBs

Photoswitching of the photolipid compounds was achieved using a CoolLED pE-2 LED light source (Andover, UK) for illumination at λ = 365 and 470 nm. The light source was typically operated for ~20 s at 80% power. For the UV-vis spectroscopic experiments with SUVs inside cuvettes, the light beam was guided by a fiber-optic cable directly to the cuvette top. For microscopic experiments, the light beam was guided by an optical fiber directly through the objective of the LSM510 Meta microscope via a collimator at the backport.

Statistical analysis

Statistical analysis of the collected AFM and confocal microscopy data was performed by one-way analysis of variance followed by Bonferroni comparison tests (95% confidence interval), using SigmaPlot 12.3 (Systat Software, Chicago, IL, USA). Tables showing the data information (mean, standard deviation, and sample size), as well as the recovered t statistics and p values can be found in the supporting material.

RESULTS AND DISCUSSION

Synthesis of photoswitchable sphingolipids

Inspired by the structural design of our simpler azo-Cers (ACes) (39) and more complex α-galactosyl-phytoceramides (40), we introduced five new azobenzene-modified sphingolipids, namely Azo-PhCer, Azo-THP-Cer, Azo-β-Gal-Cer, Azo-SM, and Azo-THP-SM. These photolipids featured (Fig. 1 *A*) 1) a FAAzo-4 fatty acid (37) at the *N*-acyl chain (equivalent to a Δ9 unsaturation when in the *cis*-isoform) and 2) sphingoid backbones based on naturally occurring sphingosine and phytosphingosine or hydroxyl-blocked sphingosine with a THP protecting group, as well as 3) lipid headgroups presenting either a free –OH, galactosyl, or phosphocholine moiety. For our comparative studies, Azo-Cer (previously named ACe-1) (39) and Azo-α-Gal-PhCer (40) (previously named GalACer-4), having the same FAAzo-4 moiety able to undergo *trans-cis* photoisomerization (Fig. 1 *B*), were also assessed.

The synthesis and characterization of Azo-Cer and Azo-α-Gal-PhCer were reported elsewhere (39,40). Azo-PhCer was prepared analogously to Azo-Cer by the coupling of

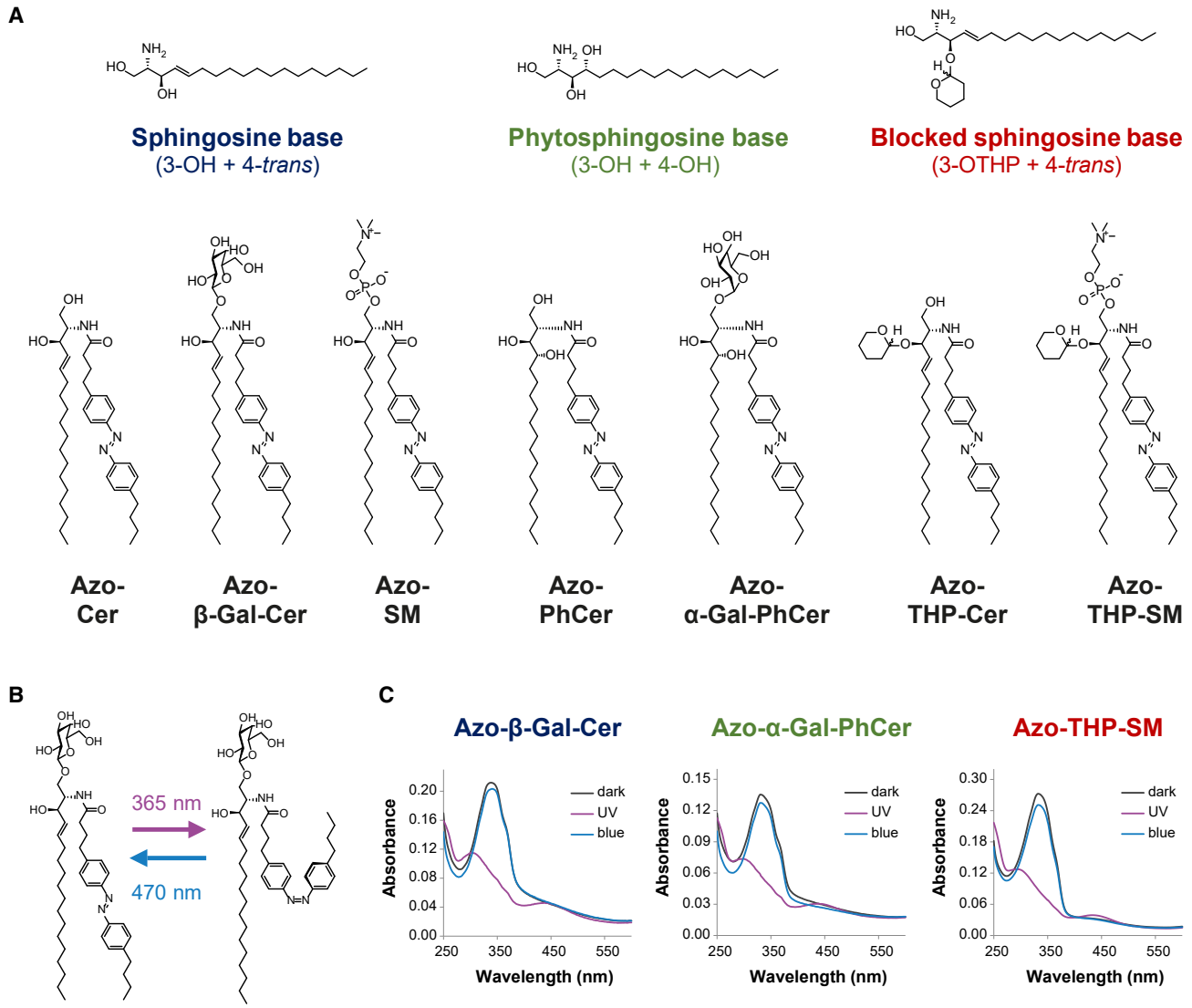

FIGURE 1 Structural and spectral properties of photoswitchable azo-sphingolipids. (*A*) Chemical structures of the *N*-acyl azobenzene-modified (FAazo-4 fatty acid) sphingolipids here tested, subdivided according to their sphingoid backbone: Azo-Cer, Azo-β-Gal-Cer, and Azo-SM with a sphingosine base and Azo-PhCer and Azo-α-Gal-PhCer with a phytosphingosine base, as well as Azo-THP-Cer and Azo-THP-SM displaying a 3-OH-blocked sphingosine base with a THP protecting group. (*B*) Schematics of light-induced *trans-cis* isomerization for an azo-sphingolipid, notably Azo-β-Gal-Cer. Application of UV-A light (λ = 365 nm) leads to the formation of a *cis*-photolipid, while illumination with blue light (λ = 470 nm) leads to the formation of a *trans*-photolipid. (*C*) UV-vis absorbance spectra of photoswitchable sphingolipids (notably Azo-β-Gal-Cer, Azo-α-Gal-PhCer, and Azo-THP-SM) incorporated in SUVs at the dark-adapted state (*black curves*), as well as after the sequential shining of UV-A (*purple curves*) and blue light (*blue curves*). To see this figure in color, go online.

phytoceramide with FAAzo-4 using HBTU as a coupling agent (see supporting material). Additional protecting group manipulations yielded Azo-THP-Cer.

For the synthesis of Azo-β-Gal-Cer, we used a benzoyl protected alcohol and the azide as protecting groups (56) (see supporting material). Azides do not coordinate to the primary alcohol, and thereby the nucleophilicity of the sphingosine is greatly enhanced. Glycosylation of azidosphingosine with trichloroacetimidate yielded protected glycoside in 92% yield and excellent β-selectivity. Staudinger reduction using PBu_3 and subsequent amide coupling with FAAzo-4 (37) using 1-ethyl-3-(3-dimethylaminopropyl) carbodiimide, followed by global deprotection gave Azo-β-Gal-Cer (see supporting material).

The SM derivatives were prepared from Azo-THP-Cer, which was phosphorylated using 2-cyanoethyl-*N*,*N*,*N*′,*N*′-tetraisopropylphosphorodiamidite and 1H-tetrazole, followed by reaction with choline tosylate (see supporting material). An oxidation directly yielded Azo-THP-SM. Finally, deprotection under acidic conditions gave the unprotected Azo-SM (see supporting material).

Light responsiveness of membrane-embedded azo-sphingolipids

Next, we incorporated our newly synthesized **Azo-β-Gal-Cer**, **Azo-SM**, **Azo-PhCer**, **Azo-THP-SM**, and **Azo-THP-Cer** photolipids, as well as **Azo-Cer** and **Azo-α-Gal-PhCer**, into L_d-L_o phase-separated mixtures containing DOPC, Chol, and SM (18:0-SM) and formed SUVs as previously described (39,57). Unless otherwise stated, a molar ratio of 10:6.7:5:5 (DOPC:Chol:SM:photolipid) was typically chosen.

We started with dynamic light scattering to determine the typical size and monodispersity of the sonicated SUVs. As shown in Fig. S1, the average number-normalized diameters were between 40 and 60 nm. Then, we collected UV-vis spectra of those various SUV suspensions and characterized the photodynamic properties of the different azobenzene-modified sphingolipids within a membrane environment. As seen in Figs. 1 *C* and S2 (see supporting material), the azo-sphingolipids displayed an absorbance maximum, λ_{max}, at ∼340 nm when in the dark-adapted state prior to irradiation with UV-A or blue light. This peak corresponds to the $\pi \rightarrow \pi^*$ transition and is characteristic for the *trans*-azobenzene isoform. First illumination with UV-A light ($\lambda = 365$ nm) led to the reduction of the abovementioned absorbance peak and to the appearance of a new λ_{max} at ∼450 nm. This new peak corresponds to the $n \rightarrow \pi^*$ transition and is characteristic for the *cis*-azobenzene isoform. Subsequent irradiation with blue light ($\lambda = 470$ nm) led then to a back isomerization of the *N*-acyl azobenzene moieties into the *trans*-isoform, as confirmed by the disappearance of the absorbance peak at ∼450 nm and the reemergence of the absorbance peak at ∼340 nm.

Our results indicate that the tested photoswitchable sphingolipids are in the *trans*-configuration for the dark- and blue light-adapted states and are mostly in *cis*-configuration for the UV light-adapted state. To infer if significant spectral shifts occur due to headgroup functionality and sphingoid polarity, we performed additional experiments examining the UV-vis spectra of extruded large unilamellar vesicles with a DOPC:Chol:SM:photolipid composition (10:6.7:5:5 mol ratio), followed by solubilization with 0.1% (v/v) Triton X-100 to eliminate the contribution of scattering. When we normalize the spectral maxima (Fig. S2 *E*), we find a stronger spectral red shift of ∼7 nm for the blocked THP photolipids (maximum 338 nm) compared with the azo-sphingolipids and azo-phytosphingolipids (maximum 331 nm). Thus, it appears that the presence of the THP moiety only slightly affects the spectral azobenzene properties of our photolipids.

Subsequently, we deposited SUVs composed of quaternary DOPC:Chol:SM:photolipid mixtures doped with 0.1 mol % Atto655-DOPE (dye labeling the L_d regions) on top of freshly cleaved mica to form SLBs via vesicle fusion. By collecting fluorescence confocal images, we first evaluated membrane integrity and the presence of phase separation for samples having sphingosine- (Azo-Cer, Azo-β-GalCer, Azo-SM), phytosphingosine- (Azo-PhCer, Azo-α-GalPhCer), and blocked THP-sphingosine-based (Azo-THP-SM) lipids. As seen in Figs. S3 and S4, all tested SLBs displayed L_d-L_o phase separation at the dark-adapted state, with μm-sized rigid L_o domains (*dark areas in fluorescence images*) segregated within a fluid L_d matrix (*red areas in fluorescence images*).

The photoresponsiveness and ability of the azo-sphingolipids to then remodel/reorganize phase-separated SLBs were further assessed directly after irradiation with UV-A light ($\lambda = 365$ nm). For membranes lacking a photolipid (control sample with a DOPC:Chol:SM composition at a mol ratio 10:6.7:10), no light-induced remodeling was observed (Fig. S3 *A*). In contrast, for SLBs containing azo-sphingolipids, stark lipid rearrangement dependent on the amount of photolipid present was reported. Here, lipid bilayers with the highest amount of azo-sphingolipid tested (18.7 mol %; DOPC:Chol:SM:photolipid with mol ratio 10:6.7:5:5) showed strong reorganization of the L_o domains with admixing of fluorescently marked L_d lipids and blurring of the domain boundaries directly after UV-A irradiation (Fig. S3, *B–G*). Intermediate amounts of photolipid (11.2 mol %; DOPC:Chol:SM:photolipid with mol ratio 10:6.7:7:3) led to a lower domain remodeling activity. Finally, for SLBs with the lowest amount of azo-sphingolipid tested (3.7 mol %; DOPC:Chol:SM:photolipid with mol ratio 10:6.7:9:1), only a minor admixing of L_d-L_o domains was observed (Fig. S4). Thus, the higher the concentration of azo-sphingolipids on the membranes, the stronger the reorganization of the phase-separated domains directly after UV-triggered photoisomerization of the *N*-azobenzene acyl

chain of lipids into *cis*. Specifically, the observed mixing of the L_d marker from the highly fluorescent L_d matrix regions to the nonfluorescent L_o domain regions is evidence that lipid content is exchanged between the two domains immediately after UV illumination. To be precise, this phenomenon hints that the membrane gets "fluidified" once the photolipids are switched, as L_d-localizing lipids appear to "populate" (i.e., diffuse into) the more rigid L_o domains.

Remodeling of membrane domains by sphingosine-based azo-sphingolipids

After the initial characterization and screening mentioned above, we systematically investigated the light-induced remodeling of phase-separated supported membranes with 18.7 mol % photolipid (DOPC:Chol:SM:photolipid, 10:6.7:5:*5* mol ratio) by first performing high-speed AFM to gain more insight into the activity of the photolipids. AFM enables us to capture minor dynamic changes in membrane architecture very accurately due to its exquisite sub-nm resolution. Herein, we started by analyzing bilayers containing the sphingosine-based photolipids Azo-Cer, Azo-β-GalCer, and Azo-SM.

At the dark-adapted state, those various membranes displayed a height mismatch between the L_d and L_o regions of 1.1–1.7 nm, similar to what we reported before for phase-separated bilayers with Azo-Cer (ACes) lipids (39). Application of UV-A light ($\lambda = 365$ nm) to bilayers having Azo-Cer, Azo-β-GalCer, or Azo-SM led then to the generation of an L_d phase, with no major alteration of the L_d-L_o domain height mismatch (i.e., minor increase of ∼0.1 nm).

As seen from single images in Figs. 2 *A* and S5 *B* and Videos S1, S2, S3, S4, S10, S11, and S12, the UV-induced isomerization of the *N*-acyl chains from a straight *trans*-form into a kinked *cis*-form promoted an apparent "fluidization" of the phase-separated membranes, with an overall robust decrease of the total L_o area for all three azo-sphingolipids (Fig. S6 *C*). Directly after irradiation with UV-A light, small nanoscopic L_d "lakes" were formed within the more rigid, thicker L_o domains, consistent with the influx of L_d markers into the L_o regions observed in Fig. S3. Because the height of the L_o domains is largely unaffected by the isomerization of these photolipids in *cis*, the nanoscopic L_d lakes detected by AFM may be the reservoirs into which the fluorescent L_d markers distribute immediately after photoisomerization. These membrane nanopockets with diameters below the diffraction limit would be poorly resolved in fluorescence microscopy, which explains the fluorescently smeared appearance of the L_o regions when detected under the confocal microscope (Figs. S3 and S4).

The number of fluid L_d lakes then rapidly dropped in order to reduce surface tension. While the majority of the smaller nanoscopic L_d lakes seem to vanish toward the outer fluid L_d matrix, a few larger fluid L_d lakes remained trapped inside rigid L_o domains, appearing to grow primarily via domain fusion and/or Ostwald ripening (58). Finally, if all the high-speed AFM area values (Figs. 2, *A* and *C*, and S5 *B*; $n = 7$) for this class of photolipids are grouped, an average L_o area decrease of ∼25% (area L_o(UV)/area L_o(dark) = 0.75 ± 0.14) can be estimated, as depicted in Fig. S6.

After a few minutes of equilibration, subsequent application of a brief pulse of blue light ($\lambda = 470$ nm) to those phase-separated membranes reversed the effect, with an L_o phase being generated. Here, back isomerization of the *N*-acyl chains from a kinked *cis*-form into a straight *trans*-form, stimulated by blue light, promoted a rigidification of the membranes (Figs. 2 *A* and S5 *B*), with an increase of the total L_o area (Fig. S5 *C*) back to its original equilibrium dark-adapted value (area L_o(blue)/area L_o(dark) = 1.01 ± 0.18; from grouped high-speed AFM area values in Fig. S6). More specifically, upon irradiation with blue light, small rigid L_o "islands" were firstly formed within the fluid L_d matrix (Videos S1, S2, S3, S4, S10, S11, S12, and S13). These taller L_o islands then vanished, as preexisting L_o domains grew primarily via Ostwald ripening and domain fusion. Moreover, L_o domains displayed height values like the ones reported before for the initial dark-adapted state. Interestingly, those changes could be repeated over multiple cycles without dissipation effects, with the amount of L_d-L_o phase separation alternating between two defined steady states (or area levels) (Fig. 2, *C* and *D*).

Besides changes in L_d-L_o phase separation, we also observed sporadic generation of holes on our supported bilayers after the blue light-triggered conversion of the azo-sphingolipids' *N*-acyl chains from *cis* to *trans* (Fig. S7 *A*). The presence of holes allowed us to recover the total membrane thickness, which was ∼5.2 nm (L_d thickness ∼3.9 nm; Fig. S7, *B* and *C*), in agreement with previously reported values for membranes of comparable lipid composition (59–61).

In summary, the tested azo-sphingolipids with a sphingosine backbone display a similar photoswitching profile independently of the type of headgroup. These lipids are able to increase the amount of L_d phase on phase-separated membranes upon conversion to the *cis*-isoform after UV-A light irradiation and increase the amount of L_o phase upon conversion to the *trans*-isoform after irradiation with blue light.

Remodeling of membrane domains by phytosphingosine-based azo-sphingolipids

Next, we recapitulated the same high-speed AFM procedures on membranes with photoswitchable phytosphingosine-based sphingolipids displaying two hydroxyl groups (3-OH + 4-OH) on the phytosphingosine backbone. More precisely, we investigated the ability of these photolipids to interfere with the L_d-L_o phase separation on SLBs

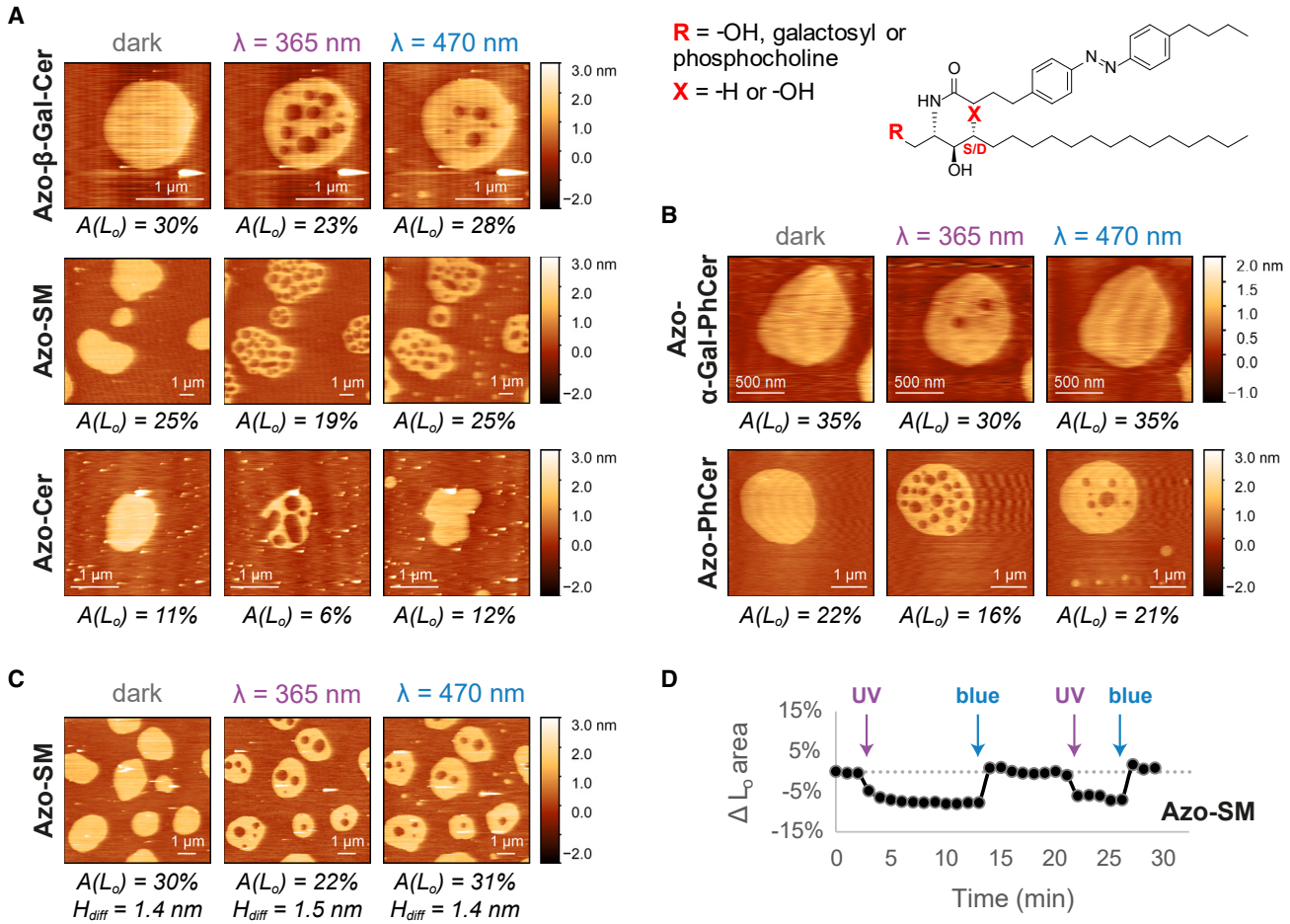

FIGURE 2 Lateral remodeling of phase-separated membranes containing nonblocked azo-sphingolipids upon light trigger analyzed by high-speed AFM. (*A* and *B*) Changes in the area of L_o domains (of depicted snapshots) before/after illumination with UV-A (λ = 365 nm) and blue (λ = 470 nm) lights on DOPC:Chol:SM:photolipid (10:6.7:5:5 mol ratio) SLBs having (*A*) Azo-β-Gal-Cer (see Video S1), Azo-SM (see Video S2), or Azo-Cer (see Video S3) with a sphingosine backbone (X = –H) and varying headgroup functionality (R = galactosyl, phosphocholine, or –OH, respectively) or (*B*) Azo-α-Gal-PhCer (see Video S5) or Azo-PhCer (see Video S6) with a phytosphingosine backbone (X = –OH) and varying headgroup functionality (R = galactosyl or –OH, respectively). (*C* and *D*) Reversible lateral remodeling of a phase-separated SLB containing Azo-SM (DOPC:Chol:SM:Azo-SM; 10:6.7:5:5 mol ratio) upon UV-A/blue light irradiation, as seen in Video S4. (*C*) AFM images of the SLB at the dark-, UV-, and blue light-adapted states, displaying the area occupied by the L_o phase and the L_d-L_o height mismatches. (*D*) Relative variation of total L_o area of the SLB over time, shown in Video S4, upon shining short pulses (marked with *arrows*) of UV-A and blue light. To see this figure in color, go online.

when compared with sphingosine-based lipids having only one hydroxyl (3-OH) on their backbone.

In the dark-adapted state, phase-separated DOPC:Chol:SM:photolipid SLBs with Azo-PhCer and Azo-α-Gal-PhCer exhibited a domain height mismatch of 1.2–1.8 nm (Figs. 2 *B* and S5 *C*), very close to the L_d-L_o height differences here reported for membranes with sphingosine analogs (Figs. 2 *A* and S5 *B*). Upon photoactivation, the L_d-L_o phase-separated SLBs containing either Azo-PhCer (with a hydroxyl headgroup) or Azo-α-Gal-PhCer (with a bulkier galactosyl headgroup) behaved in a similar way to membranes with sphingosine-based azo-sphingolipids by exhibiting, at the end, an identical phenotype of membrane remodeling (Fig. S6 *C*).

As seen in Figs. 2 *B* and S5 *C* and Videos S6, S7, S13, S14, and S15, after irradiation with UV-A light (λ = 365 nm), L_d lakes initially appeared inside existing L_o domains, and the total L_d phase membrane area lowered by ∼23% (area L_o(UV)/area L_o(dark) = 0.78 ± 0.18, from grouped high-speed AFM area values in Fig. S6, extracted from Figs. 2 *B* and S5 *C*; $n = 5$), while the domain height mismatch did not change majorly. Then, after irradiation with blue light (λ = 470 nm), L_o islands initially formed inside the L_d regions, and the total L_o phase membrane area subsequently increased to the initial equilibrium dark-adapted values (area L_o(blue)/area L_o(dark) = 1.03 ± 0.20, from grouped high-speed AFM area values in Fig. S6).

Our results confirm that the bulkiness of the neutral headgroup does not play a role in the membrane remodeling ability of our photoswitchable phytosphingolipids. Moreover, the increased backbone polarity of the phytosphingosine backbone does not seem to affect the way

azo-phytosphingolipids engage in interactions with their neighboring lipids when compared with azo-sphingolipids. Hereby, we conclude that the tested Azo-Cer, Azo-β-GalCer, Azo-SM, Azo-α-Gal-PhCer, and Azo-PhCer establish stable interactions with other sphingolipids (such as SM) and sterols (such as Chol) inside L_o domains when their azobenzene acyl chain is in the *trans*-isoform (imitating a "straight" saturated acyl chain) and with unsaturated phosphatidylcholines (e.g., DOPC) inside L_d regions when the azobenzene is in the *cis*-isoform (mimicking a "bent" unsaturated chain).

It is worth noting that the normalized extent of L_o domain area changes produced by *trans-cis* isomerization of the *N*-acyl azobenzene chain in these two classes of photolipids (Fig. S6 *C*) appears to be robust and independent of domain size, scanned area dimensions, and different L_o phase surfaces scanned locally (Figs. 2, 3, and S5). A direct comparison of all AFM time lapses (Videos S1, S2, S3, S4, S5, S6, S7, S8, S9, S10, S11, S12, S13, S14, S15, S16, and S17) also shows that it is difficult to assign whether the contribution of Ostwald ripening or domain fusion to the restructuring of L_d lakes is different for each photolipid type. This was particularly evident in membranes containing Azo-α-Gal-PhCer and Azo-Cer (with completely different backbones and headgroups), where some of the bilayers appeared to show a more rapid remodeling and domain fusion-based mechanism of the L_d lakes upon UV irradiation, while in other bilayers/areas, the remodeling/expulsion of the L_d lakes trapped inside L_o domains appeared to occur slowly by Ostwald ripening (for Azo-Cer, see Videos S3 and S12; for Azo-α-Gal-PhCer, see Videos S5, S13, and S14).

Remodeling of membrane domains by 3-OH-blocked azo-sphingolipids

In order to infer the exact role of H-bonding and sphingoid base polarity for the mode of action of azo-sphingolipids, we used high-speed AFM to further investigate the photoswitching and lateral membrane remodeling activities of the azo-sphingolipids Azo-THP-Cer and Azo-THP-SM. These lipids have the 3-OH group on their sphingosine backbone protected with a bulky THP moiety. Notably, the final protecting step resulted in an inseparable mixture of diastereomers at the THP linkage (see Fig. 3), which was used in all experiments.

In the dark-adapted *trans*-form, DOPC:Chol:SM:photolipid bilayers containing 3-OH-blocked Azo-THP-SM or Azo-THP-Cer (Figs. 3 and S5 *D*; Videos S7, S8, S9, S16, and S17) had L_o domains with irregular borders and lower heights (~0.6–0.9 nm) when compared with SLBs with non-blocked counterparts (Fig. 2). Such a noticeable effect on the global architecture of L_o domains is evidence that

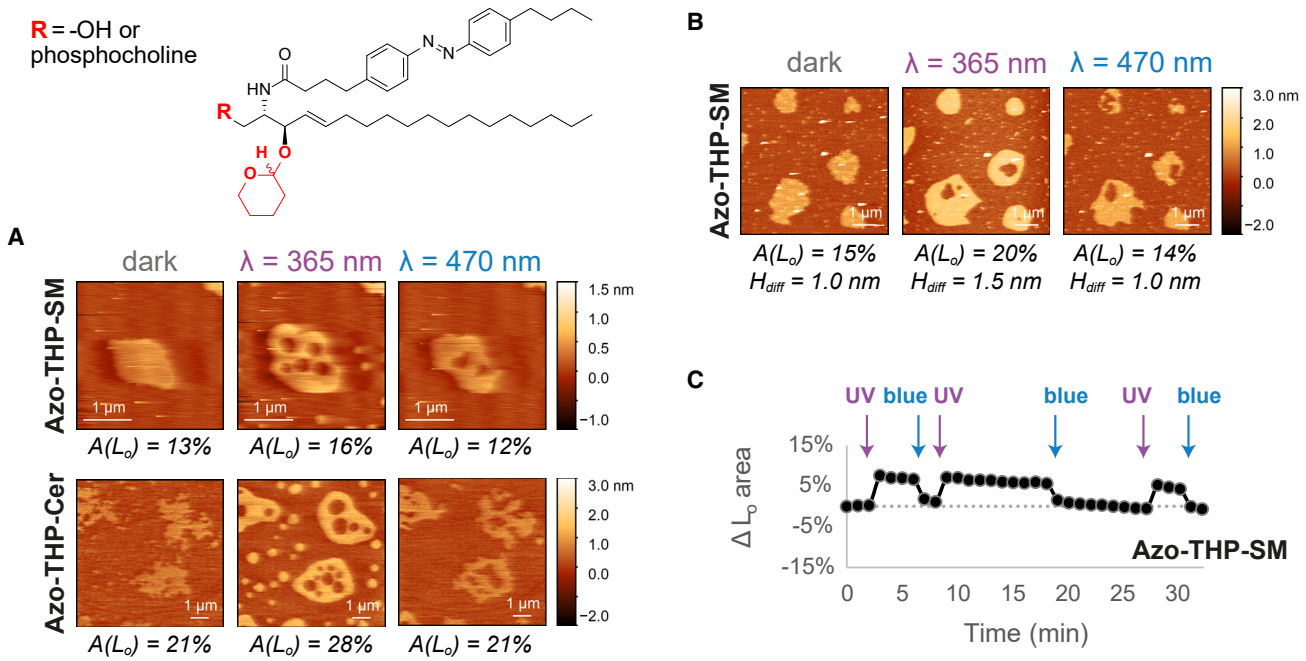

FIGURE 3 Lateral remodeling of phase-separated membranes containing 3-OH-blocked azo-sphingolipids upon light trigger analyzed by high-speed AFM. (*A*) Changes in the area of L_o domains (of depicted snapshots) before/after illumination with UV-A (λ = 365 nm) and blue (λ = 470 nm) lights on DOPC:Chol:SM:photolipid (10:6.7:5:5 mol ratio) SLBs having Azo-THP-SM (see Video S7) or Azo-THP-Cer (see Video S8) with a 3-OH-blocked (THP-protected) sphingosine backbone and varying headgroup functionality (R = phosphocholine or –OH, respectively). (*B* and *C*) Reversible lateral remodeling of a phase-separated SLB with Azo-THP-SM (DOPC:Chol:SM:Azo-THP-SM; 10:6.7:5:5 mol ratio) upon UV-A/blue light irradiation, as seen in Video S9. (*B*) AFM images of the SLB at the dark-, UV-, and blue light-adapted states, displaying the area occupied by the L_o phase and the L_d-L_o height mismatches. (*C*) Relative variation of total L_o area of the SLB over time, shown in Video S9, upon shining short pulses (marked with arrows) of UV-A and blue light. To see this figure in color, go online.

3-OH-blocked lipids are able to reduce the molecular packing within the L_o phase, as previously reported for 3-OH-blocked stearoyl-SM (29,62).

When the membranes with THP-protected photolipids were irradiated with UV-A light ($\lambda = 365$ nm) and the lipids converted to the *cis*-isoform, the total area of L_o phase markedly increased ~23% (area L_o(UV)/area L_o(dark) = 1.23 ± 0.21, from grouped high-speed AFM area values in Fig. S6, extracted from Figs. 3 and S5 *D*; $n = 5$), with L_o domains getting larger, rounder, and noticeably higher (~1.1–1.4 nm) (Fig. 3, *A* and *B*). Quite strikingly, directly after exposure to UV-A light, L_d lakes inside preexisting L_o domains, as well L_o islands within the L_d matrix were transiently formed. The preexisting L_o domains then grew in total area, mainly via Ostwald ripening as L_o islands disappeared, whereas only a few larger L_d lakes appeared at the end trapped inside the enlarged L_o domains.

Subsequent illumination with blue light ($\lambda = 470$ nm) led to an overall decrease of both total L_d-L_o height mismatch and L_o area back to the initial dark-adapted state values (area L_o(blue)/area L_o(dark) = 0.98 ± 0.20, Fig. S6), as the 3-OH-blocked photolipids isomerized back to the *trans*-isoform. Interestingly, no noticeable formation of large L_d lakes or L_o islands was observed here. The L_o domains rapidly shrank with their domain borders becoming irregular (less rounded) and more unstable, as large rapid fluctuations were visible (Videos S7, S8, S9, S16, and S17). This clearly indicates that the THP-protected azo-sphingolipids, when in the *trans*-isoform, severely affect line tension of the phase-separated domains. Finally, the reported L_o domain height and area changes within the phase-separated bilayers could be repeated over multiple illumination cycles, as seen in Fig. 3 *C* and Videos S7, S8, S9, S16, and S17.

To sum up, photoswitchable sphingolipids having their 3-OH sphingoid moiety blocked with a THP group promote a clearly distinct light-induced reorganization of L_d-L_o phase-separated membranes when compared with non-blocked counterparts. These blocked lipids are able to significantly increase the percentual amount and height of the L_o phase upon UV-triggered isomerization to the *cis*-isoform and to decrease both these parameters upon blue light-triggered isomerization to the *trans*-isoform. Moreover, the formation of L_d lakes and L_o islands only after the application of UV light (and not blue light) suggests an altered distribution profile of these photolipids within the L_d and L_o phases when compared with nonblocked photolipids.

Phase-separation area changes by photoswitchable sphingolipids

After demonstrating that the various nonblocked versus hydroxyl-blocked photoswitchable sphingolipids reorganize phase-separated membranes differently, we set out to quantitatively compare the extent by which these lipids alter the total distribution of phase separation, as well as other structural membrane parameters.

To begin, since AFM only allows us to follow a limited number of L_o domains simultaneously, we acquired additional large field-of-view fluorescence confocal images (Figs. S8, S9 *A*, and 4 *A*) to obtain better statistics for determining ensemble area values independent of domain size and number. We analyzed changes in L_o total area before/after UV/blue irradiation on DOPC:Chol:SM control SLBs ($n = 5$ images) and, most importantly, DOPC:Chol:SM:photolipid SLBs containing 18.7 mol % Azo-Cer, Azo-β-GalCer, Azo-SM, Azo-PhCer, Azo-α-GalPhCer, Azo-THP-Cer, or Azo-THP-SM (number of images per photolipid, $n = 5$–8) doped with 0.1 mol % Atto655-DOPE for fluorescent detection of the L_d phase.

Usage of fluorescence allowed us to easily generate binary masks (Fig. S8), from which L_o phase areas could be straightforwardly estimated. Instead of collecting the confocal images immediately after photoisomerization (Fig. S3), which would have been smeared due to the short-lived nanoscopic L_d lakes, we let the SLBs equilibrate here for 20 min after brief irradiation with UV/blue light. In this way, we were able to reduce the number of hard-to-resolve L_d lakes and L_o islands and obtained a clearer macroscopic L_d-L_o phase separation (Figs. 4 *A* and S9 *A*).

All average absolute L_o area values recovered for the various SLBs are shown in Fig. S9 *B*. These values are particularly important as a way to assess the extent of membrane phase-separation perturbation caused by the presence of *trans*-photolipids prior to photoactivation. Briefly, control membranes without photolipids (DOPC:Chol:SM 10:6.7:10 mol ratio) displayed a total surface coverage by L_o domains of 45%. A similar average value of 45% ± 4% was obtained for membranes with 18.7 mol % nonblocked photolipids in *trans*. Only the SLBs with THP-protected *trans*-photolipids showed significantly lower total L_o domain coverage, about 29% ± 3% ($p < 0.001$), when compared with the control membranes without photolipids. This large reduction in total L_o area for membranes with hydroxyl-protected azo-sphingolipids clearly supports our AFM observation that THP-blocked *trans*-photolipids affect L_o phase properties.

To facilitate data comparison for the photoswitchable conversion of phase separation by our photolipids, the recovered L_o areas were normalized before/after UV/blue light illumination by the average L_o area for the different individual SLBs at the dark-adapted state (Fig. 4 *C*). This allowed us to analyze the relative changes in the total L_o area (for *cis*- and *trans*-photolipids) and compare it with the behavior of the DOPC:Chol:SM control lipid samples without photolipids (Fig. 4 *C*). Relevant statistical comparisons were then performed using one-way analysis of variance followed by Bonferroni comparison *t*-tests (95% confidence interval), and the respective *t* statistics and p values are listed as supporting material in Table S3.

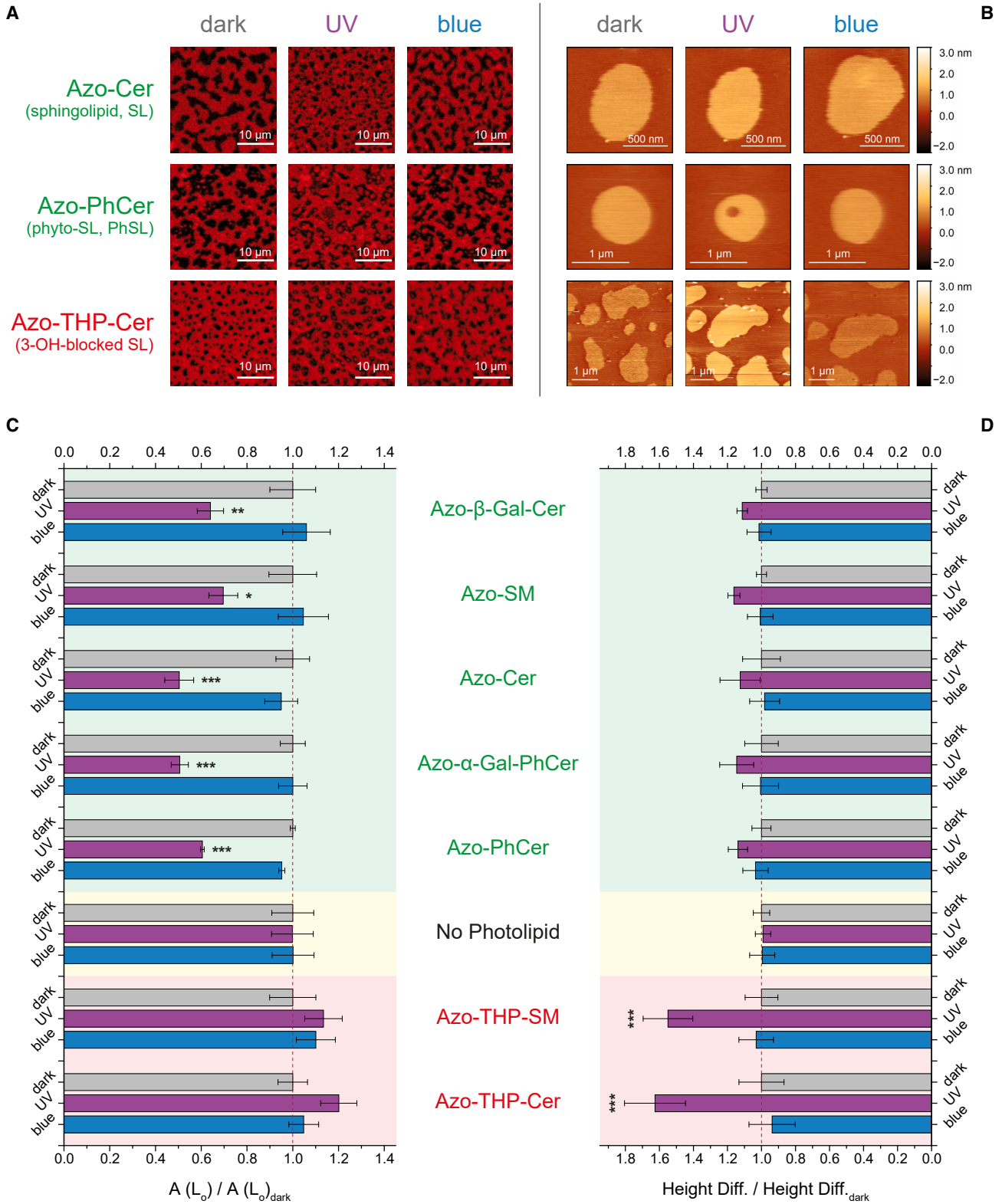

FIGURE 4 Normalized changes in the total L_o phase area and L_d-L_o height difference on phase-separated SLBs having different types of azo-sphingolipids upon application of UV-A ($\lambda = 365$ nm) and blue ($\lambda = 470$ nm) lights. Fluorescence confocal (*A*) and AFM (*B*) images of DOPC:Chol:SM:photolipid (10:6.7:5:5 mol ratio) SLBs with sphingosine-based Azo-Cer, phytosphingosine-based Azo-PhCer, or 3-OH-blocked sphingosine-based Azo-THP-Cer, all having the same –OH headgroup but distinct sphingoid backbone. Normalized L_o areas (*C*) and L_d-L_o height differences (*D*), respectively, recovered

(legend continued on next page)

As seen in Figs. 4 *C* and S9 *B*, the total L_o area for phase-separated SLBs having sphingosine- or phytosphingosine-based photolipids significantly decreased (with p values between $p < 0.05$ and $p < 0.001$) on average by 41% (area L_o(UV)/area L_o(dark) = 0.59 ± 0.04) after UV-A illumination (when the lipids are in *cis*) and augmented back to the original dark-adapted state (area L_o(blue)/area L_o(dark) = 1.00 ± 0.02) upon blue light irradiation (when the lipids are in *trans*). For SLBs having Azo-THP-SM or Azo-THP-Cer, on the contrary, the total area of the L_o phase did not statistically change ($p > 0.05$) when compared with control membranes without a photolipid. Here, only a slight increase by 17% (area L_o(UV)/area L_o(dark) = 1.17 ± 0.03) after illumination with UV-A light is seen, while the recorded amount of L_o phase decreased back to the original dark-adapted state value (area L_o(blue)/area L_o(dark) = 1.07 ± 0.03) after the application of a blue light pulse.

Interestingly, if we compare the changes in L_o area after azo-sphingolipid photoisomerization determined by fluorescence (Figs. 4 *C* and S9) versus high-speed AFM data (Fig. S6), the area changes for confocal microscopy seem to be skewed toward detecting higher amounts of L_d phase after UV irradiation. This skew may be a direct consequence of the limited pixel resolution of conventional laser-scanning confocal microscopy for detecting nanoscale L_o domains when compared with AFM. Despite this instrumental bias, similar trends in membrane domain area variations were detected with both fluorescence confocal and AFM techniques.

These experiments corroborate that sphingosine- and phytosphingosine-based photolipids rely on the same principles for reshuffling membrane phase-separated domains, whereas the THP-protected counterparts, owing to their distinct physicochemical properties, follow a markedly different mechanism. Finally, although there is no statistical difference between the various sphingosine- and phytosphingosine-based *cis*-photolipids ($p = 1$), the obtained *t* statistics for their comparison with the control DOPC:Chol:SM suggest a possible hierarchy. Here, Azo-Cer and the two azo-phytosphingolipids (Azo-α-Gal-PhCer and Azo-PhCer), the latter being able to establish stronger H-bonding interactions, appeared to possess the strongest "remodeling activity" (with $p < 0.001$) (see Table S3 for more details).

Domain height mismatch changes by photoswitchable sphingolipids

Our results so far clearly point out that blocking the interfacial hydroxyl on the sphingoid backbone has a marked effect on the molecular organization of individual lipids and on the global architecture of L_o domains. Thus, to quantitatively ascertain how photoswitchable sphingolipids affect the structure and physicochemical properties of L_o domains within phase-separated membranes, we collected zoomed-in and high-resolution low-speed AFM images (n = 5–9) of individual L_o domains on DOPC:Chol:SM:photolipid SLBs prior to and 20 min after brief illumination with UV-A/blue light (to let domains equilibrate and reduce the amount of L_d lakes and L_o islands), as depicted in Figs. 4 *B*, S10, and S11 *A*. This acquisition mode allows us to follow the membrane contour with an increased signal/noise ratio and therefore determine more accurately the height differences between the L_o domains and the surrounding L_d matrix (Fig. S10). This is an important parameter, as it relates to the hydrophobic mismatch between the saturated ("nonbent" acyl chains) lipids in L_o domains with increased chain order (63) and the unsaturated (bent acyl chains) lipids in less packed L_d regions.

Altogether, the average height difference between L_o and L_d regions (at the dark-adapted state for the various SLBs having either sphingosine- or phytosphingosine-based photolipids) was 1.3 ± 0.1 nm. This value corresponds to the mean of all average L_d-L_o height differences (± standard error) obtained for membranes containing Azo-Cer, Azo-β-GalCer, Azo-SM, Azo-PhCer, or Azo-α-GalPhCer (Fig. S11 *B*) and was very close to the less precise values previously reported using high-speed AFM. Owing to the exquisite *z*-resolution of AFM, we also identified that the L_o domains of SLBs having azo-sphingolipids with smaller headgroups (e.g., Azo-Cer and Azo-PhCer) were slightly less elevated (1 ± 0.1 nm) than the L_o domains of SLBs having azo-sphingolipids with larger headgroups (e.g., Azo-SM, Azo-β-GalCer, and Azo-α-GalPhCer). The later-displayed L_d-L_o height mismatches (1.4 ± 0.1 nm) are closer to the values recovered (1.8 ± 0.1 nm) for control ternary mixtures without a photolipid. Hence, our observations corroborate a preferred localization of the *trans*-azo-sphingolipids inside L_o domains, as these lipids could then engage hydrophobic packing and stable H-bonding interactions with SM and Chol, altering slightly the height of L_o domains due to the different headgroup size and *N*-acyl chain length (e.g., C18:0 acyl chain: 21.2 Å vs. FAAzo-4: 17.9 Å, retrieved from Chem3D, PerkinElmer, Boston, MA, USA).

Interestingly, upon applying UV-A light to SLBs having these nonblocked photolipids, the L_d-L_o height mismatch increased on average by 14% (1.4 ± 0.1 nm; Fig. 4 *D*). Although this variation is not statistically relevant, it is in line with the exclusion of *cis*-azo-sphingolipids from the

from fluorescence confocal and AFM data for phase-separated SLBs having either azo-(phyto)sphingolipids with free 3-OH (marked in *green*), no azo-sphingolipid (controls with SM, marked in *yellow*), or THP-protected azo-sphingolipids with the 3-OH blocked (marked in *red*). Error bars correspond to standard error of the mean (n = 5–8 confocal images each). Statistical analysis: *cis*-photolipids versus no photolipid (***$p < 0.001$, **$p < 0.005$, *$p < 0.05$). See Figs. S9 and S11 for details. To see this figure in color, go online.

L_o phase and SM being then the predominant sphingolipid molecule inside those domains. Subsequent irradiation with blue light led to the decrease of the domain height by 13% back to the original values reported for the dark-adapted state (Fig. 4 *D*), corroborating a repartitioning of *trans*-azo-sphingolipids back to the L_o phase.

For membranes having hydroxyl-blocked photolipids, the height of L_o domains at the dark-adapted state was lower, and the domain boundaries more irregular, when compared with membranes with nonblocked counterparts. Indeed, the L_d-L_o height mismatch observed for SLBs with Azo-THP-SM or Azo-THP-Cer was below 1 nm (0.7 $\pm$ 0.1 nm; Fig. S11 *B*), similar to the values observed using high-speed AFM and nearly 0.5 and 1.0 nm lower than the height mismatch found for SLBs with Azo-SM or control membranes lacking azo-sphingolipids, respectively. The lower L_o height observed for membranes with 3-OTHP-lipids indeed corroborates that these lipids establish altered interactions with other colipids in the L_o phase when in the *trans*-isoform but, most importantly, validates that blocking H-bonding severely alters the molecular packing, as well as the line tension within L_o domains.

This destabilization effect can be overcome once the hydroxyl-blocked azo-sphingolipid is converted to its *cis*-isoform upon illumination with UV-A light. Indeed, after applying UV-A to the phase-separated SLBs with Azo-THP-SM, the L_d-L_o height mismatch significantly increased ($p < 0.001$) by 55% (Fig. 4 *D*) to average values above 1 nm (1.1 $\pm$ 0.1 nm). This elevation in height suggests that Azo-THP-SM and Azo-THP-Cer lipids are expelled from the L_o phase when in the *cis*-isoform, leaving the L_o domains mainly composed by SM and Chol. Without the interference of these THP-protected lipids, SM and Chol molecules can then establish more stable H-bonding and tighter hydrophobic chain packing interactions, giving rise to taller, rounder, and larger L_o domains. In opposition, irradiation of the phase-separated SLBs with blue light leads to a marked reduction of the L_o domain height (Fig. 4 *D*) back to the initial dark-adapted state value (0.7 $\pm$ 0.1 nm). As the 3-OH-blocked azo-sphingolipids isomerize back to their *trans*-isoform, these lipids could then reestablish hydrophobic chain packing interactions with the other L_o-localizing lipids, destabilizing the existing H-bonding interactions between SM and Chol.

Domain line tension changes by photoswitchable sphingolipids

A parameter closely linked to the domain height mismatch is line tension, which can be perceived as the interfacial energy arising at the boundaries of coexisting phases and is an important driving force for membrane shape transformation (e.g., budding (4,64,65) and fusion (66)). In order to estimate the approximate values of line tension for the various L_d-L_o membranes with distinct blocked and nonblocked photoswitchable sphingolipids, based on the height mismatch values measured using low-speed AFM, we used the theoretical model for flexible domains implemented by Cohen and co-workers (Eq. 1). This model describes a quadratic dependence of the line tension with the phase height mismatch (53) and was previously used to estimate line tension on phase-separated membranes with similar lipid compositions (52).

Overall, as seen in Fig. S11 *C*, line tension values ranged from 1.9 to 4.3 pN for L_d-L_o phase-separated SLBs with sphingosine- and phytosphingosine-based lipids in the *trans*-isoform. When the lipids are in the *cis*-isoform and partition to the L_d phase instead, a statistically nonsignificant yet small increase in line tension by 24% (Fig. S12) was recovered, with the values being very close to the ones gauged for phase-separated SLBs lacking azo-sphingolipids (5.4 $\pm$ 0.6 pN).

In contrast, L_d-L_o bilayers with THP-protected azo-sphingolipids (such as Azo-THP-SM and Azo-THP-Cer) in the *trans*-isoform possess noticeably reduced line tension values ($\sim$1.2 pN): 2.2- to 4.5-fold lower than the domain line tension measured for SLBs with nonblocked photolipid counterparts (Fig. S11 *C*). Next, when the hydroxyl-blocked lipids are in their *cis*-isoform and locate in the L_d phase, the domain line tension greatly increases ($p < 0.001$) by $\sim$120% (Fig. S12), reaching values close to the ones reported for nonblocked counterparts (2.6 pN). Hence, THP-protected photolipids, when in *trans*, greatly reduce the line tension of L_o domains in opposition to the azo-sphingolipids with free interfacial hydroxyls, appearing to possess additional line-active (lineactant) properties.

Line-active molecules are known to concentrate at the boundaries of membrane phases (67–70), reducing the hydrophobic mismatch and line tension around phase-separated domains (e.g., L_o versus L_d). Herein, hybrid lipids such as palmitoyl-oleyl-phosphatidylcholine, possessing both a saturated and unsaturated fatty acid chain, are of particular relevance. When added to ternary mixtures made of lipids with two saturated tails (e.g., DPPC or DSPC), two unsaturated tails (DOPC), and a sterol (Chol), palmitoyl-oleyl-phosphatidylcholine was shown to interact with the L_o phase and disturb the chain ordering of L_o domains in a so-called "partitioning and loosening" mechanism (71). Such an effect will then promote the reduction of line tension and formation of nanoscopic domains, hence lowering the differences in physical properties between the L_o and L_d phases (71–75). Interestingly, Azo-THP-SM and Azo-THP-Cer also appear to reduce line tension and promote the formation of nanoscopic domains in a similar way, sharing moreover key structural similarities with hybrid lipids: 1) the *trans*-azobenzene *N*-acyl chains mimic saturated fatty acids prone to localize within L_o domains, and 2) the bulky THP moiety at the sphingosine base appears to interfere with the molecular packing of lipids and therefore be susceptible to preferentially localize in the less packed L_d phase.

To sum up, the hybrid chain properties in addition to the blockage of H-bonding could be possible explanations for the observed perturbation of the L_o domain boundaries and reduction of domain height by THP-protected azo-sphingolipids in the *trans*-isoform. It is plausible that the blocked photolipids in the *trans*-configuration are not exclusively localized in the L_o phase but rather behave as a hybrid lipid able to interact with both the L_d and L_o phases.

Here, the blocked *trans*-photolipids partitioned inside the L_o phase could loosen the chain packing of the L_o domains, reduce line tension, and be responsible for the formation of L_d lakes within the L_o phase when converted into *cis*. Moreover, since the nominal height mismatch (Fig. S11 *B*) and total area (Fig. S9 *B*) of the L_o phase are significantly reduced ($p < 0.001$) on membranes with hydroxyl-blocked photolipids when compared with membranes with nonblocked photolipid equivalents (i.e., *trans*-Azo-SM and *trans*-Azo-Cer), we can also speculate that a small fraction of the destabilized "rigid" colipids (i.e., C18-SM and Chol) might be localized in the L_d phase as well. This would further substantiate the mechanism of L_o island formation after UV irradiation, as such a pool of rigid colipids in the L_d phase could serve as nuclei for the formation of L_o islands once the fraction of L_d-localizing THP photolipids is isomerized into *cis* and no longer destabilizes this pool of rigid colipids.

Changes in the mechanics of homogeneous membranes promoted by the photoisomerization of azo-spingolipids

Despite the differences in membrane domain remodeling by THP-protected versus nonprotected azo-sphingolipids, we also observed the generation of occasional membrane holes when isomerizing 3-OH-blocked photolipids from the bent *cis*-isoform to the straight *trans*-isoform, as depicted in Fig. S13 for phase-separated membranes with Azo-THP-SM. This hole formation clearly indicates that SLBs containing THP-protected azo-sphingolipids, similarly to membranes with nonblocked counterparts (Fig. S7 *A*), globally expand after UV-A illumination and subsequently compress upon illumination with blue light due to the bending and unbending on the *N*-acyl chains, respectively. Hence, photoswitching of azo-sphingolipids not only influences lipid phase separation (as discussed so far) but irrefutably affects basic mechanical properties of the membrane, such as packing and stiffness/fluidity.

To evaluate whether photoswitchable sphingolipids indeed interfere with global packing of membranes, irrespective of phase separation, we sought to perform additional analyses on a nonphase-separated system. In this context, we explored the possibility of using ternary compositions that form only a single L_o phase. It has been reported in the literature that certain sphingolipid-containing ternary mixtures such as DOPC:GalCer:Chol (37.5:37.5:25 mol %) can exhibit a single L_o phase in the presence of significant amounts of Chol (76), whereas other mixtures with the same ratio, e.g., DOPC:SM:Chol (37.5:37.5:25 mol %), can exhibit L_d-L_o phase separation (77). Some information is already available on ternary mixtures containing photolipids from previous work with colleagues, notably for the phosphatidylcholine Azo-PC. Specifically, for equimolar DPhPC:Azo-PC membrane mixtures, Urban et al. reported L_d-L_o phase separation in the presence of 10–35 mol % Chol and a single L_o phase with Chol above 35% (45). In addition, the authors also reported a single phase on giant vesicles for DOPC:Azo-PC with 20 mol % Chol (78).

With this in mind, we examined bilayers containing either Azo-Cer (as nonblocked azo-sphingolipid) or Azo-THP-SM (as 3-OH-blocked azo-sphingolipids) in a DOPC:Chol:photolipid composition with 10:6.7:10 mol ratio. As shown in Fig. S14 (using fluorescence confocal microscopy) and Fig. S15 (using AFM), these membrane compositions are indeed homogenous and do not exhibit domains either before or after irradiation with UV-A/blue light.

Next, we performed additional AFM-based force spectroscopy measurements, in particular nanoindentation experiments (54,55,79–84), on these ternary mixed homogenous SLBs having Azo-Cer (Fig. S16 *A*) or Azo-THP-SM (Fig. S16 *D*). In short, when indenting such membranes with an AFM tip, a typical jump (or discontinuity) corresponding to the force required to pierce (or break through) the SLB can be easily identified within the collected force-displacement curves (as seen in Fig. S16, *B* and *E*). The extent of such breakthrough forces is then directly linked to the mechanical properties of the membrane: lower forces are expected when the membranes are more fluid (or less compact) and higher forces when these are stiffer (or more compact). Thus, upon recording a set of force curves prior and after illumination with UV-A ($\lambda = 365$ nm) and blue ($\lambda = 470$ nm) lights, we evaluated the breakthrough events and displayed the recovered forces needed to pierce the membranes (Fig. S16, *C* and *F*) as histograms normalized by the average breakthrough force obtained for the dark-adapted state. Nonnormalized values are depicted in Fig. S17.

For homogenous DOPC:Chol:Azo-Cer SLBs, an average breakthrough force of 2.8 ± 0.3 nN ($n = 900$ curves) was recorded in the dark-adapted state (Fig. S17 *A*). After illumination with UV light, and consequent conversion of Azo-Cer to its bent *cis*-isoform, the force required for piercing the membrane reduced by ~30% (Fig. S16 *C*) to 1.9 ± 0.2 nN (Fig. S17 *B*). Irradiation with blue light, on the contrary, promoted an increase of the breakthrough force back to its original average value (2.8 ± 0.3 nN; Fig. S17 *C*), as Azo-Cer would back isomerize to its *trans*-isoform. Thus, for nonblocked azo-sphingolipids, we confirmed that the *cis*-isoform expands/fluidifies the membrane, while the *trans*-isoform compacts/stiffens it. In this context, our force data clearly back up a previous study (44) based on

fluorescence recovery after photobleaching, which showed that lateral lipid diffusion on a membrane made of Azo-PC (phosphatidylcholine analog with a FAAzo-4 acyl chain) was higher when the photolipid was in its *cis*-isoform and slower when in the *trans*-isoform.

Interestingly, the measured average breakthrough force required to pierce a bilayer with Azo-THP-SM was significantly higher than for bilayers containing Azo-Cer (Fig. S16, *B* and *E*). Although we cannot exclude a contribution of the THP moiety at the interface, the measured increase is mainly due to the larger phosphocholine headgroup of Azo-THP-SM compared with the smaller hydroxyl headgroup of Azo-Cer. Indeed, Garcia-Manyes et al. (81) had previously found a clear correlation of membrane piercing forces for lipids with the same acyl chains as a function of headgroup size. In that seminal work, the authors found that DPPA with the smallest headgroup had the lowest breakthrough force, followed by DPPE, DPPC, and DPPS.

When we instead analyze the normalized changes in breakthrough force for nonphase-separated DOPC:Chol: Azo-THP-SM bilayers as a function of photoisomeization, then similar trends as for Azo-Cer were recorded. More precisely, the piercing force needed to break through those membranes ($n = 200$ curves) also reduced by ~25% (Fig. S16 *F*), from 5 ± 0.4 (Fig. S17 *D*) to 3.8 ± 0.4 nN (Fig. S17 *E*), upon irradiation with UV light and formation of *cis*-Azo-THP-SM, in agreement with a global expansion or fluidification of the membrane. Subsequently, the membrane breakthrough force also reverted back close to the original value (4.7 ± 0.6 nN; Fig. S17 *F*) upon illumination with blue light and formation of *trans*-Azo-THP-SM, in agreement with a global compaction or rigidification of those membranes.

Therefore, based on this force spectroscopy outcome for homogenous membranes, we can argue that the opposite changes in L_o area for phase-separated SLBs containing either 3-OH-blocked or nonblocked azo-sphingolipids (observed throughout the previous manuscript sections) are mainly due to different types of interactions these photolipids engage in via their sphingoid backbone with neighboring lipids within L_o domains and are not directly linked to the structural properties of the *N*-acyl photoswitch per se.

Comparison of the behavior of photolipids in direct relation to their natural sphingolipid counterparts

In this article, we have shown that photoswitchable sphingolipids with an azobenzene *N*-acyl chain are able to change the L_d-L_o ratio on phase-separated membranes and to affect packing on homogeneous membranes in a photoisomerization-dependent manner. However, a fundamental question remains as to how similar and biocompatible such photolipids are with respect to their natural counterparts.

Photolipids appear to maintain phase separation in the presence of native counterparts, as recently shown by Socrier et al. for photo-Gb3 (85) and previously by us for Azo-Cer (39). For example, in our previous work (39), we have shown that Azo-Cer not only maintains L_d-L_o phase separation but is also able to sustain a liquid-gel phase when mixed with DOPC and SM in the absence of Chol. From previous results with Azo-PC (45), it also appears that photolipids are, in principle, capable of forming phase separation themselves. However, the exact ratios required for these processes may differ from those of the native 18:0 or 16:0 counterparts and depend on the nature of the colipids used.

Concerning native sphingolipids, several studies in the literature suggest that small differences in headgroup, acyl chain, or sphingoid base are sufficient to significantly alter membrane properties and lateral organization. For example, it is well known that Cers have a strong ability to induce gel-fluid phase separation on membranes, as reported elsewhere (86,87). Particularly important is the presence of significant amounts of Chol, which is known to liquefy such rigid gel phases. As previously mentioned in changes in the mechanics of homogeneous membranes promoted by the photoisomerization of azo-spingolipids, no gel phases were found for equimolar DOPC:SM (77) or equimolar DOPC:GalCer (76) mixtures with 25 mol % Chol. For mixtures containing Cer, Castro et al. (88) also reported that increasing amounts of Chol liquefied the gel phases.

Since the presence or absence of certain phases depends then on the ratiometric combination and the nature of the spingolipids and colipids (i.e., unsaturated phospholipid and Chol), we still decided to investigate the phase-separation properties of natural C18 lipids in membranes under the same ratiometric combinations of colipids that we tested here for the photolipids. Therefore, we collected AFM and fluorescence images of quaternary DOPC:Chol:SM:C18-sphingolipid mixtures and finally compared them with those of quaternary DOPC:Chol:SM:photolipid (all bilayers with a molar ratio of 10:6.7:5:5 and 0.1 mol % Atto6550DOPE). Such a comparison will ultimately give us a clearer picture on how biocompatible our photolipids are in relation to their natural counterparts.

As summarized in Fig. S18, most membranes with photolipids ended up showing equivalent phase-behavior properties when compared with membranes having their natural sphingolipid counterparts. Indeed, DOPC:Chol:SM membranes with 18.7 mol % azo-β-GalCer and azo-PhCer exhibited similar total L_o area (in *trans*) as well as similar L_d-L_o height deviation as membranes with 18.7 mol % 18:0-β-GalCer and 18:0-PhCer (native counterparts). Membranes with 18.7 mol % Azo-SM showed a similar total L_o area (in *trans*) yet a slightly smaller (~0.4 nm) but significant ($p < 0.001$) deviation in the L_d-L_o height mismatch compared with membranes with 18:0-SM.

A clearly different behavior was observed only for membranes with 18.7 mol % Azo-Cer, which did not exhibit any gel phase compared with their native 18:0-Cer counterpart. While L_d-L_o phase separation was observed for bilayers with 18:0-SM, 18:0-β-GalCer, and 18:0-PhCer, a gel phase (visible by AFM and fluorescence microscopy) was observed for membranes with 18:0-Cer instead. AFM analysis also shows that lipid bilayers with 18:0-Cer form a third L_o phase with an intermediate height (Fig. S18 *B*), which is consistent with previous results (10). However, apart from these differences, no significant variations can be observed when comparing the values of the recorded L_d-L_o height for both SLBs with azo-Cer or 18:0-Cer, as both membranes show a similar L_d-L_o mismatch height of 1.1 nm (Table S2).

Based on these last results, photolipids do not seem to behave dramatically differently from their native counterparts, at least in terms of their ability to maintain L_d-L_o phase separation and preserve their respective height deviation. This is very important information confirming that azobenzene-modified lipids are indeed biomimetic, or even bioequivalent, molecules and can therefore be considered a suitable option for manipulating native membrane properties.

CONCLUSIONS

In this work, we evaluated physicochemical foundations for the membrane remodeling ability by a family of photoswitchable sphingolipids, deciphering the relative contributions of the lipid headgroup and sphingoid backbone. We synthesized new types of *N*-acyl azobenzene sphingolipids with varying headgroup and sphingoid base functionalities. Then, we studied, with the help of atomic force and fluorescence microscopies, the propensity of these photolipids to alter membrane properties and laterally remodel L_d-L_o phase-separated supported membranes. Overall, we demonstrated that the headgroup type (simple hydroxyl versus more complex galactosyl or phosphocholine) does not interfere with the photoswitching ability of the various azo-sphingolipids within L_d-L_o lipid mixtures. Owing to the photodynamic reversibility of the azobenzene *N*-acyl chain, we further highlighted that *trans*-photolipids (i.e., dark-adapted and blue light-illuminated states) predominantly localize within preexisting L_o domains and compact membranes, while *cis*-photolipids (i.e., UV-A-illuminated state) preferentially locate within the more fluid L_d membrane regions and expand membranes.

Importantly, our results provide clear evidence that the nature of the sphingoid backbone, and its ability to engage stable H-bonding interactions with other colipids, plays a fundamental role in the way photoswitchable sphingolipids remodel L_d-L_o phase-separated membranes and change the amount, size, and height of L_o domains. Sphingosine- and phytospingosine-based lipids, with their free interfacial 3-OH and 4-OH hydroxyls, do not significantly alter the height of L_o domains when in the *trans*-isoform. In contrast, THP-protected lipids, with their interfacial 3-OH blocked, greatly interfere with the molecular packing and line tension of L_o domains, markedly reducing the overall L_o height mismatch. Whereas nonblocked azo-sphingolipids will promote a decrease of the total L_o phase area upon UV trigger, THP-protected azo-sphingolipids will increase the total L_o area, as well as induce a marked rise in L_o domain height after illumination with UV light.

Taken together, the structural diversity of the photoswitchable sphingolipids presented here, as well as an exquisite understanding of how these lipids alter important membrane properties, may offer new strategies for controlling the structure of biological lipid bilayers and the localization of membrane-interacting proteins. Thus, by further expanding the headgroup repertoire of photolipids, we may soon be in the position to target the fate of biologically relevant proteins on membranes using light as trigger. Such an endeavor would not only open up new, exciting avenues for optodynamic applications in the fields of synthetic biology, structural biology, or biophysics but would also offer novel perspectives toward the development of innovative photoresponsive drugs and pharmacological therapies.

SUPPORTING MATERIAL

Supporting material can be found online at https://doi.org/10.1016/j.bpj.2023.02.029.

AUTHOR CONTRIBUTIONS

H.G.F. and S.M.L. conducted the biophysical experiments and analyzed data. N.H. synthesized and purified most photolipids, in cooperation with N.W., H.T.-R., and J.A.F. P.S. and D.T. provided funding. D.T. supervised the synthesis of photolipids and H.G.F. their biophysical characterization. H.G.F., N.H., and S.M.L. prepared the first manuscript draft. All authors contributed to revision of the manuscript.

ACKNOWLEDGMENTS

The authors thank Sigrid Bauer for assistance in lipid handling and Alena Khmelinskaia for helpful discussions. The project was funded by the Deutsche Forschungsgemeinschaft (DFG)– SFB-1032 – Project ID 201269156. Additional support was provided by the Center for NanoScience (CeNS). H.G.F. and P.S. acknowledge financial support by the DFG within the SFB 863 (project ID 111166240). D.T. acknowledges the European Research Council (ERC Advanced Grant #268795, "CARV") and the DFG (SFB 749 and CIPSM) for generous funding. N.H. acknowledges financial support by the Deutsche Telekom Foundation and the LMUMentoring program. Further support was given to P.S. by the Max Planck Society and to H.G.F. by the STARK project 46SKD023X (Federal Ministry for Economic Affairs and Energy [BMWi] and Saxon State Ministry of Science and Art [SMWK]).

DECLARATION OF INTERESTS

The authors declare no competing interests.

REFERENCES

1. Hannun, Y. A., and L. M. Obeid. 2018. Sphingolipids and their metabolism in physiology and disease. *Nat. Rev. Mol. Cell Biol.* 19:175–191.
2. Marquês, J. T., H. S. Marinho, and R. F. M. de Almeida. 2018. Sphingolipid hydroxylation in mammals, yeast and plants – an integrated view. *Prog. Lipid Res.* 71:18–42.
3. van Meer, G., D. R. Voelker, and G. W. Feigenson. 2008. Membrane lipids: where they are and how they behave. *Nat. Rev. Mol. Cell Biol.* 9:112–124.
4. Baumgart, T., S. T. Hess, and W. W. Webb. 2003. Imaging coexisting fluid domains in biomembrane models coupling curvature and line tension. *Nature.* 425:821–824.
5. Veatch, S. L., and S. L. Keller. 2003. Separation of liquid phases in giant vesicles of ternary mixtures of phospholipids and cholesterol. *Biophys. J.* 85:3074–3083.
6. Kahya, N., D. Scherfeld, …, P. Schwille. 2003. Probing lipid mobility of raft-exhibiting model membranes by fluorescence correlation spectroscopy. *J. Biol. Chem.* 278:28109–28115.
7. de Almeida, R. F. M., A. Fedorov, and M. Prieto. 2003. Sphingomyelin/phosphatidylcholine/cholesterol phase diagram: boundaries and composition of lipid rafts. *Biophys. J.* 85:2406–2416.
8. Goñi, F. M., and A. Alonso. 2006. Biophysics of sphingolipids I. Membrane properties of sphingosine, ceramides and other simple sphingolipids. *Biochim. Biophys. Acta.* 1758:1902–1921.
9. Silva, L. C., R. F. M. de Almeida, …, M. Prieto. 2007. Ceramide-domain formation and collapse in lipid rafts: membrane reorganization by an apoptotic lipid. *Biophys. J.* 92:502–516.
10. Chiantia, S., N. Kahya, and P. Schwille. 2007. Raft domain reorganization driven by short- and long-chain ceramide: a combined AFM and FCS study. *Langmuir.* 23:7659–7665.
11. Castro, B. M., M. Prieto, and L. C. Silva. 2014. Ceramide: a simple sphingolipid with unique biophysical properties. *Prog. Lipid Res.* 54:53–67.
12. Kondo, N., Y. Ohno, …, A. Kihara. 2014. Identification of the phytosphingosine metabolic pathway leading to odd-numbered fatty acids. *Nat. Commun.* 5:5338.
13. Školová, B., A. Kováčik, …, K. Vávrová. 2017. Phytosphingosine, sphingosine and dihydrosphingosine ceramides in model skin lipid membranes: permeability and biophysics. *Biochim. Biophys. Acta Biomembr.* 1859:824–834.
14. Pruett, S. T., A. Bushnev, …, A. H. Merrill, Jr. 2008. Thematic review series: sphingolipids. Biodiversity of sphingoid bases ("sphingosines") and related amino alcohols. *J. Lipid Res.* 49:1621–1639.
15. Bieberich, E. 2018. Sphingolipids and lipid rafts: novel concepts and methods of analysis. *Chem. Phys. Lipids.* 216:114–131.
16. Simons, K., and W. L. C. Vaz. 2004. Model systems, lipid rafts, and cell membranes. *Annu. Rev. Biophys. Biomol. Struct.* 33:269–295.
17. Sezgin, E., I. Levental, …, C. Eggeling. 2017. The mystery of membrane organization: composition, regulation and roles of lipid rafts. *Nat. Rev. Mol. Cell Biol.* 18:361–374.
18. Levental, I., and S. Veatch. 2016. The continuing mystery of lipid rafts. *J. Mol. Biol.* 428:4749–4764.
19. Lorent, J. H., K. R. Levental, …, I. Levental. 2020. Plasma membranes are asymmetric in lipid unsaturation, packing and protein shape. *Nat. Chem. Biol.* 16:644–652.
20. Slotte, J. P. 2016. The importance of hydrogen bonding in sphingomyelin's membrane interactions with co-lipids. *Biochim. Biophys. Acta Biomembr.* 1858:304–310.
21. Mueller, V., C. Ringemann, …, C. Eggeling. 2011. STED nanoscopy reveals molecular details of cholesterol- and cytoskeleton-modulated lipid interactions in living cells. *Biophys. J.* 101:1651–1660.
22. Eggeling, C., C. Ringemann, …, S. W. Hell. 2009. Direct observation of the nanoscale dynamics of membrane lipids in a living cell. *Nature.* 457:1159–1162.
23. Chiantia, S., N. Kahya, and P. Schwille. 2005. Dehydration damage of domain-exhibiting supported bilayers: an AFM study on the protective effects of disaccharides and other stabilizing substances. *Langmuir.* 21:6317–6323.
24. Chiantia, S., N. Kahya, …, P. Schwille. 2006. Effects of ceramide on liquid-ordered domains investigated by simultaneous AFM and FCS. *Biophys. J.* 90:4500–4508.
25. Chiantia, S., J. Ries, …, P. Schwille. 2008. Role of ceramide in membrane protein organization investigated by combined AFM and FCS. *Biochim. Biophys. Acta.* 1778:1356–1364.
26. Franquelim, H. G., S. Chiantia, …, M. A. R. B. Castanho. 2011. Anti-HIV-1 antibodies 2F5 and 4E10 interact differently with lipids to bind their epitopes. *AIDS.* 25:419–428.
27. Visco, I., S. Chiantia, and P. Schwille. 2014. Asymmetric supported lipid bilayer formation via methyl-β-cyclodextrin mediated lipid exchange: influence of asymmetry on lipid dynamics and phase behavior. *Langmuir.* 30:7475–7484.
28. Boggs, J. M. 1987. Lipid intermolecular hydrogen bonding: influence on structural organization and membrane function. *Biochim. Biophys. Acta.* 906:353–404.
29. Kan, C. C., Z. S. Ruan, and R. Bittman. 1991. Interaction of cholesterol with sphingomyelin in bilayer membranes: evidence that the hydroxy group of sphingomyelin does not modulate the rate of cholesterol exchange between vesicles. *Biochemistry.* 30:7759–7766.
30. Mombelli, E., R. Morris, …, F. Fraternali. 2003. Hydrogen-bonding propensities of sphingomyelin in solution and in a bilayer assembly: a molecular dynamics study. *Biophys. J.* 84:1507–1517.
31. Björkbom, A., T. Róg, …, J. P. Slotte. 2010. Effect of sphingomyelin headgroup size on molecular properties and interactions with cholesterol. *Biophys. J.* 99:3300–3308.
32. Gater, D. L., V. Réat, …, V. Cherezov. 2013. Hydrogen bonding of cholesterol in the lipidic cubic phase. *Langmuir.* 29:8031–8038.
33. Artetxe, I., C. Sergelius, …, T. Maula. 2013. Effects of sphingomyelin headgroup size on interactions with ceramide. *Biophys. J.* 104: 604–612.
34. Guo, S., T. C. Moore, …, C. McCabe. 2013. Simulation study of the structure and phase behavior of ceramide bilayers and the role of lipid headgroup chemistry. *J. Chem. Theory Comput.* 9:5116–5126.
35. Yasuda, T., M. A. Al Sazzad, …, J. P. Slotte. 2016. The influence of hydrogen bonding on sphingomyelin/colipid interactions in bilayer membranes. *Biophys. J.* 110:431–440.
36. Björkbom, A., T. Róg, …, J. P. Slotte. 2011. N- and O-methylation of sphingomyelin markedly affects its membrane properties and interactions with cholesterol. *Biochim. Biophys. Acta.* 1808:1179–1186.
37. Frank, J. A., M. Moroni, …, D. Trauner. 2015. Photoswitchable fatty acids enable optical control of TRPV1. *Nat. Commun.* 6:7118.
38. Morstein, J., A. C. Impastato, and D. Trauner. 2021. Photoswitchable lipids. *Chembiochem.* 22:73–83.
39. Frank, J. A., H. G. Franquelim, …, D. Trauner. 2016. Optical control of lipid rafts with photoswitchable ceramides. *J. Am. Chem. Soc.* 138:12981–12986.
40. Hartrampf, N., T. Seki, …, D. Trauner. 2020. Optical control of cytokine production using photoswitchable galactosylceramides. *Chemistry.* 26:4476–4479.
41. Pritzl, S. D., P. Urban, …, T. Lohmüller. 2020. Photolipid bilayer permeability is controlled by transient pore formation. *Langmuir.* 36:13509–13515.
42. Morstein, J., M. Kol, …, D. Trauner. 2021. Short photoswitchable ceramides enable optical control of apoptosis. *ACS Chem. Biol.* 16:452–456.
43. Scheidt, H. A., K. Kolocaj, …, D. Huster. 2020. Light-induced lipid mixing implies a causal role of lipid splay in membrane fusion. *Biochim. Biophys. Acta Biomembr.* 1862, 183438.
44. Urban, P., S. D. Pritzl, …, T. Lohmueller. 2020. A lipid photoswitch controls fluidity in supported bilayer membranes. *Langmuir.* 36: 2629–2634.

45. Urban, P., S. D. Pritzl, …, T. Lohmüller. 2018. Light-controlled lipid interaction and membrane organization in photolipid bilayer vesicles. *Langmuir.* 34:13368–13374.
46. Pernpeintner, C., J. A. Frank, …, T. Lohmüller. 2017. Light-controlled membrane mechanics and shape transitions of photoswitchable lipid vesicles. *Langmuir.* 33:4083–4089.
47. Bryan, A. M., J. K. You, …, M. Del Poeta. 2021. Cholesterol and sphingomyelin are critical for Fcγ receptor–mediated phagocytosis of Cryptococcus neoformans by macrophages. *J. Biol. Chem.* 297, 101411.
48. Römer, W., L. Berland, …, L. Johannes. 2007. Shiga toxin induces tubular membrane invaginations for its uptake into cells. *Nature.* 450:670–675.
49. Holmgren, J., I. Lönnroth, …, L. Svennerholm. 1975. Interaction of cholera toxin and membrane GM1 ganglioside of small intestine. *Proc. Natl. Acad. Sci. USA.* 72:2520–2524.
50. Ewers, H., W. Römer, …, L. Johannes. 2010. GM1 structure determines SV40-induced membrane invagination and infection. *Nat. Cell Biol.* 12:11–18.
51. Cook, D. G., J. Fantini, …, F. Gonzalez-Scarano. 1994. Binding of human immunodeficiency virus type I (HIV-1) Gp120 to galactosylceramide (GalCer): relationship to the V3 loop. *Virology.* 201:206–214.
52. García-Sáez, A. J., S. Chiantia, and P. Schwille. 2007. Effect of line tension on the lateral organization of lipid membranes. *J. Biol. Chem.* 282:33537–33544.
53. Kuzmin, P. I., S. A. Akimov, …, F. S. Cohen. 2005. Line tension and interaction energies of membrane rafts calculated from lipid splay and tilt. *Biophys. J.* 88:1120–1133.
54. García-Sáez, A. J., S. Chiantia, …, P. Schwille. 2007. Pore Formation by a Bax-derived peptide: effect on the line tension of the membrane probed by AFM. *Biophys. J.* 93:103–112.
55. Franquelim, H. G., D. Gaspar, …, M. A. R. B. Castanho. 2013. Decoding distinct membrane interactions of HIV-1 fusion inhibitors using a combined atomic force and fluorescence microscopy approach. *Biochim. Biophys. Acta.* 1828:1777–1785.
56. Schmidt, R. R., and P. Zimmermann. 1986. Synthesis of glycosphingolipids and psychosines. *Angew. Chem. Int. Ed. Engl.* 25:725–726.
57. Kol, M., B. Williams, …, J. A. Frank. 2019. Optical manipulation of sphingolipid biosynthesis using photoswitchable ceramides. *Elife.* 8, e43230.
58. Frolov, V. A. J., Y. A. Chizmadzhev, …, J. Zimmerberg. 2006. "Entropic traps" in the kinetics of phase separation in multicomponent membranes stabilize nanodomains. *Biophys. J.* 91:189–205.
59. An, H., M. R. Nussio, …, J. G. Shapter. 2010. Material properties of lipid microdomains: force-volume imaging study of the effect of cholesterol on lipid microdomain rigidity. *Biophys. J.* 99:834–844.
60. Unsay, J. D., K. Cosentino, and A. J. García-Sáez. 2015. Atomic force microscopy imaging and force spectroscopy of supported lipid bilayers. *J. Vis. Exp.*e52867 https://doi.org/10.3791/52867.
61. Bhojoo, U., M. Chen, and S. Zou. 2018. Temperature induced lipid membrane restructuring and changes in nanomechanics. *Biochim. Biophys. Acta Biomembr.* 1860:700–709.
62. Lister, M. D., Z. S. Ruan, and R. Bittman. 1995. Interaction of sphingomyelinase with sphingomyelin analogs modified at the C-1 and C-3 positions of the sphingosine backbone. *Biochim. Biophys. Acta.* 1256:25–30.
63. Mills, T. T., G. E. S. Toombes, …, J. F. Nagle. 2008. Order parameters and areas in fluid-phase oriented lipid membranes using wide angle X-ray scattering. *Biophys. J.* 95:669–681.
64. Lipowsky, R. 1993. Domain-induced budding of fluid membranes. *Biophys. J.* 64:1133–1138.
65. Vind-Kezunovic, D., C. H. Nielsen, …, R. Gniadecki. 2008. Line tension at lipid phase boundaries regulates formation of membrane vesicles in living cells. *Biochim. Biophys. Acta.* 1778:2480–2486.
66. Yang, S.-T., V. Kiessling, and L. K. Tamm. 2016. Line tension at lipid phase boundaries as driving force for HIV fusion peptide-mediated fusion. *Nat. Commun.* 7, 11401.
67. Schäfer, L. V., and S. J. Marrink. 2010. Partitioning of lipids at domain boundaries in model membranes. *Biophys. J.* 99:L91–L93.
68. Brewster, R., and S. A. Safran. 2010. Line active hybrid lipids determine domain size in phase separation of saturated and unsaturated lipids. *Biophys. J.* 98:L21–L23.
69. Yamamoto, T., and S. A. Safran. 2011. Line tension between domains in multicomponent membranes is sensitive to degree of unsaturation of hybrid lipids. *Soft Matter.* 7:7021–7033.
70. Li, Z., and A. A. Gorfe. 2014. Modulation of a small two-domain lipid vesicle by linactants. *J. Phys. Chem. B.* 118:9028–9036.
71. Shimokawa, N., M. Nagata, and M. Takagi. 2015. Physical properties of the hybrid lipid POPC on micrometer-sized domains in mixed lipid membranes. *Phys. Chem. Chem. Phys.* 17:20882–20888.
72. Heberle, F. A., R. S. Petruzielo, …, J. Katsaras. 2013. Bilayer thickness mismatch controls domain size in model membranes. *J. Am. Chem. Soc.* 135:6853–6859.
73. Hassan-Zadeh, E., E. Baykal-Caglar, …, J. Huang. 2014. Complex roles of hybrid lipids in the composition, order, and size of lipid membrane domains. *Langmuir.* 30:1361–1369.
74. Usery, R. D., T. A. Enoki, …, G. W. Feigenson. 2017. Line tension controls liquid-disordered + liquid-ordered domain size transition in lipid bilayers. *Biophys. J.* 112:1431–1443.
75. Tsai, W.-C., and G. W. Feigenson. 2019. Lowering line tension with high cholesterol content induces a transition from macroscopic to nanoscopic phase domains in model biomembranes. *Biochim. Biophys. Acta Biomembr.* 1861:478–485.
76. Lin, W.-C., C. D. Blanchette, and M. L. Longo. 2007. Fluid-phase chain unsaturation controlling domain microstructure and phase in ternary lipid bilayers containing GalCer and cholesterol. *Biophys. J.* 92:2831–2841.
77. Koukalová, A., M. Amaro, …, R. Šachl. 2017. Lipid driven nanodomains in giant lipid vesicles are fluid and disordered. *Sci. Rep.* 7:5460.
78. Urban, P. 2021. Optical control of lipid interaction in photolipid membranes. *In* Doctoral Dissertation, pp. 61–63. https://doi.org/10.5282/edoc.29084.
79. Butt, H.-J., and V. Franz. 2002. Rupture of molecular thin films observed in atomic force microscopy. I. Theory. *Phys. Rev. E Stat. Nonlin. Soft Matter Phys.* 66, 031601.
80. Loi, S., G. Sun, V. Franz, and H.-J. Butt. 2002. Rupture of molecular thin films observed in atomic force microscopy. II. Experiment. *Phys. Rev. E Stat. Nonlin. Soft Matter Phys.* 66, 031602.
81. Garcia-Manyes, S., L. Redondo-Morata, …, F. Sanz. 2010. Nanomechanics of lipid bilayers: heads or tails? *J. Am. Chem. Soc.* 132:12874–12886.
82. Sullan, R. M. A., J. K. Li, …, S. Zou. 2010. Cholesterol-dependent nanomechanical stability of phase-segregated multicomponent lipid bilayers. *Biophys. J.* 99:507–516.
83. Chiantia, S., J. Ries, …, P. Schwille. 2006. Combined AFM and two-focus SFCS study of raft-exhibiting model membranes. *Chemphyschem.* 7:2409–2418.
84. Domingues, M. M., B. Gomes, …, N. C. Santos. 2021. 25-Hydroxycholesterol effect on membrane structure and mechanical properties. *Int. J. Mol. Sci.* 22, 2574.
85. Socrier, L., S. Ahadi, …, C. Steinem. 2023. Optical manipulation of Gb3 enriched lipid domains: impact of isomerization on Gb3-Shiga toxin B interaction. *Chemistry.* 29:e202202766.
86. Goñi, F. M., and A. Alonso. 2009. Effects of ceramide and other simple sphingolipids on membrane lateral structure. *Biochim. Biophys. Acta.* 1788:169–177.
87. Carreira, A. C., A. E. Ventura, …, L. C. Silva. 2015. Tackling the biophysical properties of sphingolipids to decipher their biological roles. *Biol. Chem.* 396:597–609.
88. Castro, B. M., L. C. Silva, …, M. Prieto. 2009. Cholesterol-rich fluid membranes solubilize ceramide domains: implications for the structure and dynamics of mammalian intracellular and plasma membranes. *J. Biol. Chem.* 284:22978–22987.

Biophysical Journal, Volume *122*

Supplemental information

Structural diversity of photoswitchable sphingolipids for optodynamic control of lipid microdomains

Nina Hartrampf, Samuel M. Leitao, Nils Winter, Henry Toombs-Ruane, James A. Frank, Petra Schwille, Dirk Trauner, and Henri G. Franquelim

Supporting Material

Structural Diversity of Photoswitchable Sphingolipids for Optodynamic Control of Lipid Microdomains

Nina Hartrampf,[1,2,‡] Samuel M. Leitao,[3,4,‡] Nils Winter,[1] Henry Toombs-Ruane,[1]

James A. Frank,[1,5] Petra Schwille,[3] Dirk Trauner,[1,6,a,*] Henri G. Franquelim,[3,b,*]

1) Department of Chemistry, Ludwig Maximilian University of Munich, Munich 81377, Germany; 2) Department of Chemistry, University of Zurich, Zurich 8057, Switzerland; 3) Cellular and Molecular Biophysics Department, Max Planck Institute of Biochemistry, Martinsried 82152, Germany; 4) Institute for Bioengineering, École Polytechnique Fédérale de Lausanne, Lausanne 1015, Switzerland; 5) Vollum Institute, Oregon Health & Science University, Portland, OR 97239, United States; 6) Department of Chemistry, New York University, New York City, NY 10003, United States.

‡ Co-authors with equal contribution

* Corresponding authors: HGF (hgfranq@biochem.mpg.de) & DT (dirktrauner@nyu.edu)

a) Present address DT: Department of Chemistry, University of Pennsylvania, Philadelphia, PA 19104. E-mail: dtrauner@upenn.edu

b) Present address HGF: Interfaculty Centre for Bioactive Matter, Leipzig University, Leipzig 04103, Germany. E-mail: henri.franquelim@uni-leipzig.de

Table of Contents

Supplementary figures

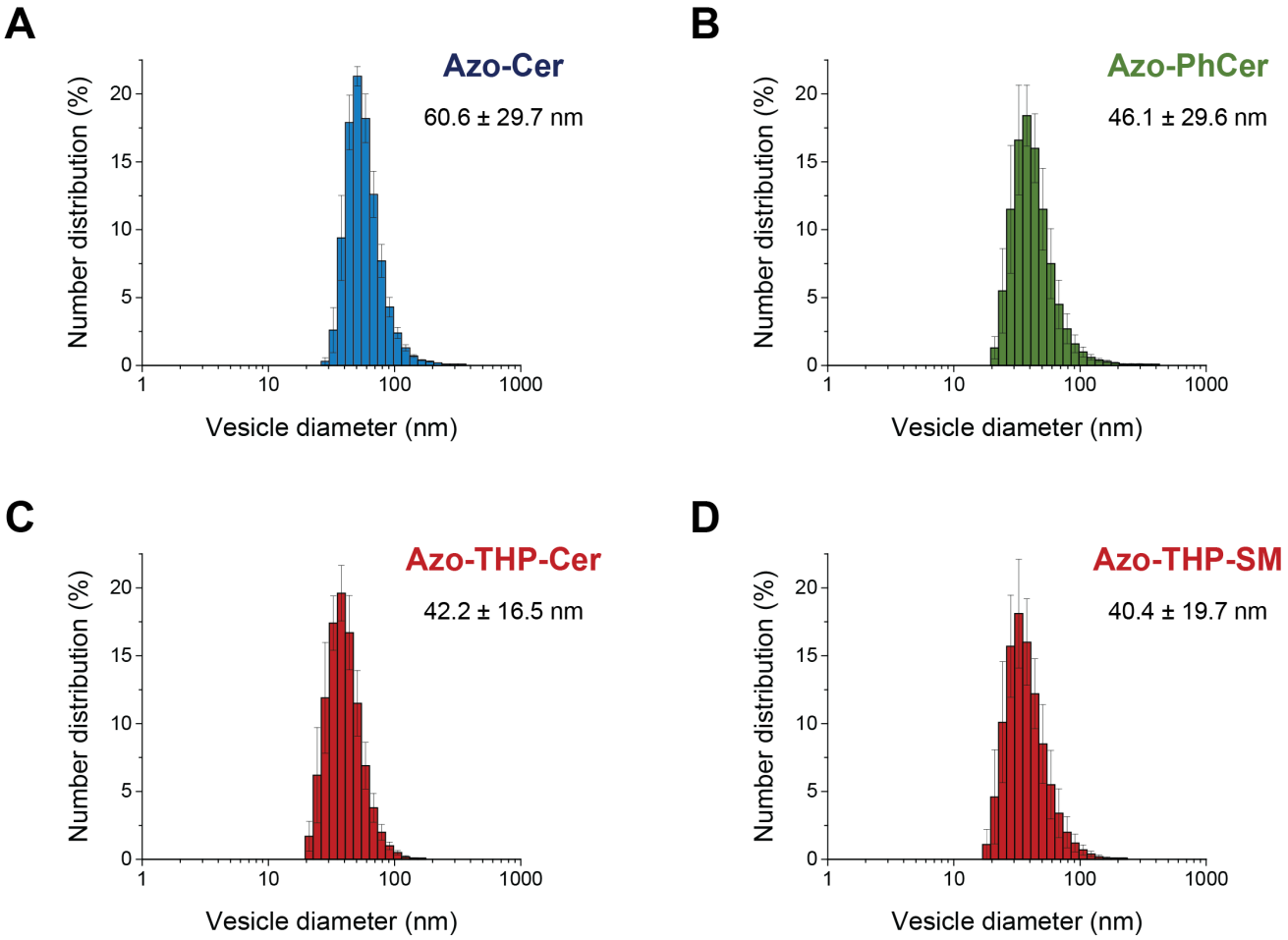

Figure S1 – Dynamic light scattering (DLS) of small unilamellar vesicles (SUVs) with azo-sphingolipids. Size distributions of SUVs composed of DOPC:Chol:SM:photolipid (10:6.7:5:5, mol ratio) containing (A) Azo-Cer, (B) Azo-PhCer, (C) Azo-THP-Cer and (D) Azo-THP-SM. Indicated are the number-normalized diameters of the sonicated SUVs, which ranged from 40 to 60 nm. In addition, the measured average polydispersity index (PDI) was here 0.34 ± 0.03.

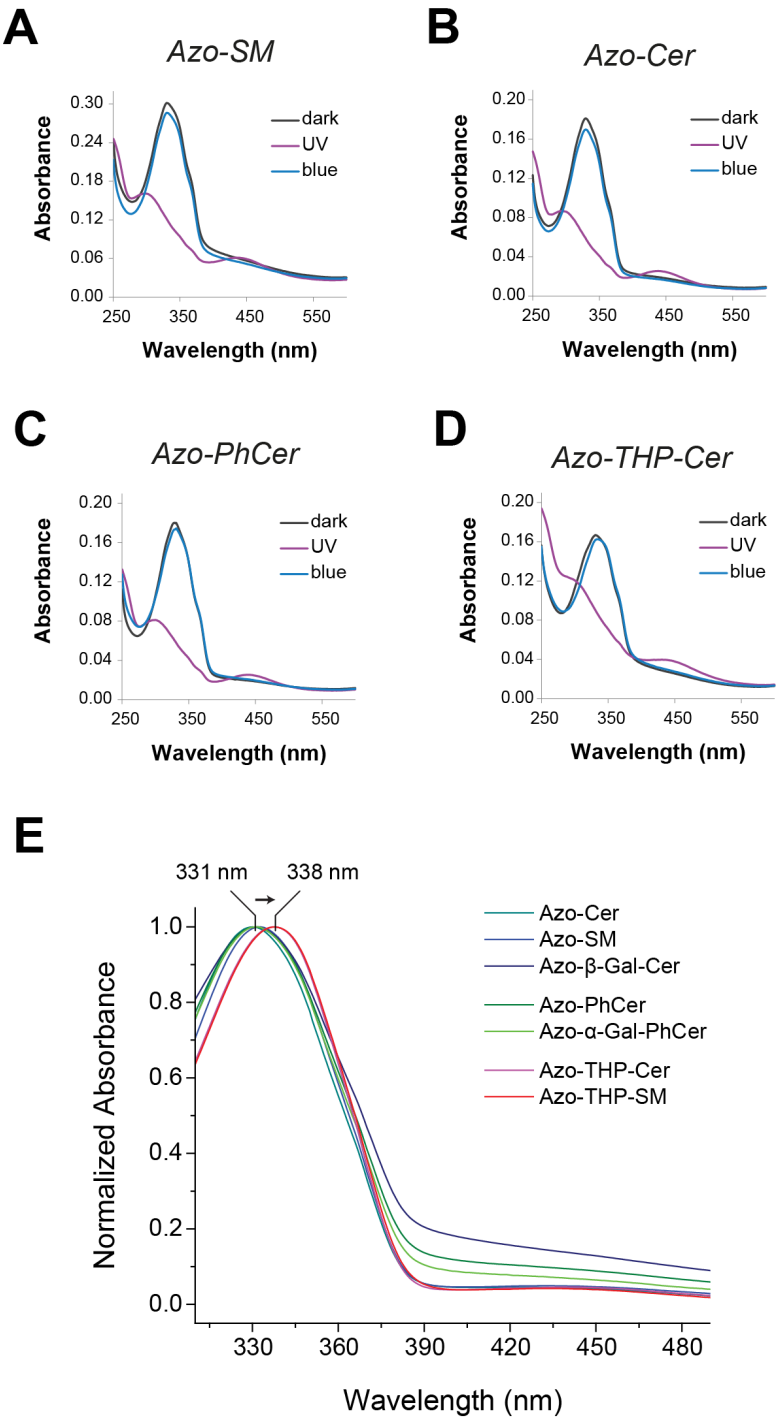

Figure S2 – UV-Vis absorbance spectra of azo-sphingolipids incorporated in small liposomes. (A) Azo-SM, (B) Azo-Cer, (C) Azo-PhCer and (D) Azo-THP-Cer. Black curves correspond to the spectra of the photolipids at their dark-adapted state (black curves), purple curves to the spectra after shining with UV-A light (λ = 365 nm) and blue curves after applying blue light (λ = 470 nm). (E) Normalized spectra after solubilization of liposomes with 0.1% (v/v) Triton X-100 for scattering correction. Azo-THP-SM and Azo-THP-Cer have a maximum peak at 338 nm, while the other photolipids have their maximum peak at 331 nm.

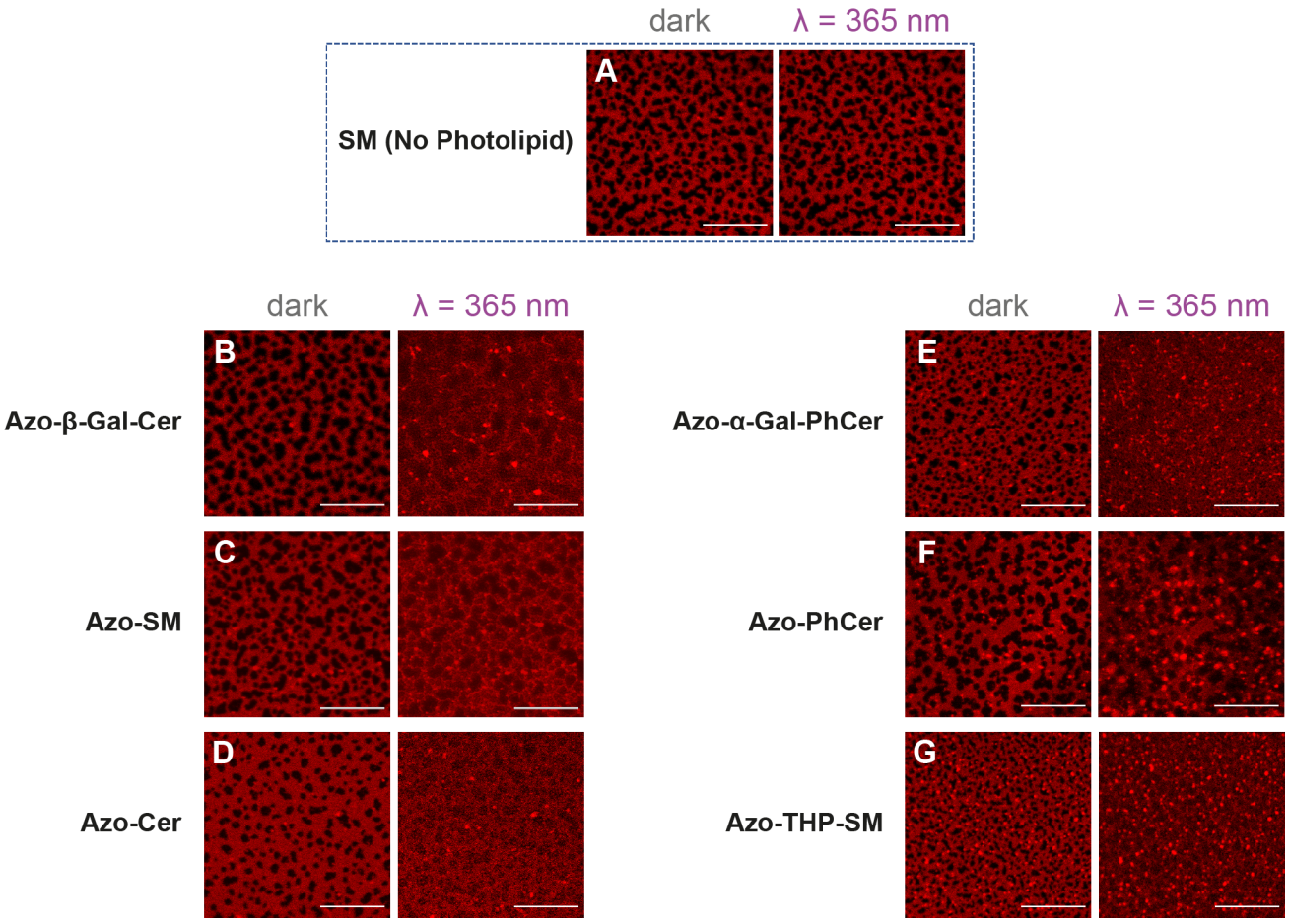

Figure S3 – Remodeling of phase-separated supported lipid bilayers (SLBs) containing azo-sphingolipids directly after irradiation with UV-A light. Fluorescence confocal images showing the admixing of the L_d-L_o lipid phases on SLBs composed of DOPC:Chol:SM:photolipid (10:6.7:5:5 mol ratio), doped with 0.1 mol% Atto655-DOPE (for fluorescence detection of L_d phase), before and directly after illumination with UV-A light (λ = 365 nm). (A) Control sample without photolipid (DOPC:Chol:SM (10:6.7:10 mol ratio)). Samples with 18.7 mol% (B) Azo-β-Gal-Cer, (C) Azo-SM, (D) Azo-Cer, (E) Azo-α-Gal-PhCer, (F) Azo-PhCer and (G) Azo-THP-SM. At the dark-adapted state, dark areas on the images correspond to the L_o phase, the fluorescently red matrix to the L_d phase and the very bright spots are unfused SUVs on the membranes. Scale-bar is 20 μm.

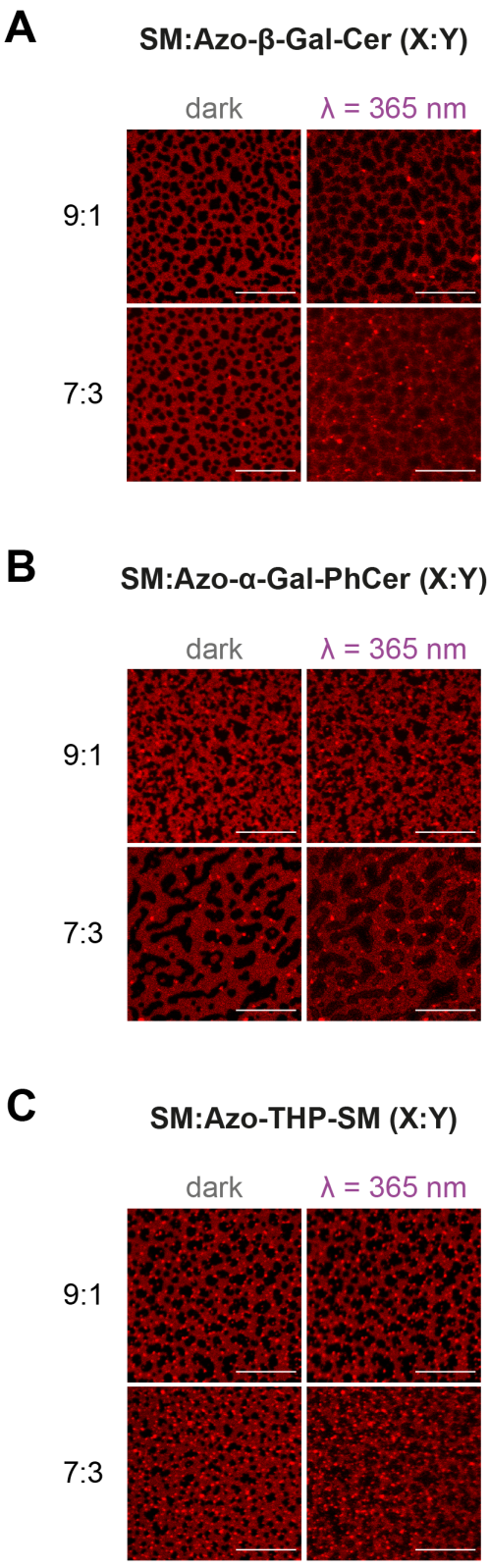

Figure S4 – Admixing of L_d-L_o directly after irradiation with UV-A light on membranes with lower amounts of azo-sphingolipids. Fluorescence confocal images of SLBs composed of DOPC:Chol:SM:photolipid (10:6.7:X:Y mol ratio), doped with 0.1 mol% Atto655-DOPE (for fluorescence detection of L_d phase), before and directly after illumination with UV-A light (λ = 365 nm). Samples with (A) Azo-β-Gal-Cer, (B) Azo-α-Gal-PhCer and (C) Azo-THP-SM at 3.7 mol% (SM:photolipid, X:Y = 9:1) or 11.2 mol% (SM:photolipid, X:Y = 7:3). Scale-bar is 20 µm.

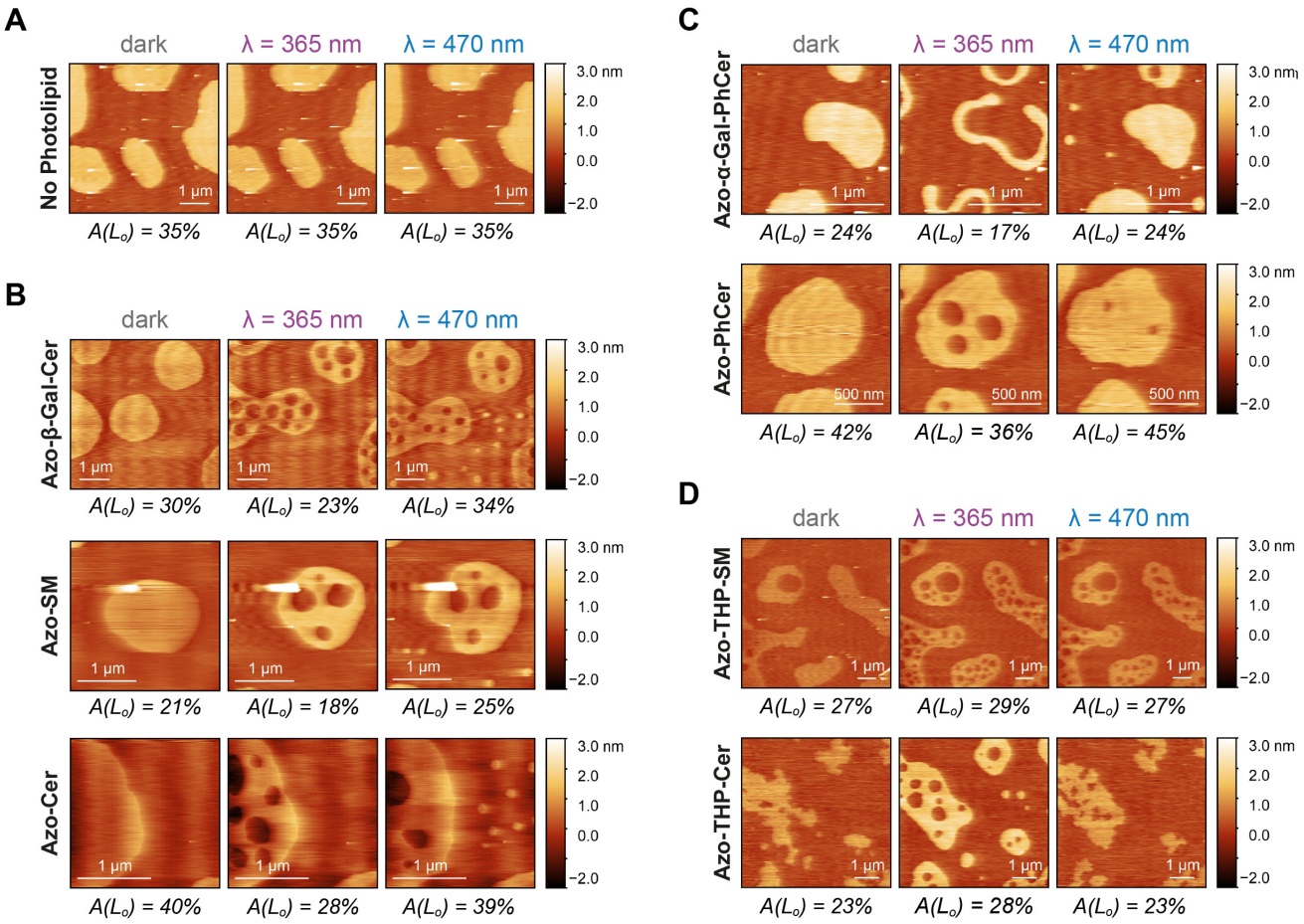

Figure S5 – Additional high-speed AFM height images of phase-separated supported bilayers containing different types of azo-sphingolipids upon light trigger. Changes in the area of L_o domains (of depicted snapshots) before and directly after brief illumination with UV-A (λ = 365 nm) and blue (λ = 470 nm) lights on DOPC:Chol:SM:photolipid (10:6.7:5:5 mol ratio) SLBs having different types of photoswitchable lipids. ***(A) without azo-sphingolipid***: control with SM; mixture being DOPC:Chol:SM (10:6.7:10 mol ratio). ***(B) with spingosine-based azo-sphingolipids***: Azo-β-Gal-Cer, Azo-SM or Azo-Cer. ***(C) with phytospingosine-based azo-sphingolipids***: Azo-α-Gal-PhCer or Azo-PhCer. ***(D) samples with 3-OH-blocked azo-sphingolipids***: Azo-THP-SM or Azo-THP-Cer.

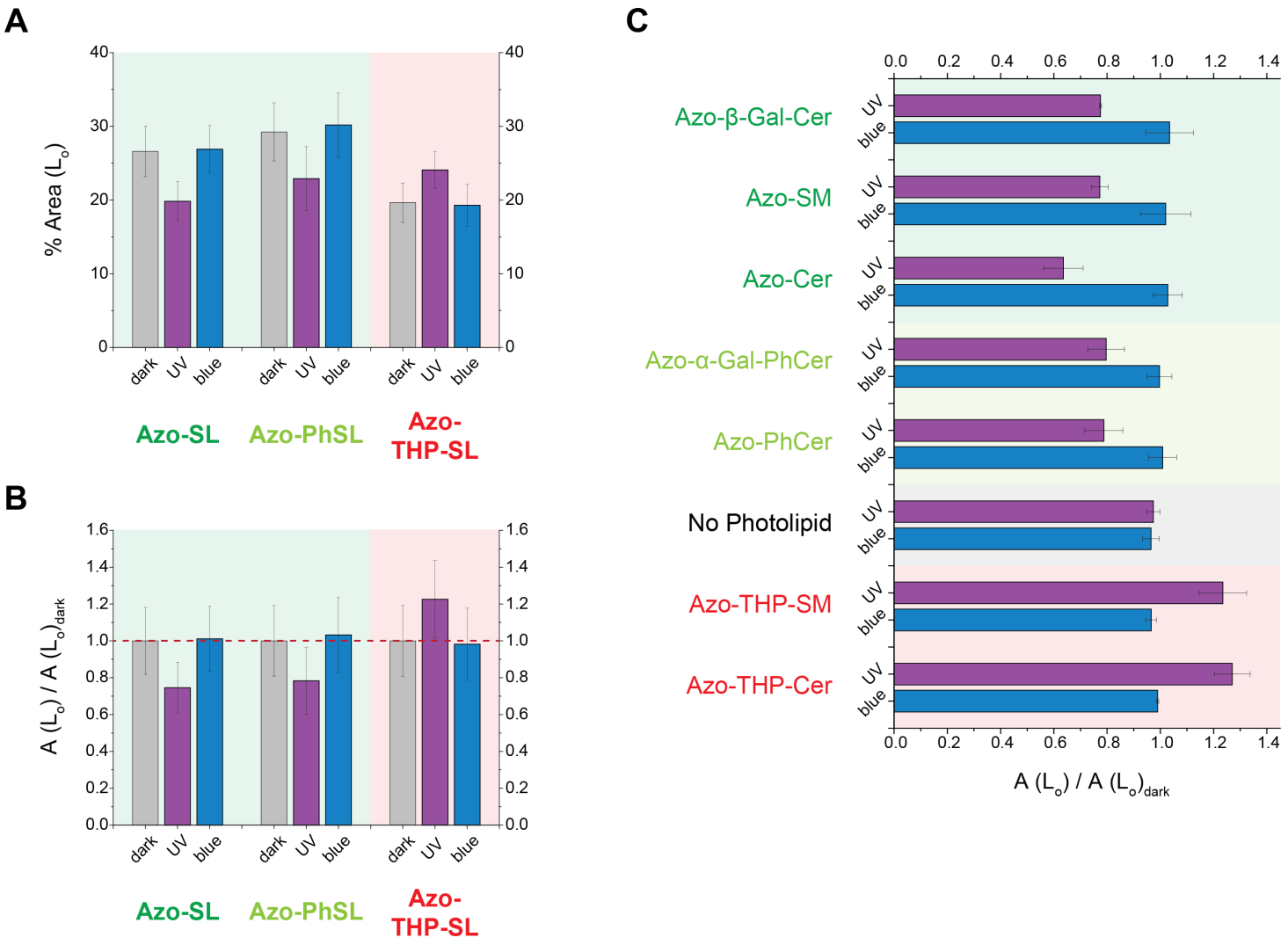

Figure S6 – Average L_o areas of phase-separated SLBs containing photoswitchable sphingolipids recovered from high-speed AFM images in Figures. 2, 3 and S5. Non-normalized (A) and normalized (B) L_o areas of grouped and (C) normalized non-grouped SLBs containing azo-sphingolipids Azo-β-Gal-Cer, Azo-SM and Azo-Cer (Azo-SL), azo-phytosphingolipids Azo-α-Gal-PhCer and Azo-PhCer (Azo-PhSL), and THP-protected azo-sphingolipids Azo-THP-SM and Azo-THP-Cer (Azo-THP-SL). Grey bars corresponds to average values at the dark-adapted state, purple bars to the average values after irradiation with UV-A light (λ = 365 nm), and blue bars to values after irradiation with blue light (λ = 470 nm). Columns relative to photolipids with free 3-OH (i.e. Azo-SL and Azo-PhSL) are marked in green, while columns relative to photolipids with blocked-3-OH (i.e. Azo-THP-SL) are marked in red. Error bars correspond to standard error of the mean (*n* = 4-7 high-speed AFM images each).

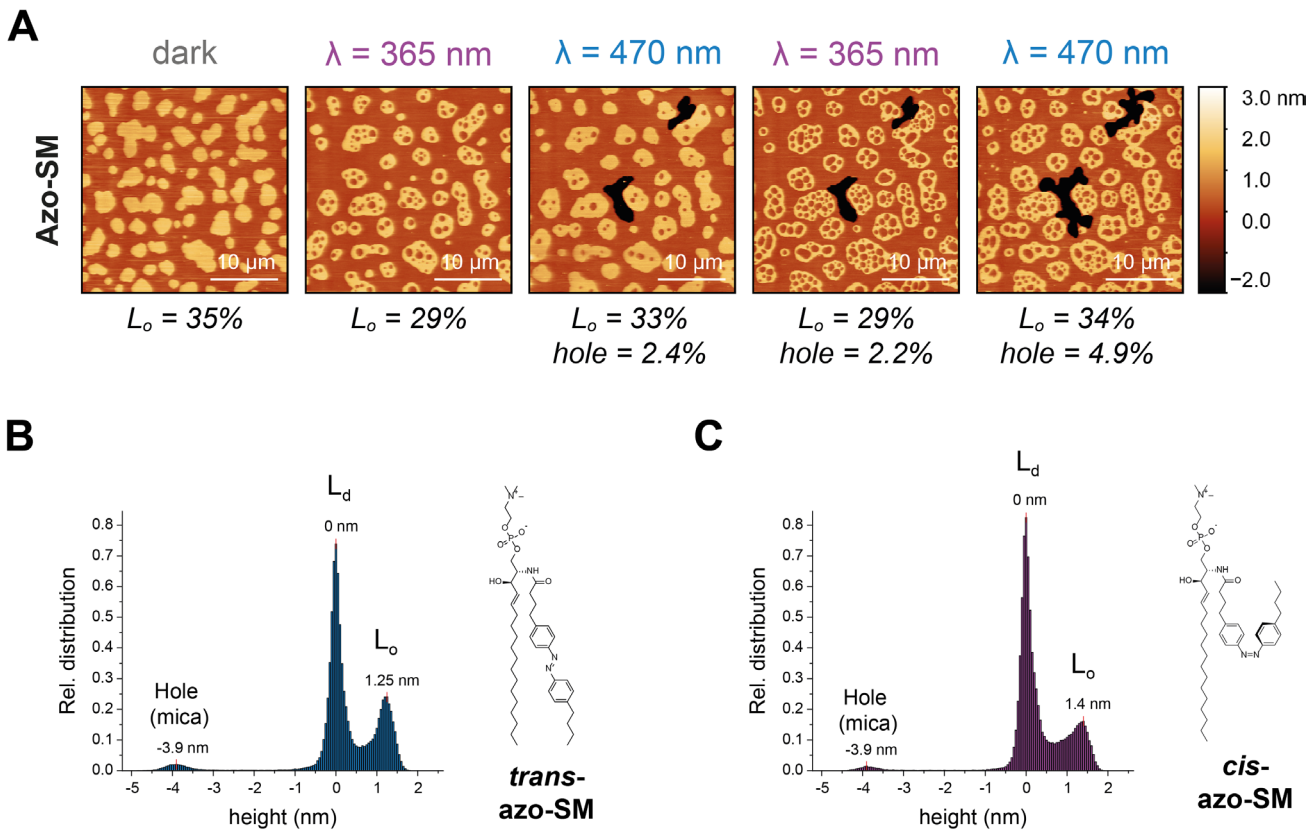

Figure S7 – Reshuffling of L_d-L_o phase separation and membrane expansion/compaction triggered by the photo-isomerization of Azo-SM. (A) Sequential AFM images of DOPC:Chol:SM:Azo-SM (10:6.7:5:5 mol ratio) SLB undergoing phase reshuffling and hole expansion/compaction upon applying UV-A (λ = 365 nm) and blue (λ = 470 nm) lights. Areas of L_o phase and membrane holes on the individual images are additionally depicted. (B, C) Height distribution histograms extracted from images above when Azo-SM was in the (B) *trans*- (blue-adapted) and (C) *cis*- (UV-adapted) states, respectively. Peaks correspond to the height level of the holes (mica surface, -3.9 nm), L_d (0 nm) and L_o (1.25 / 1.4 nm) phases, as marked.

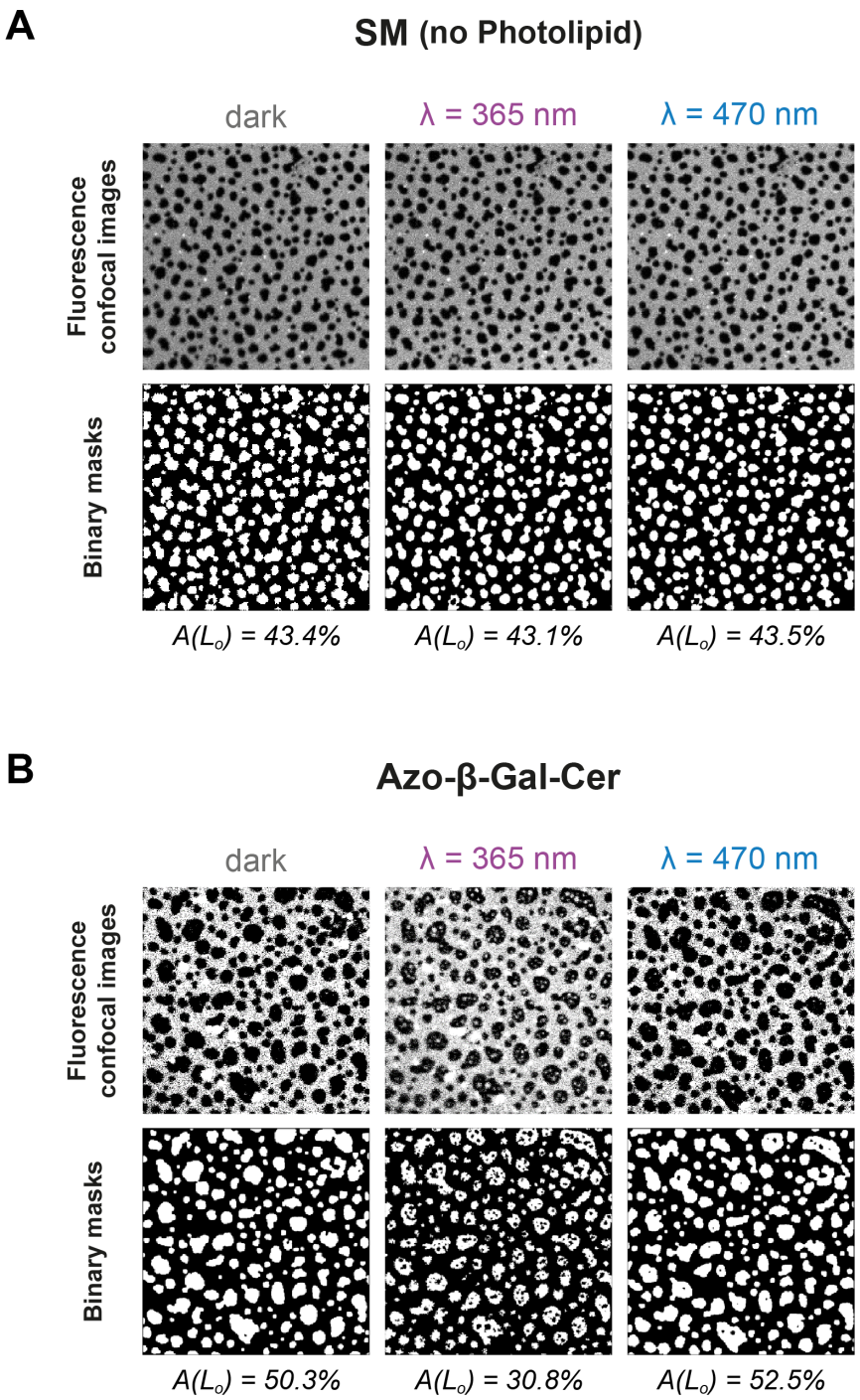

Figure S8 – Quantification of the amount of L_d-L_o area from fluorescence confocal data. Example of fluorescence confocal images, generated binary masks and recovered L_o phase area values for (A) DOPC:Chol:SM (10:6.7:10) control SLBs lacking photoswitchable sphingolipids, as well as (B) DOPC:Chol:SM:Azo-β-GalCer (10:6.7:5:5) SLBs having a sphingosine-based photoswitchable sphingolipid, prior and 20 min after brief illumination with UV-A (λ = 365 nm) and blue (λ = 470 nm) lights. Microscopy images correspond to large fields-of-view (56.7 × 56.7 μm^2) of SLBs having 0.1 mol% Atto655-DOPE for fluorescence detection of the L_d phase.

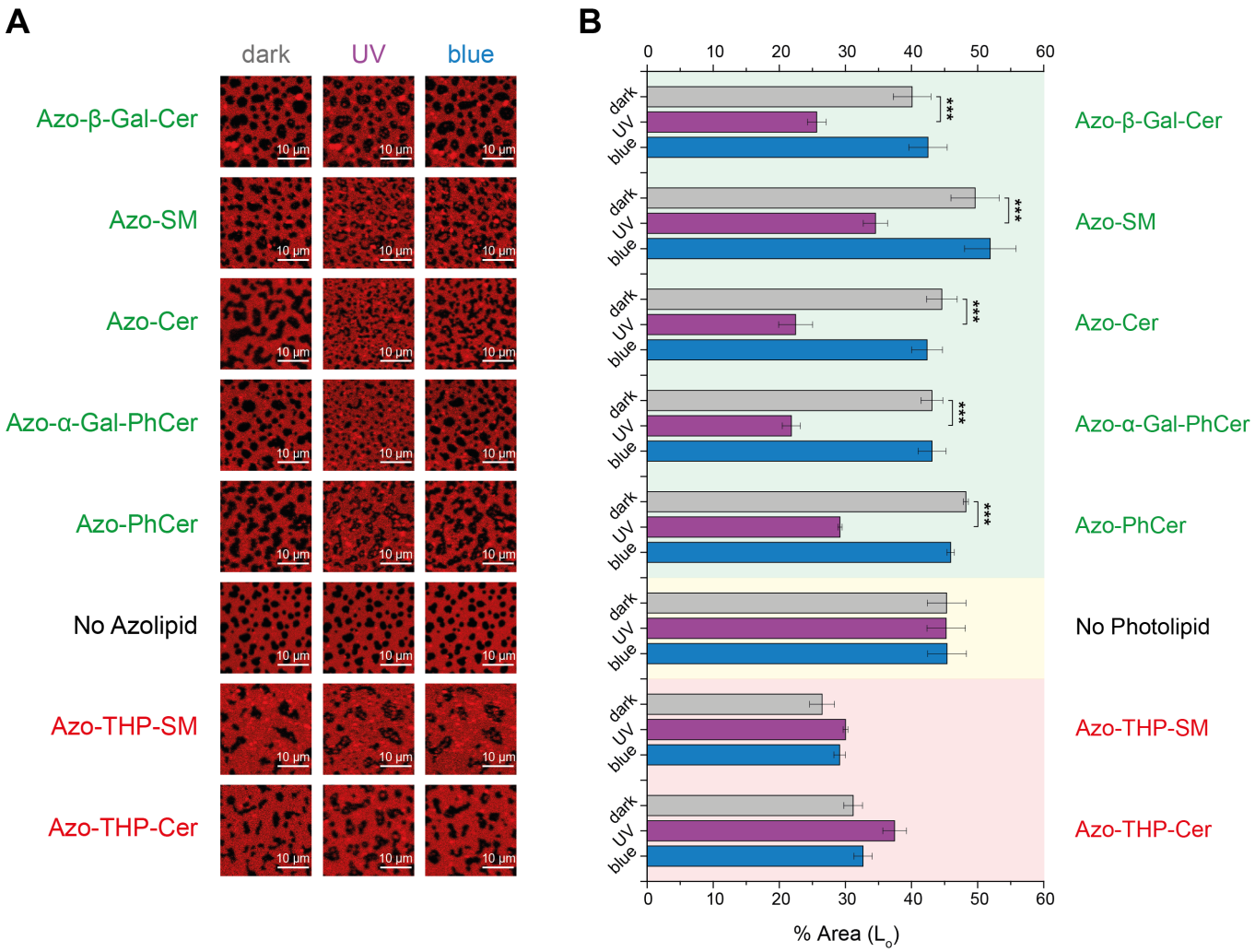

Figure S9 – Percentage of L_o phase area retrieved from fluorescence confocal images prior and 20 min after brief illumination with UV-A (λ = 365 nm) and blue (λ = 470 nm) lights. (A) Microscopy images of DOPC:Chol:SM:photolipid (10:6.7:5:5 mol ratio) and control (no photolipid; 10:6.7:10 mol ratio) SLBs, doped with 0.1 mol% Atto655-DOPE for fluorescence detection. (B) Average percentage of L_o phase retrieved for phase-separated SLBs containing either azo-(phyto)sphingolipids with free 3-OH (marked in green), no photolipid (controls with SM, marked in yellow), or THP-protected azo-sphingolipids with the 3-OH blocked (marked in red). Error bars correspond to the standard error of the mean (*n* = 5-8 confocal images each). Statistical analysis: UV- vs. dark-adapted states (*** p-value < 0.001).

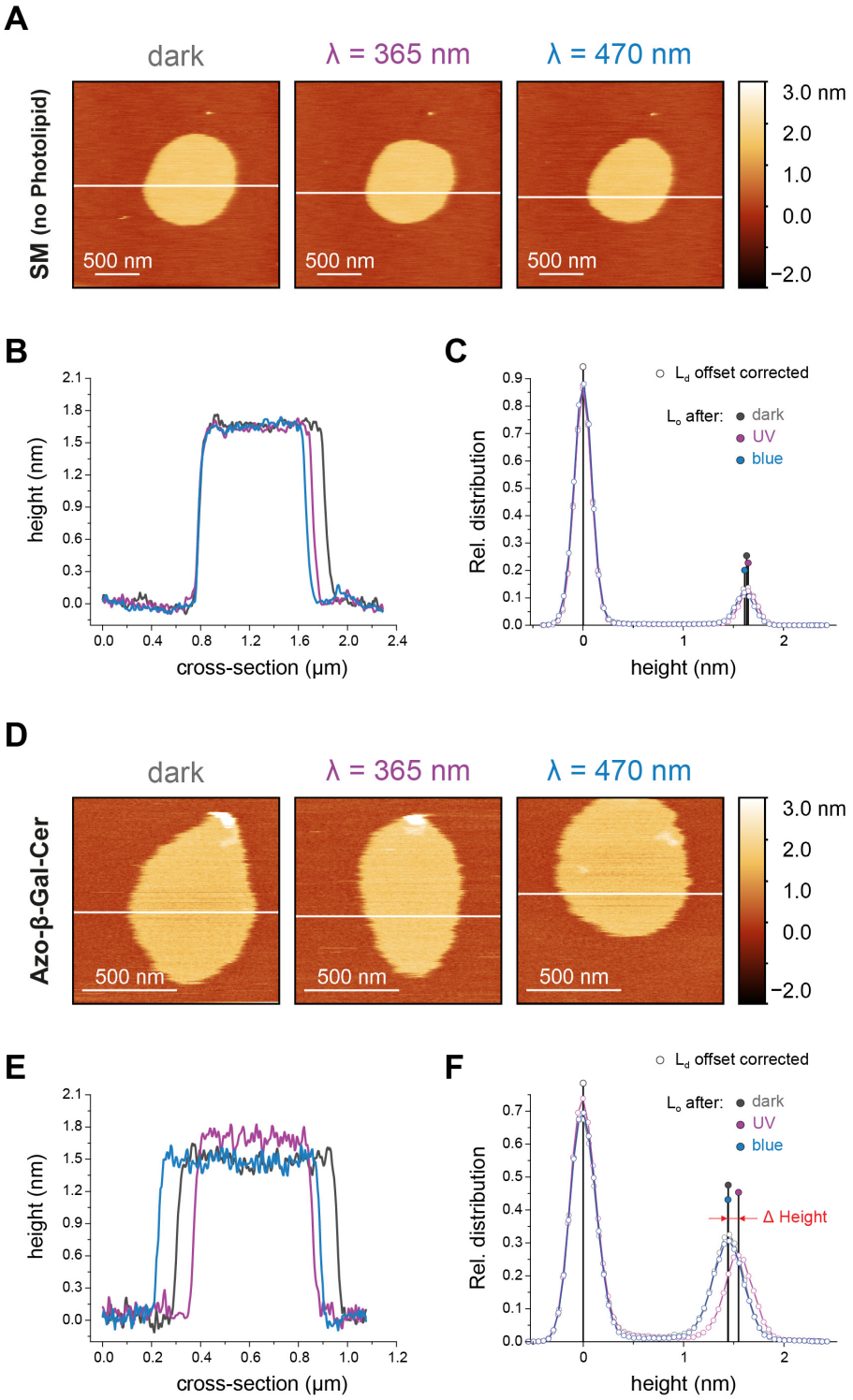

Figure S10 – Quantification of the L_d-L_o height difference from AFM data. (A, D) Example of AFM height images for phase-separated (A) DOPC:Chol:SM (10:6.7:10) control SLBs lacking photoswitchable sphingolipids, as well as (D) DOPC:Chol:SM:Azo-β-GalCer (10:6.7:5:5) SLBs having a sphingosine-based photoswitchable sphingolipid, prior and 20 min after brief illumination with UV-A (λ = 365 nm) and blue (λ = 470 nm) lights. **(B, E)** Cross-sections (from white lines marked in A, D) and height distribution **(C, F)** profiles for the displayed membranes lacking photolipid (B) and with Azo-β-GalCer (E) at the dark-, UV- and blue-adapted states, with the L_d (centered at 0 nm) and L_o (1.4-1.7 nm) phase height peaks accordingly marked

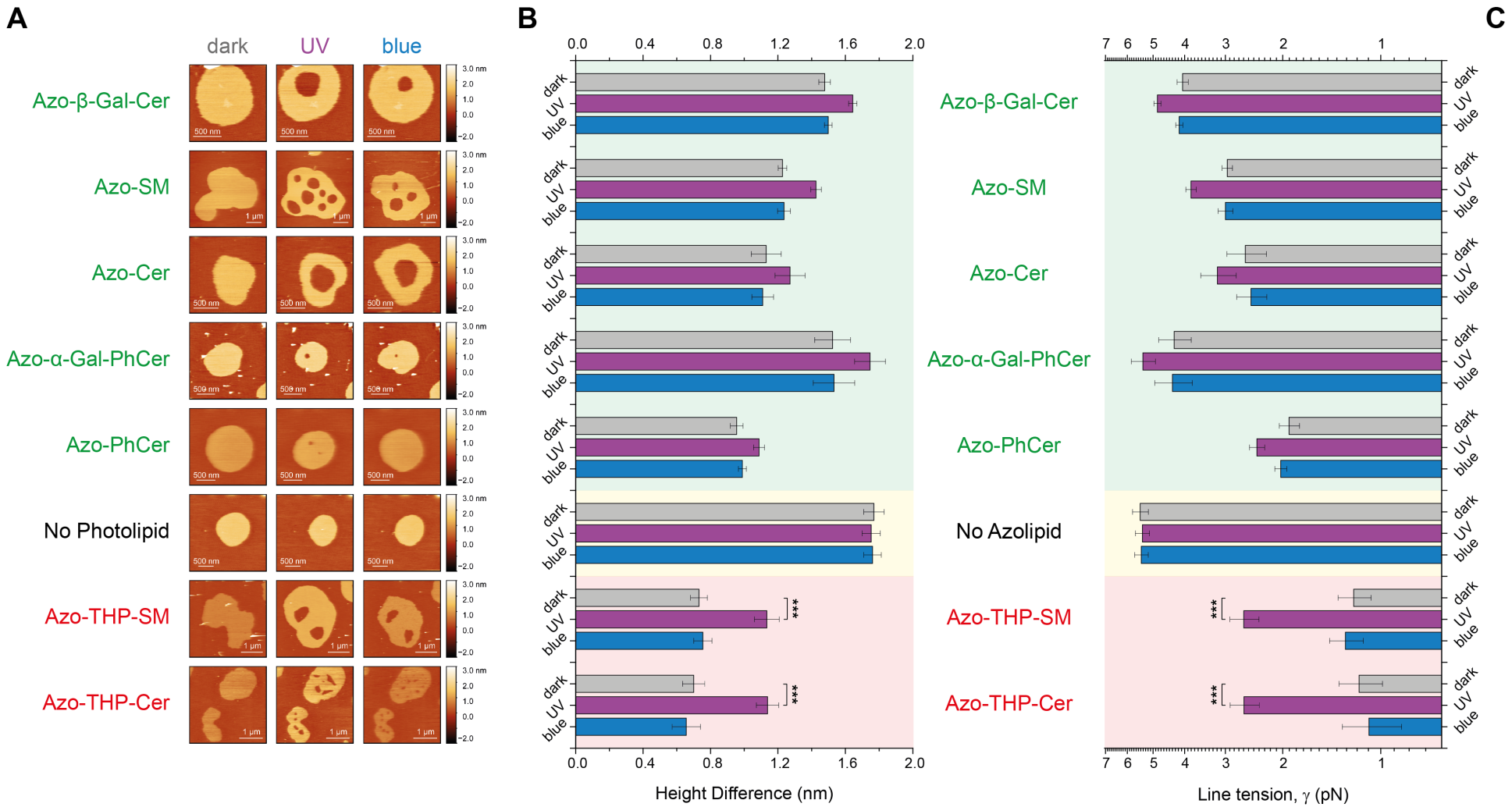

Figure S11 – L_d-L_o height difference and line tension values retrieved from AFM images prior and 20 min after brief illumination with UV-A (λ = 365 nm) and blue (λ = 470 nm) lights. (A) Slow-speed AFM height images of DOPC:Chol:SM:photolipid (10:6.7:5:5 mol ratio) and control (no photolipid; 10:6.7:10 mol ratio) SLBs. Average height mismatches (B) and calculated line tension values for phase-separated SLBs containing either azo-(phyto)sphingolipids with free 3-OH (marked in green), no photolipid (controls with SM, marked in yellow), or THP-protected azo-sphingolipids with the 3-OH blocked (marked in red). Error bars correspond to standard error of the mean (*n* = 5-9 slow-speed AFM images each). Statistical analysis: UV- vs. dark-adapted states (*** p-value < 0.001).

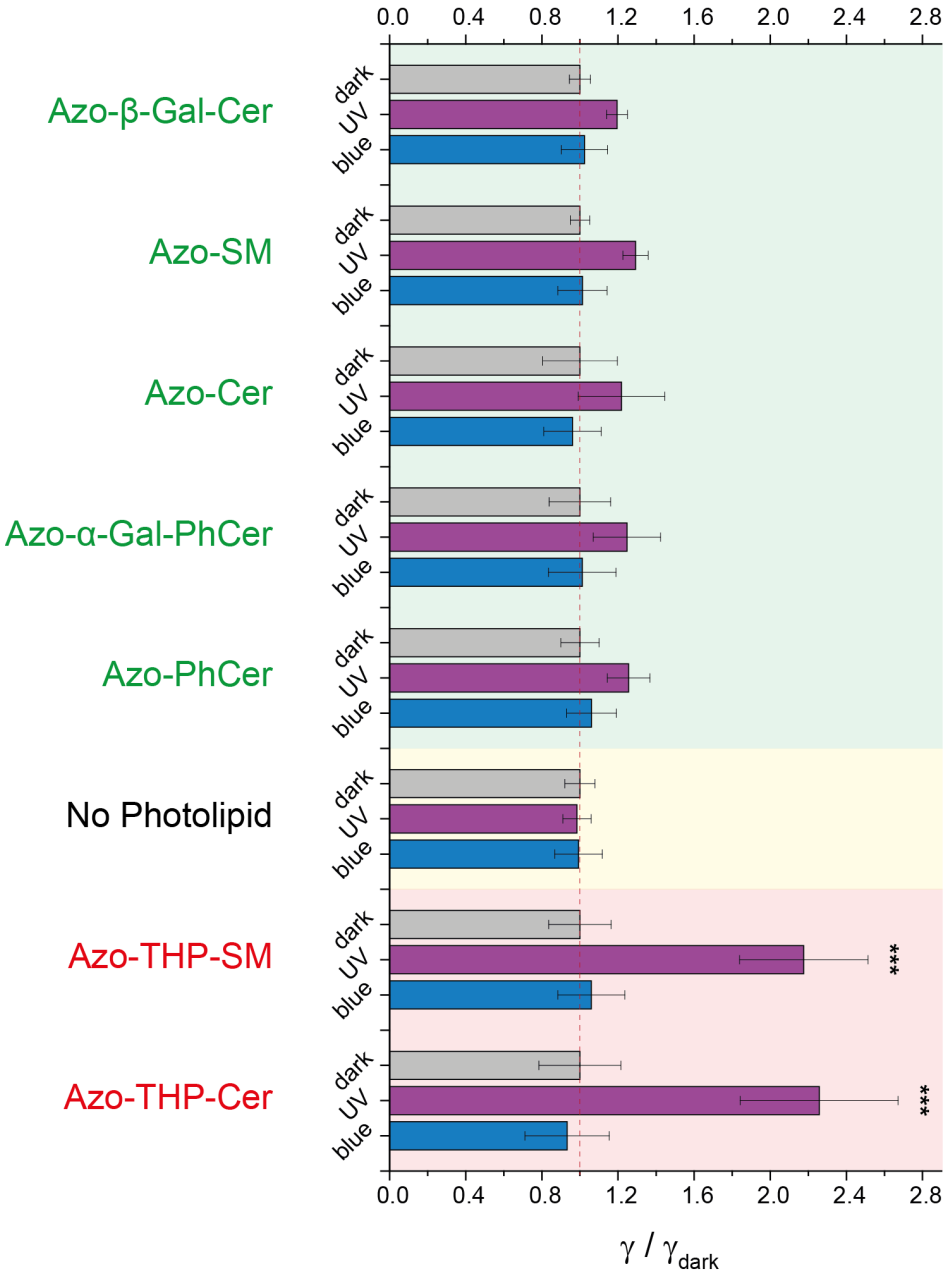

Figure S12 – Normalized changes in the line tension values of L_o domains on phase-separated membranes with different types of azo-sphingolipids, upon application of UV-A (λ = 365 nm) and blue (λ = 470 nm) light. Average line tension values (normalized to dark-adapted state) calculated from height mismatches in Figure S10 for SLBs containing either azo-(phyto)sphingolipids with free 3-OH (marked in green), no photolipid (controls with SM, marked in yellow), or THP-protected azo-sphingolipids with the 3-OH blocked (marked in red). Error bars correspond to the standard error of the mean (*n* = 5-9 slow-speed AFM images each). Statistical analysis: *cis*-photolipids (UV-adapted) vs. control samples without photolipid (*** p-value < 0.001).

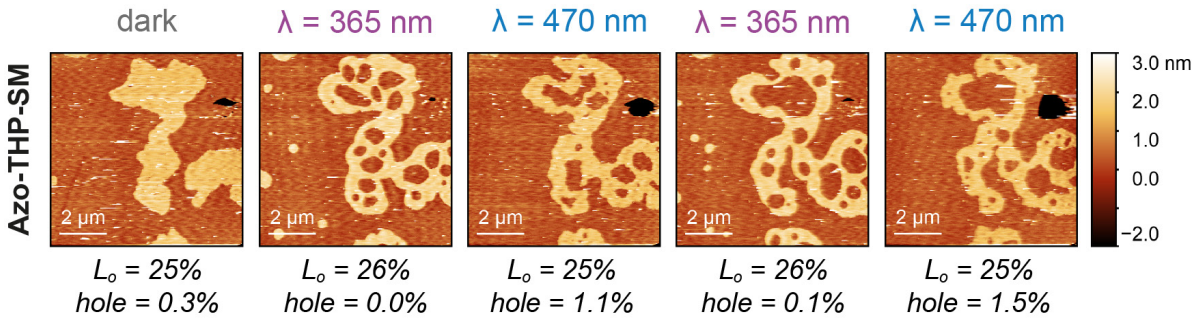

Figure S13 – Membrane expansion/compaction triggered by the photo-isomerization of Azo-THP-SM. Sequential AFM images of DOPC:Chol:SM:Azo-THP-SM (10:6.7:5:5 mol ratio) SLB undergoing phase reshuffling and hole expansion/compaction upon applying UV-A (λ = 365 nm) and blue (λ = 470 nm) lights. Areas of L_o phase and membrane holes are additionally depicted.

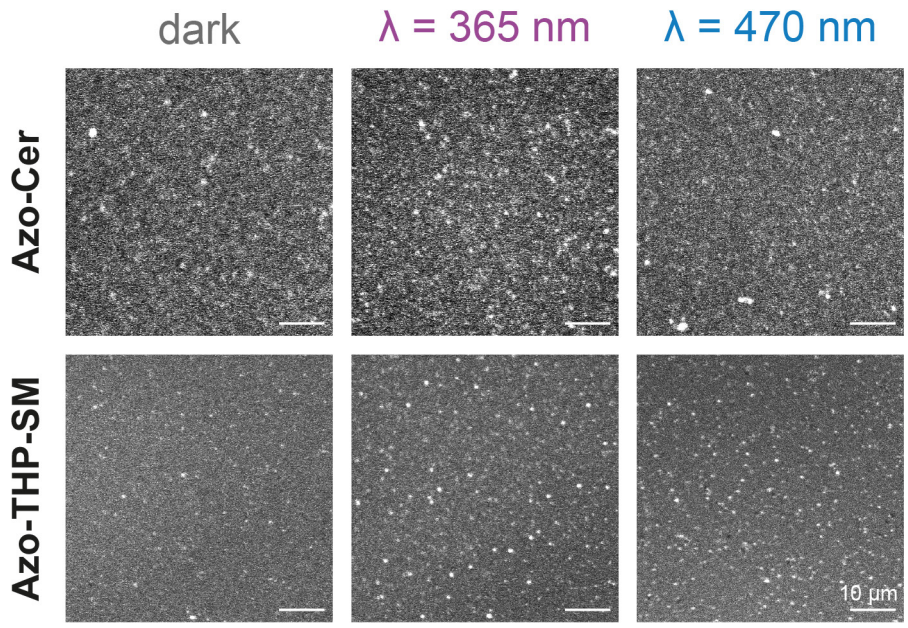

Figure S14 – Homogeneous supported lipid bilayers (SLBs) containing azo-sphingolipids before and after irradiation with UV-A and blue lights. Fluorescence confocal images showing non-phase-separated SLBs composed of DOPC:Chol:Azo-Cer and DOPC:Chol:Azo-THP-SM (both 10:6.7:10 mol ratio), doped with 0.1 mol% Atto655-DOPE, before and 20 min after illumination with UV-A (λ = 365 nm) and blue (λ = 470 nm) lights.

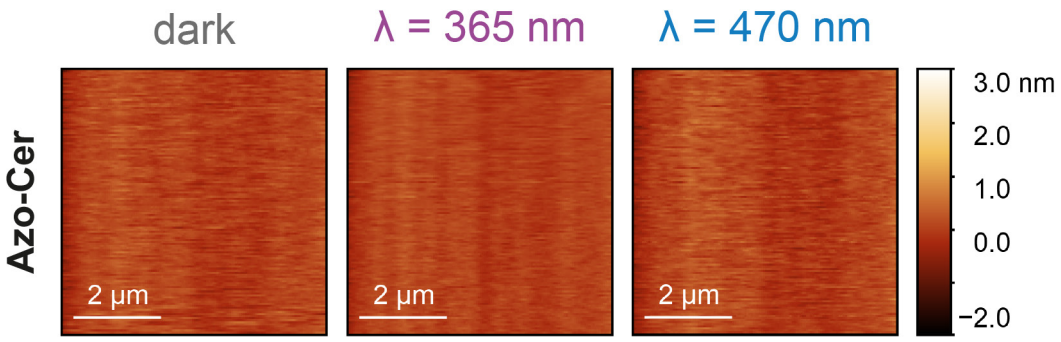

Figure S15 – Homogeneous supported lipid bilayer (SLBs) containing Azo-Cer before and directly after irradiation with UV-A and blue lights. High-speed AFM images showing non-phase-separated SLBs composed of DOPC:Chol:SM:Azo-Cer (10:6.7:10 mol ratio), before and directly after irradiation with UV-A (λ = 365 nm) and blue (λ = 470 nm) lights.

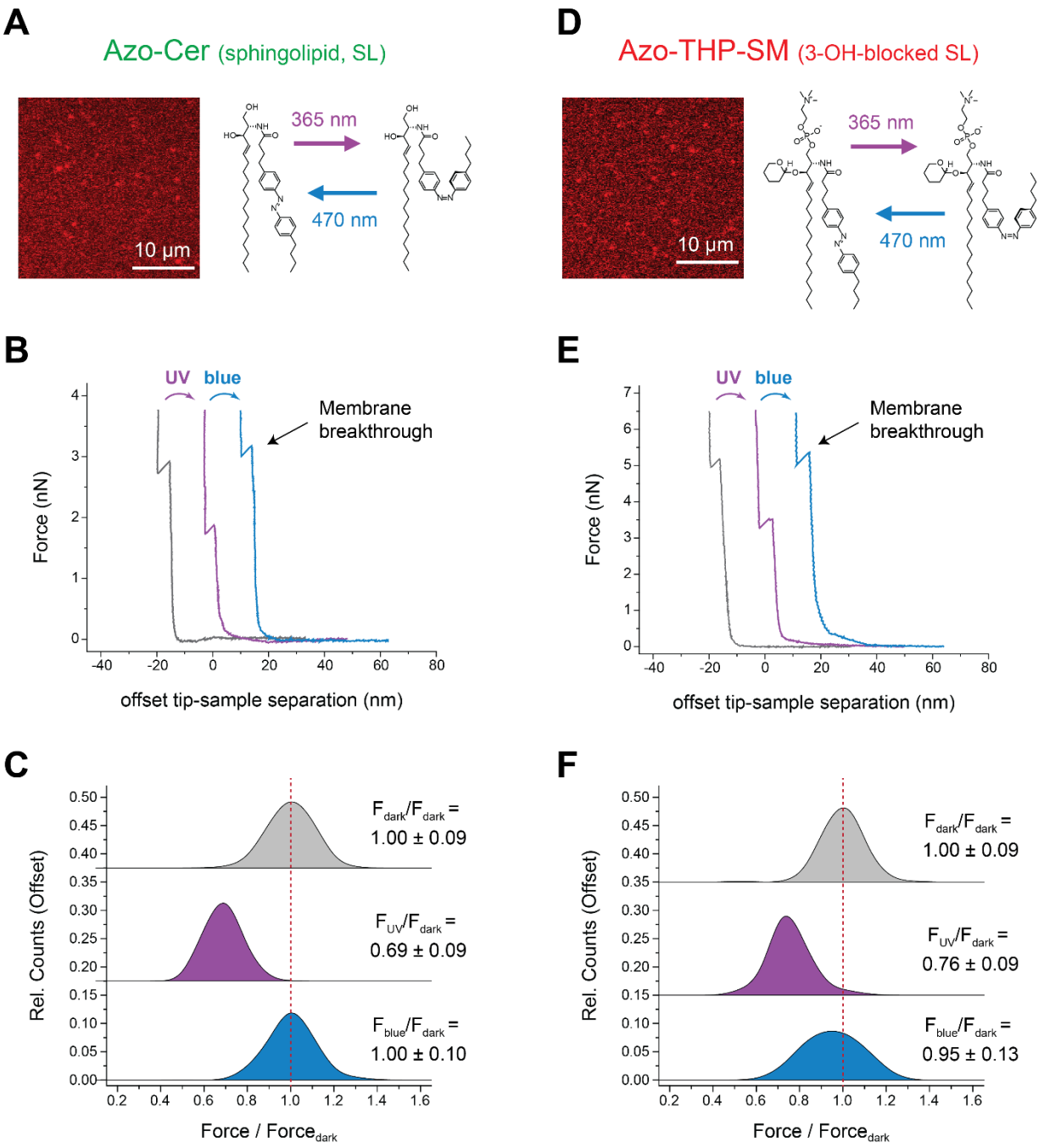

Figure S16 – Breakthrough forces of homogeneous membranes containing non-blocked Azo-Cer (A-C) and 3-OH-blocked Azo-THP-SM (D-F) azo-sphingolipids. (A, D) Confocal images of DOPC:Chol:photolipid (10:6.7:10 mol ratio) supported membranes doped with 0.1 mol% Atto655-DOPE for fluorescence detection. (B, E) Force spectroscopy indentation curves of homogeneous SLBs containing azo-sphingolipids upon illumination with UV-A (λ = 365 nm) and blue (λ = 470 nm) lights. Characteristic membrane breakthrough events for the AFM tip pinching through the SLB marked with arrows. (C, F) Histograms of the overall breakthrough forces (values normalized by the average force obtained at the dark-adapted state, F_{dark}). Error corresponds to the standard deviation of the normalized breakthrough forces. (n = 900 force curves for SLBs with Azo-Cer and n = 200 force curves for SLBs with Azo-THP-SM). For more details, see non-normalized plots in Figure S17.

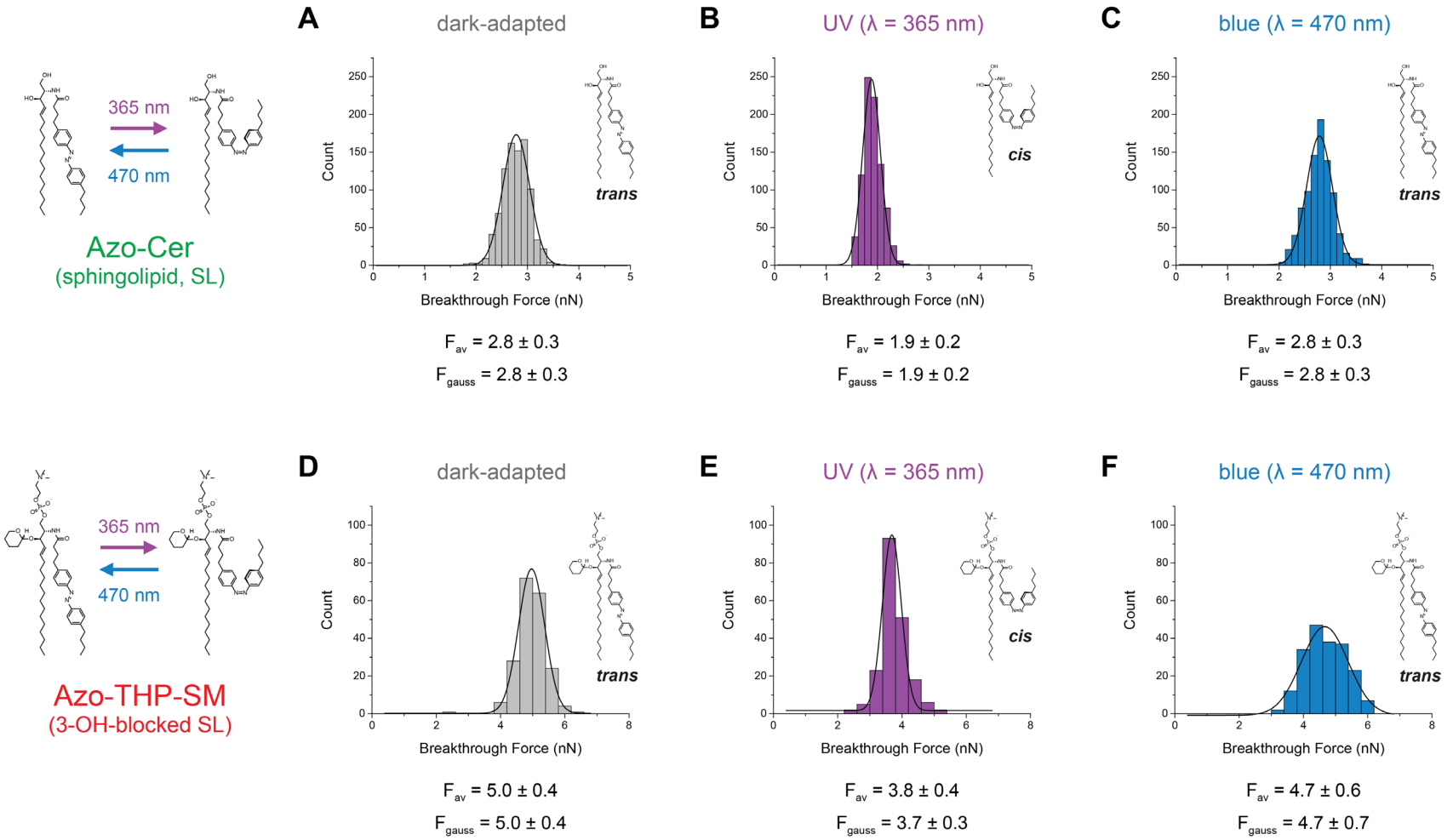

Figure S17 – Non-normalized histograms of breakthrough forces obtained via force spectroscopy on homogeneous SLBs containing non-blocked Azo-Cer (*A-C*) and 3-OH-blocked Azo-THP-SM (*D-F*) azo-sphingolipids. Nominal breakthrough forces recovered from membrane piercing experiments on (A-C) DOPC:Chol:Azo-Cer and (D-F) DOPC:Chol:Azo-THP-SM homogenous membranes (at 10:6.7:10 mol ratio) at the (A, D) dark-, (B, E) UV light- and (C, F) blue light-adapted states. Average breakthrough forces (± standard deviation), as well as Gaussian peak fits (± standard deviation, δ) are displayed (*n* = 900 force curves for SLBs with Azo-Cer and *n* = 200 force curves for SLBs with Azo-THP-SM).

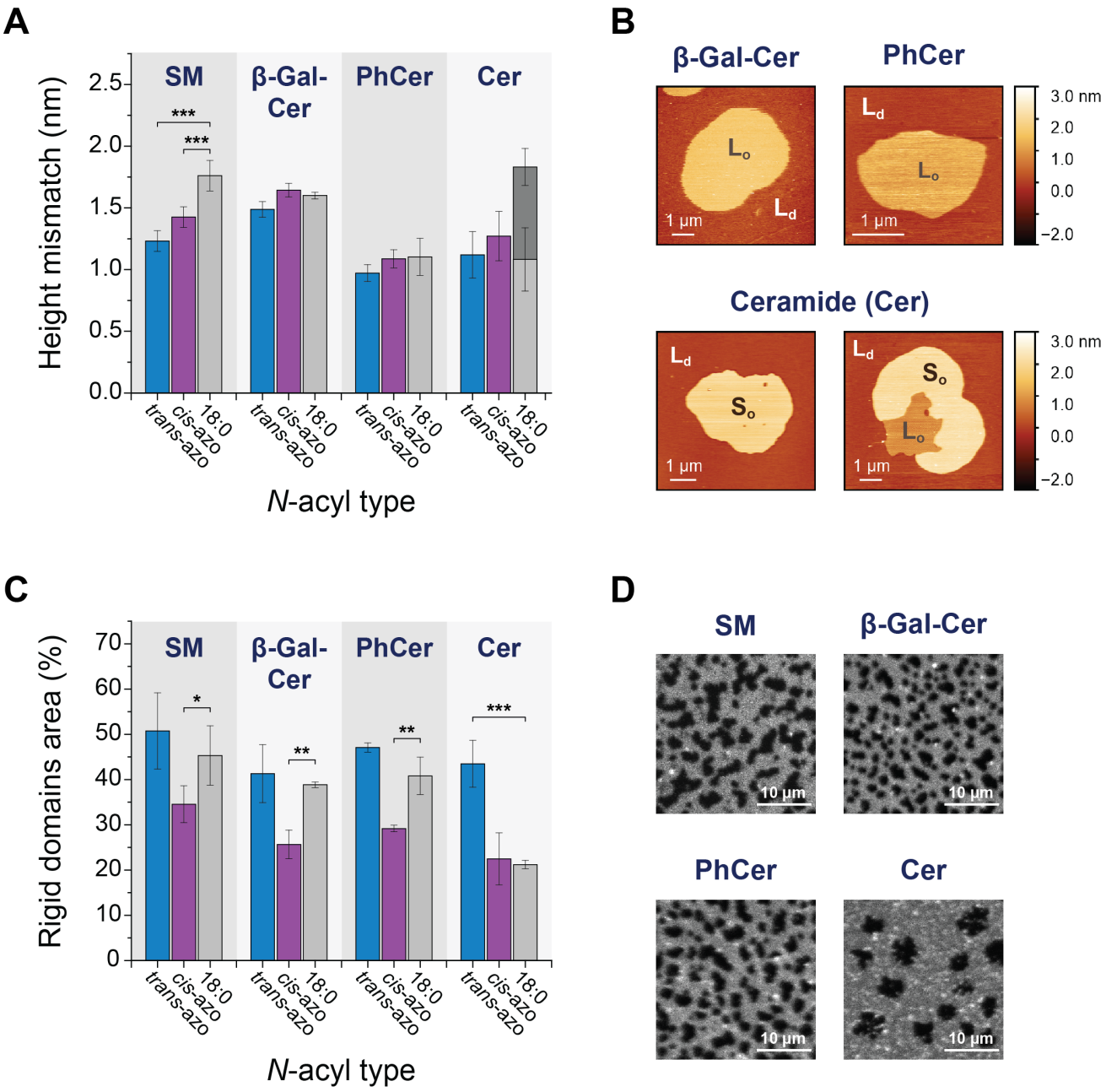

Figure S18 – Comparison of the domain area and height mismatches of phase-separated membranes with photolipids vs. native C18-sphingolipid counterpart. Supported bilayers were made of DOPC:Chol:SM:***X*** (10:6.7:5:5 mol ratio + 0.1 mol% Atto655-DOPE). Comparison of (A) domain height mismatches and (C) total rigid domain areas (i.e., L_o – light grey, or gel – dark grey, for the case of 18:0-Cer) determined for different types of X-sphingolipids (SM, β-GalCer, PhCer, and Cer) as a function of acyl chain (i.e., *trans*-, *cis*-azobenzene vs. 18:0). Illustrative (B) AFM and (D) confocal fluorescence images of SLBs with native non-photoactive C18 lipid counterparts. Statistical analysis: *cis*/*trans*-azobenzene acyl chains vs. 18:0 chains (*** p-value < 0.001, ** p-value < 0.005, * p-value < 0.05).

Supplementary movie legends

Movie S1 – Remodeling of lipid domains by the sphingosine-based Azo-β-GalCer (Fig. 2A) on a phase-separated SLB made of DOPC:Chol:SM:Azo-β-GalCer (10:6.7:5:5 mol ratio), recorded using high-speed AFM. Images correspond to height signal. Initial dark-adapted state is marked with a gray circle. Isomerization to *cis*-Azo-β-GalCer upon irradiation with UV-A light (λ = 365 nm) is marked with a purple circle. Isomerization back to *trans*-Azo-β-GalCer upon irradiation with blue light (λ = 470 nm) is marked with a blue circle. Acquisition = 3.2 s/frame. Video frame rate = 11 fps.

Movie S2 – Remodeling of lipid domains by the sphingosine-based Azo-SM (Fig. 2A) on a phase-separated SLB made of DOPC:Chol:SM:Azo-SM (10:6.7:5:5 mol ratio), recorded using high-speed AFM. Images correspond to height signal. Initial dark-adapted state is marked with a gray circle. Isomerization to *cis*-Azo-SM upon irradiation with UV-A light (λ = 365 nm) is marked with a purple circle. Isomerization back to *trans*-Azo-SM upon irradiation with blue light (λ = 470 nm) is marked with a blue circle. Acquisition = 16.2 s/frame. Video frame rate = 11 fps.

Movie S3 – Remodeling of lipid domains by the sphingosine-based Azo-Cer (Fig. 2A) on a phase-separated SLB made of DOPC:Chol:SM:Azo-Cer (10:6.7:5:5 mol ratio), recorded using high-speed AFM. Images correspond to height signal. Initial dark-adapted state is marked with a gray circle. Isomerization to *cis*-Azo-Cer upon irradiation with UV-A light (λ = 365 nm) is marked with a purple circle. Isomerization back to *trans*-Azo-Cer upon irradiation with blue light (λ = 470 nm) is marked with a blue circle. Acquisition = 5.2 s/frame. Video frame rate = 11 fps.

Movie S4 – Reversible remodeling of lipid domains by Azo-SM (Fig. 2C) on a phase-separated SLB made of DOPC:Chol:SM:Azo-SM (10:6.7:5:5 mol ratio), recorded using high-speed AFM. Images correspond to height signal. Initial dark-adapted state is marked with a gray circle. Isomerization to *cis*-Azo-SM upon irradiation with UV-A light (λ = 365 nm) is marked with a purple circle. Isomerization back to *trans*-Azo-SM upon irradiation with blue light (λ = 470 nm) is marked with a blue circle. Acquisition = 20.2 s/frame. Video frame rate = 11 fps. Quantification of the variation in L_o area is depicted in Fig. 2D.

Movie S5 – Remodeling of lipid domains by the phytosphingosine-based Azo-α-Gal-PhCer (Fig. 2B) on a phase-separated SLB made of DOPC:Chol:SM:Azo-α-Gal-PhCer (10:6.7:5:5 mol ratio), recorded using high-speed AFM. Images correspond to height signal. Initial dark-adapted state is marked with a gray circle. Isomerization to *cis*-Azo-α-Gal-PhCer upon irradiation with UV-A light (λ = 365 nm) is marked with a purple circle. Isomerization back to *trans*-Azo-α-Gal-PhCer upon irradiation with blue light (λ = 470 nm) is marked with a blue circle. Acquisition = 4.2 s/frame. Video frame rate = 11 fps.

Movie S6 – Remodeling of lipid domains by the phytosphingosine-based Azo-PhCer (Fig. 2B) on a phase-separated SLB made of DOPC:Chol:SM:Azo-PhCer (10:6.7:5:5 mol ratio), recorded using high-speed AFM. Images correspond to height signal. Initial dark-adapted state is marked with a gray circle. Isomerization to *cis*-Azo-PhCer upon irradiation with UV-A light (λ = 365 nm) is marked with a purple circle. Isomerization back to *trans*-Azo-PhCer upon irradiation with blue light (λ = 470 nm) is marked with a blue circle. Acquisition = 5.2 s/frame. Video frame rate = 11 fps.

Movie S7 – Remodeling of lipid domains by the 3-OH-blocked sphingosine-based Azo-THP-SM (Fig. 3A) on a phase-separated SLB made of DOPC:Chol:SM:Azo-THP-SM (10:6.7:5:5 mol ratio), recorded using high-speed AFM. Images correspond to phase signal. Initial dark-adapted state is marked with a gray circle. Isomerization to *cis*-Azo-THP-SM upon irradiation with UV-A light (λ = 365 nm) is marked with a purple circle. Isomerization back to *trans*-Azo-THP-SM upon irradiation with blue light (λ = 470 nm) is marked with a blue circle. Acquisition = 4.1 s/frame. Video frame rate = 11 fps.

Movie S8 – Remodeling of lipid domains by the 3-OH-blocked sphingosine-based Azo-THP-Cer (Fig. 3A) on a phase-separated SLB made of DOPC:Chol:SM:Azo-THP-Cer (10:6.7:5:5 mol ratio), recorded using high-speed AFM. Images correspond to height signal. Initial dark-adapted state is marked with a gray circle. Isomerization to *cis*-Azo-THP-Cer upon irradiation with UV-A light (λ = 365 nm) is marked with a purple circle. Isomerization back to *trans*-Azo-THP-Cer upon irradiation with blue light (λ = 470 nm) is marked with a blue circle. Acquisition = 16.2 s/frame. Video frame rate = 11 fps.

Movie S9 – Reversible remodeling of lipid domains by Azo-THP-SM (Fig. 3B) on a phase-separated SLB made of DOPC:Chol:SM:Azo-THP-SM (10:6.7:5:5 mol ratio), recorded using high-speed AFM. Images correspond to height signal. Initial dark-adapted state is marked with a gray circle. Isomerization to *cis*-Azo-THP-SM upon irradiation with UV-A light (λ = 365 nm) is marked with a purple circle. Isomerization back to *trans*-Azo-THP-SM upon irradiation with blue light (λ = 470 nm) is marked with a blue circle. Acquisition = 20.2 s/frame. Video frame rate = 11 fps. Quantification of the variation in L_o area is depicted in Fig. 3C.

Movie S10 – Remodeling of lipid domains by the sphingosine-based Azo-β-GalCer (Fig. S5B) on a phase-separated SLB made of DOPC:Chol:SM:Azo-β-GalCer (10:6.7:5:5 mol ratio), recorded using high-speed AFM. Images correspond to height signal. Initial dark-adapted state is marked with a gray circle. Isomerization to *cis*-Azo-β-GalCer upon irradiation with UV-A light (λ = 365 nm) is marked with a purple circle. Isomerization back to *trans*-Azo-β-GalCer upon irradiation with blue light (λ = 470 nm) is marked with a blue circle. Acquisition = 6.5 s/frame. Video frame rate = 11 fps.

Movie S11 – Remodeling of lipid domains by the sphingosine-based Azo-SM (Fig. S5B) on a phase-separated SLB made of DOPC:Chol:SM:Azo-SM (10:6.7:5:5 mol ratio), recorded using high-speed AFM. Images correspond to height signal. Initial dark-adapted state is marked with a gray circle. Isomerization to *cis*-Azo-SM upon irradiation with UV-A light (λ = 365 nm) is marked with a purple circle. Isomerization back to *trans*-Azo-SM upon irradiation with blue light (λ = 470 nm) is marked with a blue circle. Acquisition = 3.2 s/frame. Video frame rate = 11 fps.

Movie S12 – Remodeling of lipid domains by the sphingosine-based Azo-Cer (Fig. S5B) on a phase-separated SLB made of DOPC:Chol:SM:Azo-Cer (10:6.7:5:5 mol ratio), recorded using high-speed AFM. Images correspond to height signal. Initial dark-adapted state is marked with a gray circle. Isomerization to *cis*-Azo-Cer upon irradiation with UV-A light (λ = 365 nm) is marked with a purple circle. Isomerization back to *trans*-Azo-Cer upon irradiation with blue light (λ = 470 nm) is marked with a blue circle. Acquisition = 2.5 s/frame. Video frame rate = 11 fps.

Movie S13 – Remodeling of lipid domains by the phytosphingosine-based Azo-α-Gal-PhCer (Fig. S5C) on a phase-separated SLB made of DOPC:Chol:SM:Azo-α-Gal-PhCer (10:6.7:5:5 mol ratio), recorded using high-speed AFM. Images correspond to height signal. Initial dark-adapted state is marked with a gray circle. Isomerization to *cis*-Azo-α-Gal-PhCer upon irradiation with UV-A light (λ = 365 nm) is marked with a purple circle. Isomerization back to *trans*-Azo-α-Gal-PhCer upon irradiation with blue light (λ = 470 nm) is marked with a blue circle. Acquisition = 5.2 s/frame. Video frame rate = 11 fps.

Movie S14 – Remodeling of lipid domains by the phytosphingosine-based Azo-α-Gal-PhCer on a phase-separated SLB made of DOPC:Chol:SM:Azo-α-Gal-PhCer (10:6.7:5:5 mol ratio), recorded using high-speed AFM. Images correspond to height signal. Initial dark-adapted state is marked with a gray circle. Isomerization to *cis*-Azo-α-Gal-PhCer upon irradiation with UV-A light (λ = 365 nm) is marked with a purple circle. Isomerization back to *trans*-Azo-α-Gal-PhCer upon irradiation with blue light (λ = 470 nm) is marked with a blue circle. Acquisition = 5.2 s/frame. Video frame rate = 11 fps.

Movie S15 – Remodeling of lipid domains by the phytosphingosine-based Azo-PhCer (Fig. S5C) on a phase-separated SLB made of DOPC:Chol:SM:Azo-PhCer (10:6.7:5:5 mol ratio), recorded using high-speed AFM. Images correspond to height signal. Initial dark-adapted state is marked with a gray circle. Isomerization to *cis*-Azo-PhCer upon irradiation with UV-A light (λ = 365 nm) is marked with a purple circle. Isomerization back to *trans*-Azo-PhCer upon irradiation with blue light (λ = 470 nm) is marked with a blue circle. Acquisition = 5.2 s/frame. Video frame rate = 5.2 fps.

Movie S16 – Remodeling of lipid domains by the 3-OH-blocked sphingosine-based Azo-THP-SM (Fig. S5D) on a phase-separated SLB made of DOPC:Chol:SM:Azo-THP-SM (10:6.7:5:5 mol ratio), recorded using high-speed AFM. Images correspond to height signal. Initial dark-adapted state is marked with a gray circle. Isomerization to *cis*-Azo-THP-SM upon irradiation with UV-A light (λ = 365 nm) is marked with a purple circle. Isomerization back to *trans*-Azo-THP-SM upon irradiation with blue light (λ = 470 nm) is marked with a blue circle. Acquisition = 10.1 s/frame. Video frame rate = 11 fps.

Movie S17 – Remodeling of lipid domains by the 3-OH-blocked sphingosine-based Azo-THP-Cer (Fig. S5D) on a phase-separated SLB made of DOPC:Chol:SM:Azo-THP-Cer (10:6.7:5:5 mol ratio), recorded using high-speed AFM. Images correspond to height signal. Initial dark-adapted state is marked with a gray circle. Isomerization to *cis*-Azo-THP-Cer upon irradiation with UV-A light (λ = 365 nm) is marked with a purple circle. Isomerization back to *trans*-Azo-THP-Cer upon irradiation with blue light (λ = 470 nm) is marked with a blue circle. Acquisition = 8.1 s/frame. Video frame rate = 11 fps.

Statistical analysis

Tables S1 – Data information for Figures S9 and S10. Total L_o area recorded via fluorescence confocal microscopy, as well as L_d-L_o height mismatch and line tension values recorded via AFM for DOPC:Chol:SM:*azolipid* (10:6.7:5:5, mol ratio) SLBs.

Total L_o area data (Figure S9)

	L_o area (%)	St.dev.	*n*
no photolipid (dark)	45.31	6.57	5
no photolipid (UV)	45.24	6.49	5
no photolipid (blue)	45.37	6.57	5
azo-β-Gal-Cer (dark)	40.10	6.34	5
azo-β-Gal-Cer (UV)	25.67	3.16	5
azo-β-Gal-Cer (blue)	42.50	6.46	5
azo-SM (dark)	49.61	8.17	5
azo-SM (UV)	34.55	4.09	5
azo-SM (blue)	51.91	8.67	5
azo-Cer (dark)	44.60	5.17	5
azo-Cer (UV)	22.47	5.74	5
azo-Cer (blue)	42.36	5.19	5
azo-α-Gal-PhCer (dark)	43.10	3.72	5
azo-α-Gal-PhCer (UV)	21.82	3.05	5
azo-α-Gal-PhCer (blue)	43.11	4.70	5
azo-PhCer (dark)	48.23	0.82	5
azo-PhCer (UV)	29.17	0.74	5
azo-PhCer (blue)	45.92	1.21	5
azo-THP-SM (dark)	26.47	4.22	5
azo-THP-SM (UV)	30.02	0.81	5
azo-THP-SM (blue)	29.14	1.97	5
azo-THP-Cer (dark)	31.17	4.01	8
azo-THP-Cer (UV)	37.44	5.05	8
azo-THP-Cer (blue)	32.67	3.92	8

L_d-L_o area height mismatch data (Figure S10 B)

	H_{diff} (nm)	St.dev.	*n*
no photolipid (dark)	1.769	0.135	5
no photolipid (UV)	1.753	0.120	5
no photolipid (blue)	1.761	0.116	5
azo-β-Gal-Cer (dark)	1.477	0.077	5
azo-β-Gal-Cer (UV)	1.644	0.055	5
azo-β-Gal-Cer (blue)	1.498	0.050	5
azo-SM (dark)	1.227	0.076	9
azo-SM (UV)	1.426	0.084	7
azo-SM (blue)	1.236	0.092	6
azo-Cer (dark)	1.130	0.218	6
azo-Cer (UV)	1.272	0.200	5
azo-Cer (blue)	1.110	0.158	6
azo-α-Gal-PhCer (dark)	1.524	0.237	5
azo-α-Gal-PhCer (UV)	1.746	0.204	5
azo-α-Gal-PhCer (blue)	1.533	0.275	5
azo-PhCer (dark)	0.955	0.085	5
azo-PhCer (UV)	1.088	0.073	5
azo-PhCer (blue)	0.989	0.052	5
azo-THP-SM (dark)	0.732	0.157	10
azo-THP-SM (UV)	1.134	0.233	10
azo-THP-SM (blue)	0.754	0.170	10
azo-THP-Cer (dark)	0.700	0.236	13
azo-THP-Cer (UV)	1.138	0.199	9
azo-THP-Cer (blue)	0.656	0.290	12

Line tension data (Figure S10 C)

	γ (pN)	St.dev.	*n*
no photolipid (dark)	5.478	0.683	5
no photolipid (UV)	5.395	0.603	5
no photolipid (blue)	5.437	0.583	5
azo-β-Gal-Cer (dark)	4.060	0.355	5
azo-β-Gal-Cer (UV)	4.850	0.268	5
azo-β-Gal-Cer (blue)	4.157	0.232	5
azo-SM (dark)	2.961	0.318	9
azo-SM (UV)	3.826	0.375	7
azo-SM (blue)	3.000	0.384	6
azo-Cer (dark)	2.605	0.886	6
azo-Cer (UV)	3.174	0.882	5
azo-Cer (blue)	2.504	0.649	6
azo-α-Gal-PhCer (dark)	4.310	1.101	5
azo-α-Gal-PhCer (UV)	5.375	1.019	5
azo-α-Gal-PhCer (blue)	4.363	1.286	5
azo-PhCer (dark)	1.912	0.304	5
azo-PhCer (UV)	2.401	0.287	5
azo-PhCer (blue)	2.029	0.191	5
azo-THP-SM (dark)	1.211	0.444	10
azo-THP-SM (UV)	2.635	0.854	10
azo-THP-SM (blue)	1.284	0.484	10
azo-THP-Cer (dark)	1.165	0.640	13
azo-THP-Cer (UV)	2.631	0.812	9
azo-THP-Cer (blue)	1.087	0.778	12

Tables S2 – Data information for Figures S6 and S18.

Upper tables: Total L_o area recorded via high-speed AFM for DOPC:Chol:SM:*azolipid* (10:6.7:5:5, mol ratio) SLBs, ungrouped or grouped by photolipid type.

Lower tables: Total L_o area recorded via fluorescence confocal microscopy, as well as L_d-L_o height mismatch recorded via AFM for DOPC:Chol:SM:*azolipid* vs. DOPC:Chol:SM:*C18-lipid* (10:6.7:5:5, mol ratio) SLBs.

Analysis of high-speed AFM snapshots

Ungrouped L_o area (Figure S6C)

	L_o / L_o (dark)	St.dev.	*n*
no photolipid (UV)	0.974	0.035	2
no photolipid (blue)	0.965	0.045	2
azo-β-Gal-Cer (UV)	0.775	0.006	2
azo-β-Gal-Cer (blue)	1.035	0.126	2
azo-SM (UV)	0.773	0.053	3
azo-SM (blue)	1.020	0.164	3
azo-Cer (UV)	0.636	0.105	2
azo-Cer (blue)	1.028	0.077	2
azo-α-Gal-PhCer (UV)	0.796	0.119	3
azo-α-Gal-PhCer (blue)	0.997	0.080	3
azo-PhCer (UV)	0.788	0.101	2
azo-PhCer (blue)	1.009	0.074	2
azo-THP-SM (UV)	1.235	0.154	3
azo-THP-SM (blue)	0.966	0.034	3
azo-THP-Cer (UV)	1.270	0.095	2
azo-THP-Cer (blue)	0.990	0.006	2

Grouped L_o area (Figure S6A)

	L_o area (%)	St.dev.	*n*
azo-SL (dark)	26.59	9.02	7
azo-SL (UV)	19.83	7.00	7
azo-SL (blue)	26.89	8.46	7
azo-PhSL (dark)	29.23	8.82	5
azo-PhSL (UV)	22.90	9.73	5
azo-PhSL (blue)	30.18	9.66	5
azo-THP-SL (dark)	19.65	5.96	5
azo-THP-SL (UV)	24.09	5.62	5
azo-THP-SL (blue)	19.29	6.32	5

Comparison photolipids vs. native C18-lipid counterparts

L_d-L_o height mismatches (Figure S18A)

	H_{diff} (nm)	St.dev.	*n*
trans-azo-SM	1.231	0.084	15
cis-azo-SM	1.426	0.084	7
18:0-SM	1.761	0.123	15
trans-azo-β-GalCer	1.488	0.063	10
cis-azo-β-GalCer	1.644	0.055	5
18:0-β-GalCer	1.600	0.027	5
trans-azo-Phcer	0.972	0.068	10
cis-azo-Phcer	1.088	0.073	5
18:0-Phcer	1.103	0.151	6
trans-azo-Cer	1.120	0.188	12
cis-azo-Cer	1.272	0.200	5
18:0-Cer (Ld-Lo)	1.082	0.256	4
18:0-Cer (Ld-Gel)	1.832	0.149	10

Total L_o area (Figure S18C)

	L_o area (%)	St.dev.	*n*
trans-azo-SM	50.76	8.42	10
cis-azo-SM	34.55	4.09	5
18:0-SM	45.31	6.57	5
trans-azo-β-GalCer	41.30	6.40	10
cis-azo-β-GalCer	25.67	3.16	5
18:0-β-GalCer	38.85	0.63	3
trans-azo-Phcer	47.08	1.02	10
cis-azo-Phcer	29.17	0.74	5
18:0-Phcer	40.82	4.13	6
trans-azo-Cer	43.48	5.18	10
cis-azo-Cer	22.47	5.74	5
18:0-Cer	21.20	0.93	6

Tables S3 – Results one-way ANOVA statistical analysis (Bonferroni t-tests). Evaluation of the total relative L_o area (normalized to dark-adapted state) for DOPC:Chol:SM:*azolipid* (10:6.7:5:5, mol ratio) SLBs with *cis*-photolipid vs. control membranes without photolipid (DOPC:Chol:SM; 10:6.7:10, mol ratio). Fluorescence confocal microscopy data shown in Figure 4C.

	difference of mean	t-statistics	p-value	significance
no photolipid vs. azo-Cer	0.496	5.412	<0.001	***
no photolipid vs. azo-α-Gal-PhCer	0.494	5.384	<0.001	***
no photolipid vs. azo-PhCer	0.395	4.309	<0.001	***
no photolipid vs. azo-β-Gal-Cer	0.360	3.923	0.003	**
no photolipid vs. azo-SM	0.304	3.312	0.027	*
no photolipid vs. azo-THP-Cer	0.201	2.590	0.23	
no photolipid vs. azo-THP-SM	0.134	1.466	1	

	difference of mean	t-statistics	p-value	significance
azo-β-Gal-Cer vs. azo-THP-Cer	0.561	5.542	<0.001	***
azo-β-Gal-Cer vs. azo-THP-SM	0.494	4.400	<0.001	***
azo-β-Gal-Cer vs. no photolipid	0.360	3.923	0.003	**
azo-β-Gal-Cer vs. azo-Cer	0.137	1.216	1	
azo-β-Gal-Cer vs. azo-α-Gal-PhCer	0.134	1.193	1	
azo-β-Gal-Cer vs. azo-SM	0.056	0.499	1	
azo-β-Gal-Cer vs. azo-PhCer	0.035	0.315	1	

	difference of mean	t-statistics	p-value	significance
azo-SM vs. azo-THP-Cer	0.505	4.988	<0.001	***
azo-SM vs. azo-THP-SM	0.438	3.901	0.004	***
azo-SM vs. no photolipid	0.304	3.312	0.027	*
azo-SM vs. azo-Cer	0.193	1.715	1	
azo-SM vs. azo-α-Gal-PhCer	0.190	1.692	1	
azo-SM vs. azo-PhCer	0.092	0.815	1	
azo-SM vs. azo-β-Gal-Cer	0.056	0.499	1	

	difference of mean	t-statistics	p-value	significance
azo-Cer vs. azo-THP-Cer	0.697	6.891	<0.001	***
azo-Cer vs. azo-THP-SM	0.631	5.616	<0.001	***
azo-Cer vs. no photolipid	0.496	5.412	<0.001	***
azo-Cer vs. azo-SM	0.193	1.715	1	
azo-Cer vs. azo-β-Gal-Cer	0.137	1.216	1	
azo-Cer vs. azo-PhCer	0.101	0.900	1	
azo-Cer vs. azo-α-Gal-PhCer	0.003	0.023	1	

	difference of mean	t-statistics	p-value	significance
azo-α-Gal-PhCer vs. azo-THP-Cer	0.695	6.866	<0.001	***
azo-α-Gal-PhCer vs. azo-THP-SM	0.628	5.593	<0.001	***
azo-α-Gal-PhCer vs. no photolipid	0.494	5.384	<0.001	***
azo-α-Gal-PhCer vs. azo-SM	0.190	1.692	1	
azo-α-Gal-PhCer vs. azo-β-Gal-Cer	0.134	1.193	1	
azo-α-Gal-PhCer vs. azo-PhCer	0.099	0.877	1	
azo-α-Gal-PhCer vs. azo-Cer	0.003	0.023	1	

	difference of mean	t-statistics	p-value	significance
azo-PhCer vs. azo-THP-Cer	0.596	5.892	<0.001	***
azo-PhCer vs. azo-THP-SM	0.529	4.715	<0.001	***
azo-PhCer vs. no photolipid	0.395	4.309	<0.001	***
azo-PhCer vs. azo-Cer	0.101	0.900	1	
azo-PhCer vs. azo-α-Gal-PhCer	0.099	0.877	1	
azo-PhCer vs. azo-SM	0.092	0.815	1	
azo-PhCer vs. azo-β-Gal-Cer	0.035	0.315	1	

	difference of mean	t-statistics	p-value	significance
azo-THP-SM vs. azo-Cer	0.631	5.616	<0.001	***
azo-THP-SM vs. azo-α-Gal-PhCer	0.628	5.593	<0.001	***
azo-THP-SM vs. azo-PhCer	0.529	4.715	<0.001	***
azo-THP-SM vs. azo-β-Gal-Cer	0.494	4.400	<0.001	***
azo-THP-SM vs. azo-SM	0.438	3.901	0.004	**
azo-THP-SM vs. no photolipid	0.134	1.466	1	
azo-THP-SM vs. azo-THP-Cer	0.067	0.661	1	

	difference of mean	t-statistics	p-value	significance
azo-THP-Cer vs. azo-Cer	0.697	6.891	<0.001	***
azo-THP-Cer vs. azo-α-Gal-PhCer	0.695	6.866	<0.001	***
azo-THP-Cer vs. azo-PhCer	0.596	5.892	<0.001	***
azo-THP-Cer vs. azo-β-Gal-Cer	0.561	5.542	<0.001	***
azo-THP-Cer vs. azo-SM	0.505	4.988	<0.001	***
azo-THP-Cer vs. no photolipid	0.201	2.590	0.23	
azo-THP-Cer vs. azo-THP-SM	0.067	0.661	1	

Compound synthesis and characterization

Methods and equipment

Unless otherwise noted, all reactions were magnetically stirred and performed under an atmosphere of inert gas (Ar or N_2) using standard Schlenk techniques. The reactions were carried out in oven-dried glassware (200 °C oven temperature). External bath temperatures were used to record all reaction mixture temperatures. Diethyl ether (Et_2O) and tetrahydrofuran (THF) were distilled prior to use under an atmosphere of N_2 from sodium and benzophenone, triethylamine (NEt_3) from calcium hydride. *N*,*N*-dimethylformamide (DMF), toluene and methanol (MeOH) were purchased from Acros Organics as 'extra dry' reagents under inert gas atmosphere and over molecular sieves. Solvents for flash column chromatography and crystallization experiments were purchased in technical grade and distilled under reduced pressure prior to use. Degassed solvents were degassed under N_2 atmosphere by using either three successive freeze-pump-thaw cycles or by purging the solvent for 30 min with N_2. Petroleum ether (PE) refers to fractions of *iso*-hexanes which boil between 40 and 80 °C. All other reagents were purchased from commercial sources and used without further purification.

Chromatography. Analytical thin-layer chromatography (TLC) was performed on pre-coated glass plates (silica gel 60 F254) from Merck, and visualized by exposure to ultraviolet light (UV, 254 nm) and by staining with aqueous acidic ceric ammonium molybdate(IV) (CAM) solution. Flash column chromatography was performed using Merck silica gel (40–63 µm particle size).

NMR Spectroscopy. Proton nuclear magnetic resonance (^{1}H NMR) spectra were recorded in 5 mm tubes on a Varian 300, Varian 400, Inova 400 or Varian 600 spectrometer in deuterated solvents at room temperature. Chemical shifts (δ scale) are expressed in parts per million (ppm) and are calibrated using residual protic solvent as an internal reference ($CHCl_3$: δ = 7.26 ppm). Data for ^{1}H NMR spectra are reported as follows: chemical shift (δ ppm) (multiplicity, coupling constants (Hz), integration). Couplings are expressed as: s = singlet, d = doublet, t = triplet, q = quartet, m = multiplet or combinations thereof. Carbon nuclear magnetic resonance (^{13}C NMR) spectra were recorded at 75, 100 and 150 MHz, respectively. Carbon chemical shifts (δ scale) are also expressed in parts per million (ppm) and are referenced to the central carbon resonances of the solvents ($CDCl_3$: δ = 77.16 ppm). In order to assign the ^{1}H and ^{13}C NMR spectra, a range of 2D NMR experiments (COSY, HSQC, HMBC, NOESY) were used as appropriate. The numbering of the proton and carbon atoms does not correspond to the IUPAC nomenclature. Diastereotopic protons in the ^{1}H NMR spectra are referenced with a and b, nomenclature is arbitrarily and does not correspond to the spin system.

High performance liquid chromatography (HPLC). HPLC was performed with HPLC grade solvents and deionized H_2O that was purified on a TKA MicroPure H_2O purification system. All solvents were degassed with helium gas prior to use. Unless noticed otherwise, all experiments were carried out at room temperature.

Analytical HPLC spectra were recorded on a ultra-high performance liquid chromatography (UHPLC) system from the Agilent 1260 Infinity series (1260 degasser, 1260 Binary Pump VL, 1260 ALS auto sampler, 1260 TCC thermostated column compartment, 1260 DAD diode array detector), which was computer-controlled through Agilent ChemStation software.

Chiral HPLC spectra were recorded on a high performance liquid chromatography (HPLC) system from the Shimadzu 20A series (DGU-20A3R degasser, LC-20AD Binary Pump VL, SIL-20AHT autosampler, CTO-20A thermostated column compartment, SPD-M20A DAD diode array detector), which was computer controlled through Shimadzu LabSolutions Software (Version 5.42 SP5). Enantiomeric excess (*ee*) was calculated by using the following equation; m_1 refers to the integral of the major peak and m_2 to the integral of the minor peak:

$$ee = \frac{|-m_1 - m_2|}{m_1 + m_2} \cdot 100\%$$

High-resolution mass spectrometry (HRMS). A Varian MAT CH7A mass spectrometer was used to obtain high-resolution electron ionization (EI) mass. High-resolution electronspray (ESI) mass spectra were recorded on a Varian MAT 711 MS spectrometer operation in either positive or negative ionization modes.

Infrared spectroscopy (IR). Infrared spectra (IR) were recorded on a Perkin Elmer Spectrum BX II (FTIR System) equipped with an attenuated total reflection (ATR) measuring unit. IR data is reported in frequency of absorption (cm^{-1}). The IR bands are characterized as: w = weak, m = medium, s = strong, br = broad, or combinations thereof.

Melting points (mp). Melting points were measured on a Büchi Melting Point B-540 or SRS MPA120 EZ-Melt apparatus and are uncorrected.

Optical rotation. Perkin-Elmer 241 or Krüss P8000-T polarimeter were used to measure optical rotation at the Sodium D-line (589 nm) at the given temperature (*T* in °C) and concentrations (*c* in g/100 mL) using spectroscopic grade solvents. The measurements were carried out in a cell with a path length (*d*) of 0.5 dm. Specific rotations were calculated using the following equation:

$$[\alpha]_D = \frac{\alpha}{c \cdot d} \frac{10^{-1} \cdot \mathrm{deg} \cdot \mathrm{cm}^2}{\mathrm{g}}$$

Synthesis overview

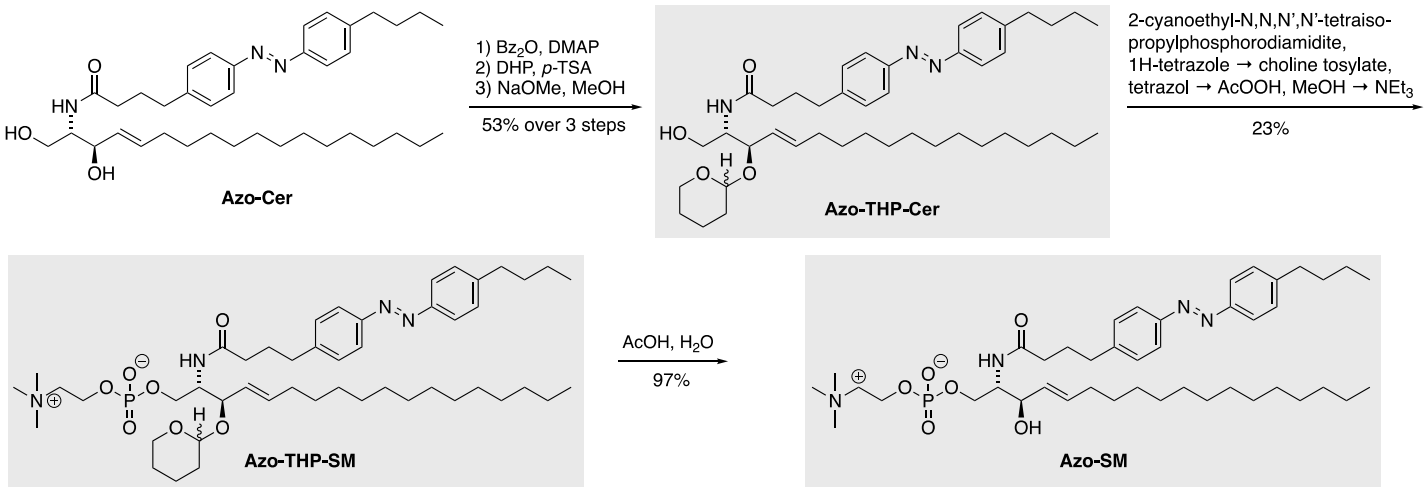

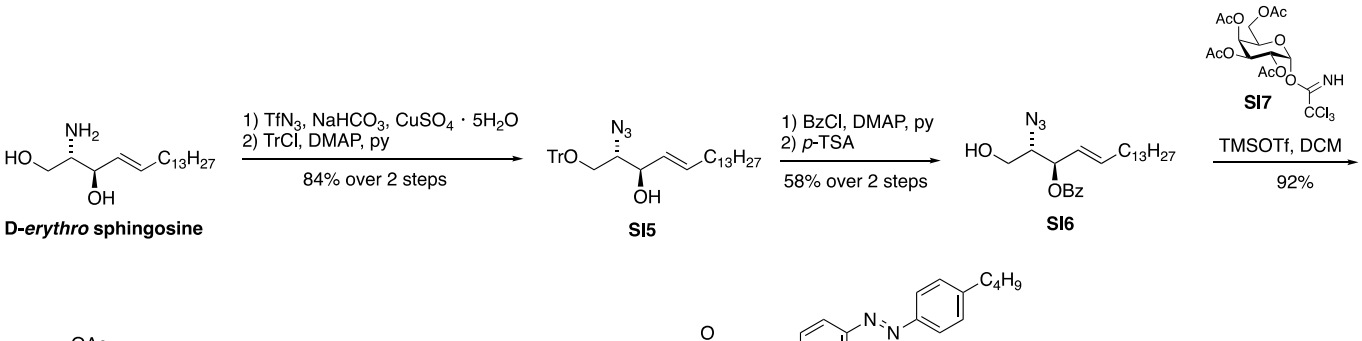

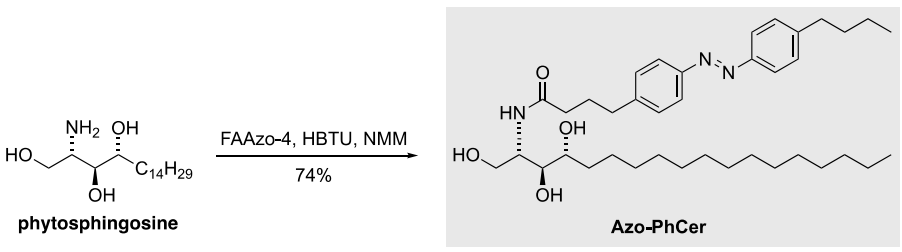

Experimental procedures

(2*S*,3*R*,*E*)-2-(4-(4-((*E*)-(4-Butylphenyl)diazenyl)phenyl)butanamido)-3-hydroxyoctadec-4-en-1-yl benzoate (SI1)

To a solution of **Azo-Cer** (previously named ACe-1[R1]) (100 mg, 0.165 mmol, 1.0 eq.) in dry DCM (10 mL) were added benzoic anhydride (41.2 mg, 0.182 mmol, 1.11 eq.) and DMAP (2.02 mg, 16.5 µmol, 0.10 eq.) and the reaction was stirred for 24 h at room temperature. Then, $NaHCO_3$ solution (100 mL) was added and the organic layer was extracted with EtOAc (3 × 100 mL) and dried (Na_2SO_4). Purification *via* flash column chromatography [PE/EtOAc, 9:1 to 1:2] afforded benzoyl-protected ceramide **SI1** (81.7 mg, 0.115 mmol, 70%) as a light orange solid.

R_f = 0.69 [PE: EtOAc 1:1]

^{1}H NMR (400 MHz, $CDCl_3$): δ = 8.04–7.97 (m, 2H), 7.84–7.76 (m, 4H), 7.59 – 7.53 (m, 1H), 7.42 (t, *J* = 7.7 Hz, 2H), 7.35–7.28 (m, 2H), 7.25 (d, *J* = 8.1 Hz, 2H), 5.93 (d, *J* = 7.9 Hz, 1H), 5.77 (dtd, *J* = 14.9, 6.7, 1.2 Hz, 1H), 5.53 (ddt, *J* = 15.4, 6.6, 1.5 Hz, 1H), 4.62–4.53 (m, 1H), 4.47–4.37 (m, 2H), 4.26 (dd, *J* = 6.7, 4.0 Hz, 1H), 2.69 (t, *J* = 7.9 Hz, 4H), 2.22 (t, *J* = 7.4 Hz, 2H), 2.00 (m, 4H), 1.70–1.59 (m, 2H), 1.45–1.15 (m, 24H), 0.94 (t, *J* = 7.3 Hz, 3H), 0.87 (t, *J* = 6.8 Hz, 3H) ppm.

^{13}C NMR (101 MHz, $CDCl_3$): δ = 173.2, 167.1, 151.4, 151.1, 146.5, 144.6, 135.0, 133.5, 129.9, 129.3, 129.2, 128.7, 128.2, 123.0, 122.9, 73.5, 63.4, 53.5, 36.0, 35.74, 35.1, 33.6, 32.4, 32.1, 29.8, 29.8, 29.8, 29.6, 29.5, 29.4, 29.2, 27.0, 22.9, 22.5, 14.3, 14.1 ppm.

IR (ATR): $\tilde{\nu}$ = 2925 (s), 2853 (m), 2358 (w), 2340 (w), 1722 (m), 1648 (m), 1602 (w), 1498 (w), 1452 (w), 1388 (w), 1273 (s), 965 (w), 844 (w), 712 (m) cm^{-1}.

HRMS (ESI): calcd. for $C_{45}H_{64}N_3O_4^+$: 710.4891 $[M+H]^+$
found: 710.4887 $[M+H]^+$.

(2*S*,3*R*,*E*)-2-(4-(4-((*E*)-(4-Butylphenyl)diazenyl)phenyl)butanamido)-3-((tetrahydro-2H-pyran-2-yl)oxy)octadec-4-en-1-yl benzoate (SI2)

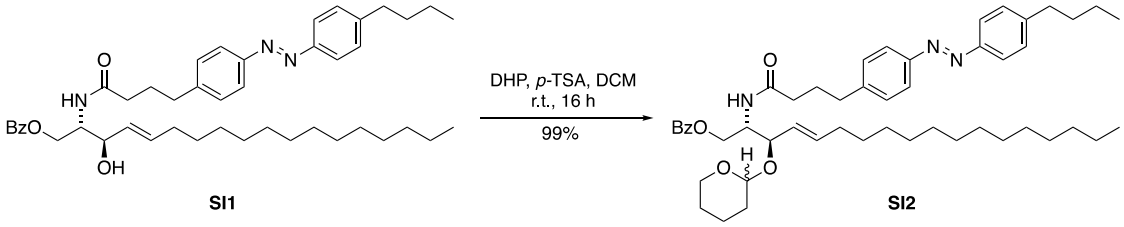

To a solution of secondary alcohol **SI1** (75.4 mg, 0.106 mmol, 1.0 eq.) in dry DCM (5 mL) were added freshly distilled dihydropyran (42.9 mL, 0.475 mmol, 4.5 eq.) and *p*-TSA monohydrate (1.63 mg, 9.49 µmol, 0.09 eq.) and the reaction mixture was stirred for 16 h at room temperature. Then, $NaHCO_3$ solution (10 mL) was added and the aqueous layer was extracted with EtOAc (3 × 20 mL) and dried (Na_2SO_4). Purification *via* flash column chromatography [PE/EtOAc, 6:1 to 3:1] afforded a diastereomeric mixture of benzoyl-protected ceramide **SI2** (83.0 mg, 0.105 mmol, 99%) as a light orange solid.

R_f = 0.45 [Pent: EtOAc 3:1]

^{1}H NMR (400 MHz, $CDCl_3$): δ = 8.06–8.01 (m, 2H), 7.84–7.76 (m, 4H), 7.56–7.50 (m, 1H), 7.44–7.37 (m, 2H), 7.33–7.28 (m, 2H), 7.25–7.22 (m, 2H), 6.27 (d, *J* = 8.2 Hz, 1H), 5.79–5.70 (m, 1H), 5.39 (ddt, *J* = 15.4, 7.2, 1.5 Hz, 1H), 4.57 (dtd, *J* = 8.8, 4.2, 1.9 Hz, 1H), 4.54–4.42 (m, 3H), 4.24 (dd, *J* = 7.3, 4.0 Hz, 1H), 3.95 (dq, *J* = 11.2, 2.4 Hz, 1H), 3.86 (ddp, *J* = 10.5, 5.9, 2.8 Hz, 1H), 3.74 (dddt, *J* = 16.5, 14.4, 6.9, 4.1 Hz, 1H), 3.56–3.46 (m, 1H), 3.46–3.29 (m, 1H), 2.67 (td, *J* = 7.9, 5.6 Hz, 4H), 2.19 (td, *J* = 7.2, 2.4 Hz, 2H), 2.00 (dq, *J* = 22.1, 7.2 Hz, 4H), 1.80 (d, *J* = 5.8 Hz, 2H), 1.75–1.59 (m, 4H), 1.59–1.44 (m, 6H), 1.43–1.18 (m, 24H), 0.94 (t, *J* = 7.3 Hz, 3H), 0.89–0.84 (m, 3H) ppm.

^{13}C NMR (101 MHz, $CDCl_3$): δ = 172.2, 166.8, 151.3, 151.1, 146.4, 144.9, 136.3, 133.1, 129.8, 129.2, 129.2, 128.5, 126.3, 122.9, 122.8, 98.8, 97.2, 78.1, 77.2, 68.4, 67.8, 67.6, 63.7, 63.6, 62.4, 51.6, 36.2, 35.7, 35.1, 33.6, 32.4, 32.0, 31.0, 29.8, 29.8, 29.7, 29.6, 29.5, 29.3, 29.2, 27.1, 25.6, 25.4, 22.8, 22.5, 20.4, 19.8, 14.3, 14.1 ppm.

IR (ATR): $\tilde{\nu}$ = 2925 (s), 2853 (s), 2358 (w), 2340 (w), 2190 (w), 1722 (m), 1684 (m), 1654 (m), 1602 (w), 1540 (w), 1453 (m), 1378 (m), 1352 (m), 1272 (s), 1201 (m), 1177 (m), 1157 (m), 1120 (s), 1076 (s), 1032 (s), 971 (m), 906 (m), 869 (m), 844 (m), 814 (m), 712 (m) cm^{-1}.

HRMS (ESI): calcd. for $C_{50}H_{72}N_3O_5^+$: 795.5500 $[M+H]^+$
found: 795.5502 $[M+H]^+$.

4-(4-((*E*)-(4-Butylphenyl)diazenyl)phenyl)-N-((2*S*,3*R*,*E*)-1-hydroxy-3-((tetrahydro-2H-pyran-2-yl)oxy)octadec-4-en-2-yl)butanamide (Azo-THP-Cer)

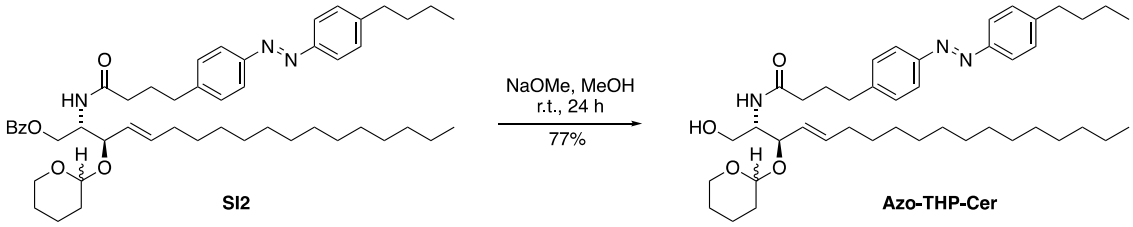

To a solution of fully protected **SI2** (30.3 mg, 38.2 µmol, 1.0 eq.) in dry MeOH (2 mL) was added catalytic sodium methoxide in MeOH (prepared from 1 mL of MeOH and 12 mg MeONa, 200 µL used) and the reaction was stirred for 24 h at room temperature. Then, H_2O (10 mL) was added and the aqueous layer was extracted with EtOAc (3 × 20 mL) and dried (Na_2SO_4). Purification *via* flash column chromatography [PE/EtOAc, 6:1 to 3:1] afforded a diastereomeric mixture of **Azo-THP-Cer** (20.3 mg, 29.4 µmol, 77%) as a light orange solid.

R_f = 0.38 [PE: EtOAc 1:2]

^{1}H NMR (400 MHz, $CDCl_3$): δ = 7.82 (dq, *J* = 8.7, 2.1 Hz, 4H), 7.35–7.28 (m, 4H), 6.42 (d, *J* = 7.6 Hz, 1H), 5.76–5.66 (m, 1H), 5.38 (ddt, *J* = 15.4, 7.1, 1.6 Hz, 1H), 4.45–4.38 (m, 1H), 4.19 (dd, *J* = 7.1, 4.8 Hz, 1H), 4.02–3.91 (m, 2H), 3.88–3.80 (m, 1H), 3.63 (q, J = 6.9, 6.4 Hz, 1H), 3.46 (dp, J = 13.4, 6.3, 5.6 Hz, 1H), 3.26 (d, J = 8.8 Hz, 1H), 2.71 (dt, J = 19.5, 7.7 Hz, 4H), 2.23 (td, J = 7.2, 2.4 Hz, 2H), 2.03 (dtd, J = 10.9, 7.5, 6.4, 3.1 Hz, 4H), 1.85 – 1.70 (m, 1H), 1.70 – 1.59 (m, 2H), 1.59 – 1.42 (m, 4H), 1.42 – 1.17 (m, 25H), 0.94 (t, J = 7.3 Hz, 3H), 0.89 – 0.85 (m, 3H) ppm.

^{13}C NMR (101 MHz, $CDCl_3$): δ = 172.8, 151.4, 151.1, 146.4, 144.9, 136.0, 129.3, 129.2, 126.5, 123.0, 122.9, 98.3, 79.1, 64.8, 62.6, 54.0, 36.0, 35.7, 35.2, 33.6, 32.4, 32.1, 31.2, 29.8, 29.8, 29.8, 29.6, 29.6, 29.5, 29.3, 29.2, 27.1, 25.3, 22.8, 22.5, 21.1, 14.3, 14.1 ppm.

IR (ATR): $\tilde{\nu}$ = 3303 (bm), 2924 (s), 2853 (m), 1645 (m), 1602 (w), 1546 (w), 1499 (w), 1466 (m), 1378 (w), 1184 (w), 1118 (m), 1074 (m), 1022 (m), 970 (m), 844 (m) cm^{-1}.

HRMS (EI): calcd. for $C_{43}H_{68}N_3O_4^+$: 690.5204 $[M+H]^+$
found: 690.5208 $[M+H]^+$.

Tetrahydropyrane-protected azosphingomyelin (Azo-THP-SM)

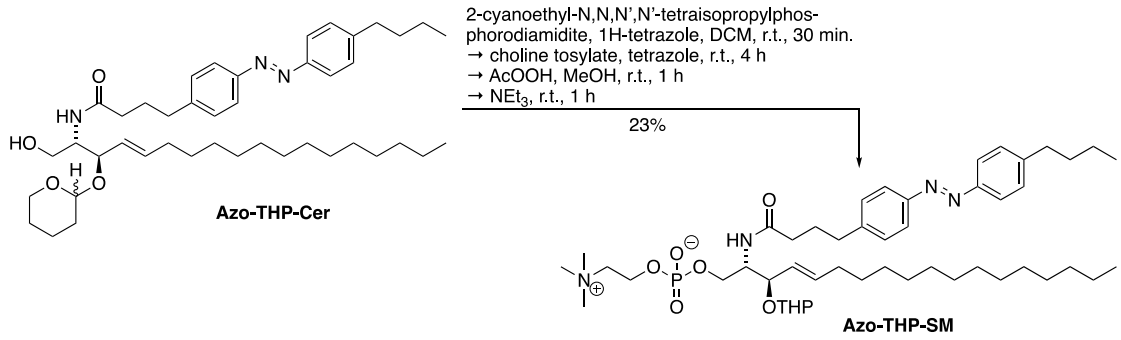

To a solution of a diastereomeric mixture of **Azo-THP-Cer** (26 mg, 37 µmol, 1.0 eq) in dry DCM (1.5 mL) were added 4 Å molecular sieves (0.30 g) and 2-cyanoethyl-*N*,*N*,*N*',*N*'-tetraisopropylphosphorodiamidite (17 mg, 18 µL, 56 µmol, 1.5 eq.) and 1*H*-tetrazole (0.45 M, 0.10 mL, 44 µmol, 1.2 eq.) at room temperature under Ar. The solution was stirred for 30 min at room temperature. To the reaction mixture was added 1*H*-tetrazole (0.45 M, 0.24 mL, 0.11 mmol, 3.0 eq.), followed by choline tosylate (41 mg, 0.15 mmol, 4.0 eq.) at room temperature. The reaction mixture was stirred for 4 h at room temperature, then MeOH (0.8 mL) and AcOOH (39% in AcOH, 11 µL, 56 µmol, 1.5 eq.) were added, followed by stirring for a further 1 h at room temperature. After that time, 30% aq NH_3 (1 mL) was added to the mixture, and the reaction was stirred for 1 h at room temperature. The solution was filtered and concentrated. The product was purified by first elution through TMD-8 resin (THF/water, 90:10), then subsequently by flash column chromatography (silica gel, $CHCl_3$/MeOH/water, 65:25:1 to 65:25:4) to give as **Azo-THP-SM** (7.4 mg, 8.65 mmol, 23%) as an orange solid.

R_f = 0.28 [$CHCl_3$:MeOH:H_2O 65:25:4]

^{1}H NMR (400 MHz, CD_3OD): δ = 7.87 – 7.78 (m, 4H), 7.44 – 7.32 (m, 4H), 5.71 (dt, J = 15.3, 6.6 Hz, 1H), 5.37 – 5.17 (m, 1H), 4.29 – 4.22 (m, 2H), 4.16 – 4.12 (m, 2H), 4.08 – 4.00 (m, 1H), 3.88 (qd, J = 7.2, 6.2, 3.5 Hz, 1H), 3.61 (dd, J = 5.6, 3.7 Hz, 2H), 3.45 (s, 1H), 3.20 (d, J = 2.2 Hz, 9H), 2.72 (q, J = 7.3 Hz, 4H), 2.27 (t, J = 7.5 Hz, 2H), 2.04 – 1.92 (m, 4H), 1.88 – 1.82 (m, 1H), 1.66 (td, J = 7.4, 2.0 Hz, 2H), 1.55 – 1.50 (m, 3H), 1.40 (q, J = 7.5 Hz, 3H), 1.32 – 1.19 (m, 24H), 0.97 (t, J = 7.4 Hz, 3H), 0.88 (t, J = 6.8 Hz, 3H) ppm.

^{13}C NMR (151 MHz, CD_3OD): δ = 175.4, 152.5, 152.3, 147.8, 146.7, 139.1, 130.4, 130.2, 130.0, 129.9, 127.8, 123.9, 123.8, 121.8, 121.8, 95.8, 76.6, 67.4, 65.7 (d, *J* = 5.5 Hz), 63.5, 60.5 (d, *J* = 4.9 Hz), 54.69, 54.66, 54.2 (d, *J* = 7.6 Hz), 36.8, 36.5, 36.2, 34.8, 33.4, 33.1, 31.8, 30.83, 30.82, 30.80, 30.79, 30.6, 30.5, 30.4, 30.3, 28.9, 26.7, 23.8, 23.4, 20.5, 14.5, 14.3 ppm.

IR (ATR): $\tilde{\nu}$ = 3389 (br), 2923 (s), 2851 (m), 2359 (w), 1367 (m)=, 1454 (m), 1247 (m), 1087 (m), 968 (m), 836 (w) cm^{-1}.

HRMS (EI): calcd. for $C_{44}H_{70}N_3O_8^+$: 855.5759 $[M+H]^+$
found: 855.5752 $[M+H]^+$.

Azosphingomyelin (Azo-SM)

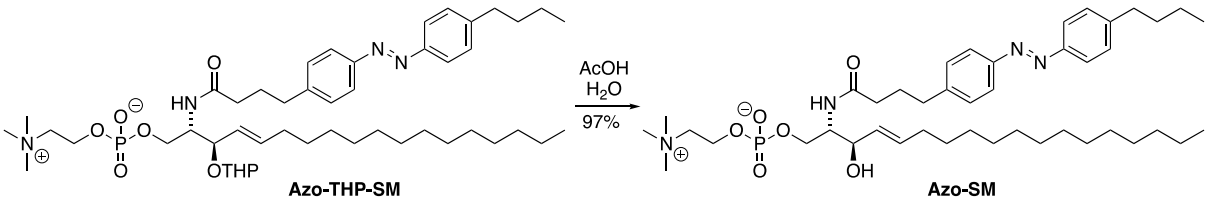

A solution of **Azo-THP-SM** (4.2 mg, 4.91 µmol) in AcOH (0.7 mL) and H_2O (0.35 mL) was stirred for 6 h at 40 °C and concentrated under reduced pressure. Purification of the resulting residue by flash column chromatography ($CHCl_3$:MeOH:H_2O 65:25:4) gave **Azo-SM** (3.7 mg, 4.76 µmol, 97%) as an orange solid.

$\mathbf{R_f}$ = 0.18 [$CHCl_3$:MeOH:H_2O 65:25:4]

^{1}H NMR (400 MHz, CD_3OD): δ = 7.82 (dd, J = 8.3, 6.4 Hz, 4H), 7.37 (dd, J = 11.7, 8.4 Hz, 4H), 5.70 (dt, J = 15.3, 6.6 Hz, 1H), 5.45 (ddt, J = 15.2, 7.7, 1.5 Hz, 1H), 4.32 – 4.23 (m, 2H), 4.13 – 3.96 (m, 4H), 3.62 (dd, J = 5.3, 3.9 Hz, 2H), 3.21 (s, 9H), 2.71 (td, J = 7.8, 3.9 Hz, 4H), 2.27 (t, J = 7.5 Hz, 2H), 2.00 – 1.90 (m, 4H), 1.70 – 1.62 (m, 2H), 1.40 (q, J = 7.5 Hz, 2H), 1.32 – 1.18 (m, 22H), 0.97 (t, J = 7.4 Hz, 3H), 0.88 (t, J = 6.9 Hz, 3H) ppm.

^{13}C NMR (151 MHz, CD_3OD): δ = 175.4, 152.5, 152.3, 147.8, 146.7, 135.3, 131.2, 130.3, 130.2, 123.9, 123.8, 72.6, 67.5, 65.8 (d, *J*= 5.0 Hz), 60.4 (d, *J* = 5.0 Hz), 55.3 (d, *J* = 7.4 Hz), 54.7, 54.7, 54.7, 36.8, 36.5, 36.3, 34.8, 33.4, 33.1, 30.8, 30.8, 30.8, 30.8, 30.7, 30.5, 30.5, 30.4, 28.9, 23.8, 23.4, 14.5, 14.3 ppm.

IR (ATR): $\tilde{\nu}$ = 3299 (br), 2920 (s), 2850 (m), 1643 (m), 1601 (w), 1556 (w), 1466 (m), 1375 (w), 1229 (m), 1148 (w), 1088 (s), 1048 (s), 968 (s), 838 (m) cm^{-1}.

HRMS (EI): calcd. for $C_{43}H_{72}N_4O_6P^+$: 771.5184 $[M+H]^+$
found: 771.5183 $[M+H]^+$.

(2*S*,3*R*,*E*)-2-Azidooctadec-4-ene-1,3-diol (SI3)

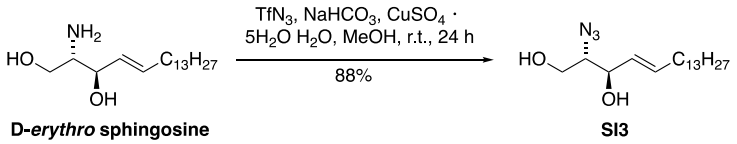

D-*erythro*-sphingosine (275 mg, 0.920 mmol, 1 eq.), $NaHCO_3$ (312 mg, 3.72 mg, 4 eq.) and $CuSO_4$•H_2O (8.80 mg, 40.0 µmol, 5 mol%) were dissolved in H_2O (1.2 mL). The emulsion was cooled to 0 °C and freshly prepared TfN_3 (2 M in toluene, 2.00 mL, 4.00 mmol, 4.3 eq.) was added. MeOH (2 mL) was added and the reaction was slowly allowed to warm to r.t. After 24 h, H_2O (20 mL) was added and the reaction mixture was extracted with EtOAc (3 × 20 mL), dried ($MgSO_4$) and concentrated under reduced pressure. Flash column chromatography [PE/EtOAc, 10:1 to 0:1] afforded azidosphingosine (**SI3**, 263 mg, 0.806 mmol, 88%) as a yellow oil.

R_f = 0.66 [PE/EtOAc, 1:1].

$[\alpha]_D^{20}$ = –0.14 (*c* = 1, DCM).

^{1}H NMR (400 MHz, $CDCl_3$): δ = 5.86–5.78 (m, 1H), 5.53 (ddt, *J* = 15.4, 7.4, 1.5 Hz, 1H), 4.27–4.23 (m, 1H), 3.78 (dd, *J* = 5.2, 3.9 Hz, 2H), 3.51 (q, *J* = 5.4 Hz, 1H), 2.14–2.00 (m, 2H), 1.47–1.32 (m, 2H), 1.32–1.19 (m, 21H), 0.88 (t, *J* = 6.8 Hz, 3H) ppm.

^{13}C NMR (101 MHz, $CDCl_3$): δ = 136.1, 127.9, 73.8, 66.7, 62.6, 32.3, 31.9, 29.7 – 29.2, 28.9, 14.1 ppm.

IR (ATR): $\tilde{\nu}$ = 3351 (w), 2919 (s), 2851 (s), 2100 (m), 1669 (w), 1467 (m), 1379 (m), 1266 (m), 1235 (m), 1195 (m), 1154 (m), 1003 (m), 971 (m), 704 (w) cm^{-1}.

HRMS (EI): calcd. for $C_{18}H_{34}O_2N_3^-$: 324.2657 $[M–H]^-$
found: 324.2658 $[M–H]^-$.

(2*S*,3*R*,*E*)-2-Azido-1-(trityloxy)octadec-4-en-3-ol (SI4)

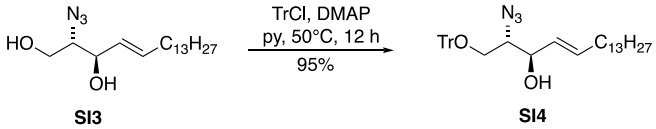

Azide **SI3** (263 mg, 0.806 mmol, 1eq.) was dissolved in pyridine (3 mL), then TrCl (274 mg, 0.887 mmol, 1.1 eq.) and DMAP (4.92 mg, 40.3 µmol, 0.05 eq.) were added. The mixture was stirred at 50 °C for 12 h. Afterwards, the solvent was removed under reduced pressure. The crude product

was purified by flash column chromatography on silica gel [PE/EtOAc, 10:1 to 3:1] to give protected alcohol **SI4** (437 mg, 0.771 mmol, 95%) as a colorless oil.

R_f = 0.65 [PE/EtOAc, 7:1].

$[\alpha]_D^{20}$ = 0.01 (*c* = 1, DCM).

^{1}H NMR (400 MHz, CD_3CN): δ = 7.37–7.32 (m, 6H), 7.21 (q, *J* = 6.8, 6.1 Hz, 6H), 7.16 (t, *J* = 7.1 Hz, 3H), 5.46 (dt, *J* = 14.3, 6.8 Hz, 1H), 5.22 (dd, *J* = 15.5, 7.1 Hz, 1H), 3.97 (t, *J* = 6.2 Hz, 1H), 3.49 (dt, *J* = 8.6, 4.4 Hz, 1H), 3.14–3.06 (m, 1H), 3.01 (dd, *J* = 9.9, 7.7 Hz, 1H), 3.14–3.06 (m, 2H), 3.01 (dd, *J* = 9.9, 7.7 Hz, 1H), 1.83 (dq, *J* = 5.2, 2.6 Hz, 2H), 1.01–1.21 (d, *J* = 13.9 Hz, 22H), 0.77 (t, *J* = 6.6 Hz, 3H) ppm.

^{13}C NMR (101 MHz, CD_3CN): δ = 144.8, 134.7, 129.9, 129.6, 129.4, 128.1, 87.8, 73.0, 67.2, 64.2, 32.7, 32.6–29.7, 23.3, 14.4 ppm.

IR (ATR): $\tilde{\nu}$ = 3422 (bw), 3059 (w), 3033 (w), 2924 (s), 2954 (m), 2362 (w), 2098 (m), 1669 (w), 15098 (w), 1491 (w=, 1448 (m), 1271 (w), 1221 (w), 1184 (w), 1155 (w), 1077 (m), 1033 (w), 1015 (w), 972 (w), 989 (w), 764 (m), 746 (m), 702 (s) cm^{-1}.

HRMS (EI): calcd. For $C_{37}H_{48}N_3O_2^-$: 566.3752 $[M–H]^–$
found: 566.3746 $[M–H]^–$.

(2*S*,3*R*,*E*)-2-Azido-1-(trityloxy)octadec-4-en-3-yl benzoate (SI5)

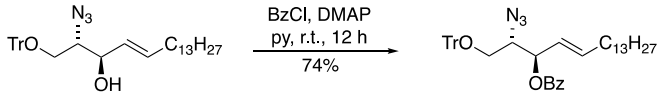

SI4 **SI5**

To a solution of secondary alcohol **SI4** (437 mg, 0.771 mmol, 1 eq.) in pyridine (12 mL) were added benzoylchloride (0.187 mL, 1.54 mmol, 2 eq.) and DMAP (4.71 mg, 38.6 µmol, 0.05 eq.). The mixture was stirred at room temperature for 12 h. The solvent was removed under reduced pressure and flash column chromatography on silica gel [PE/EtOAc, 1:0 to 2:1] afforded protected D-*erythro*-sphingosine **SI5** (383 mg, 0.570 mmol, 74%) as a colorless oil.

R_f = 0.79 [PE/EtOAc, 7:1]

$[\alpha]_D$ = –0.003 (*c* = 1, DCM).

^{1}H NMR (400 MHz, $CDCl_3$): δ = 7.91–7.85 (m, 2H), 7.53–7.45 (m, 1H), 7.39–7.32 (m, 6H), 7.24–7.17 (m, 6H), 7.17–7.11 (m, 3H), 5.74 (dt, *J* = 15.4, 6.7 Hz, 1H), 5.56 (dd, *J* = 7.9, 4.8 Hz, 1H), 5.35 (ddt,

J = 15.4, 7.9, 1.5 Hz, 1H), 3.79 (dt, *J* = 6.8, 5.0 Hz, 1H), 3.22 (dd, *J* = 9.8, 6.8 Hz, 1H), 3.12 (dd, *J* = 9.8, 5.2 Hz, 1H), 1.89 (qt, *J* = 7.0, 1.7 Hz, 2H), 1.29–1.06 (m, 22H), 0.86–0.74 (m, 3H) ppm.

^{13}C NMR (101 MHz, $CDCl_3$): *δ* = 165.3, 143.6, 138.5, 133.2, 129.9, 129.8, 128.7, 128.5, 128.2, 128.0, 127.3, 123.2, 87.3, 74.9, 64.6, 63.0, 32.4, 32.1, 29.9–29.3, 28.8, 22.9, 14.3 ppm.

IR (ATR): $\tilde{\nu}$ = 2924 (m), 2853 (m), 2098 (m), 1723 (m), 1602 (w), 1491 (w), 1466 (w), 1450 (m), 1315 (w), 1263 (s), 1177 (w), 1154 (w), 1092 (m), 1069 (m), 1026 (m), 970 (m), 899 (w), 774 (w), 764 (m), 741 (m), 703 (s) cm^{-1}.

HRMS (ESI): calcd. for $C_{44}H_{57}N_4O_3^+$ 689.4425 [M+NH_4^+]
found: 689.4442 [M+NH_4^+].

(2*S*,3*R*,*E*)-2-Azido-1-hydroxyoctadec-4-en-3-yl benzoate (SI6)

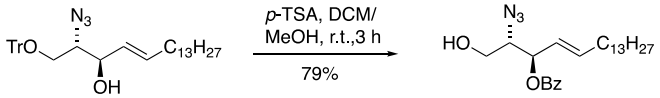

SI5 **SI6**

To a solution of protected D-*erythro*-sphingosine (**SI5**, 72.6 mg, 0.108 mmol, 1 eq.) in DCM (1 mL) and MeOH (1 mL) was added *p*-toluenesulforic acid hydrate (20.5 mg, 0.108 mmol, 1.0 eq.) and the reaction was stirred at room temperature for 3 h. All volatiles were removed under reduced pressure and the crude product was purified by flash column chromatography [PE/EtOAc, 10:1 to 3:1] to give primary alcohol (**SI6**, 27.6 mg, 85.1 µmol, 79%) as a colorless oil.

R_f = 0.66 [PE/EtOAc, 4:1].

$[\alpha]_D^{20}$ = –0.38 (*c* = 1, DCM).

^{1}H NMR (400 MHz, $CDCl_3$): *δ* = 8.06 (d, *J* = 7.7 Hz, 2H), 7.59 (t, *J* = 7.4 Hz, 1H), 7.46 (t, *J* = 7.6 Hz, 2H), 5.96 (ddd, *J* = 13.8, 8.7, 4.3 Hz, 1H), 5.68–5.57 (m, 2H), 3.85–3.70 (m, 2H), 3.63 (dd, *J* = 11.6, 7.0 Hz, 1H), 2.08 (q, *J* = 7.1 Hz, 2H), 1.57 (bs, 1H), 1.39 (t, *J* = 7.2 Hz, 2H), 1.24 (d, *J* = 3.7 Hz, 16H), 0.88 (t, *J* = 6.7 Hz, 3H) ppm.

^{13}C NMR (101 MHz, $CDCl_3$): *δ* = 165.5, 138.7, 133.4, 129.8 (C-5), 129.7, 128.5, 123.2, 74.6, 66.2, 62.0, 32.4, 31.9–28.7, 22.7, 14.1 ppm.

IR (ATR): $\tilde{\nu}$ = 3428 (bw), 2923 (s), 2853 (s), 2168 (w), 2101 (s), 1722 (s), 1602 (w), 1452 (m), 1316 (m), 1265 (s), 1177 (m), 1110 (s), 1068 (s), 1026 (m), 970 (m), 860 (w), 710 (s), 686 (m) cm^{-1}.

HRMS (EI): calcd. for $C_{25}H_{43}N_4O_3^-$: 447.3330 [M+NH_4^+]
found: 447.3336 [M+NH_4^+]

(2*R*,3*S*,4*S*,5*R*,6*R*)-2-(Acetoxymethyl)-6-(((2*S*,3*R*,*E*)-2-azido-3-(benzoyloxy)octadec-4-en-1-yl)oxy)tetrahydro-2*H*-pyran-3,4,5-triyl triacetate (SI8)

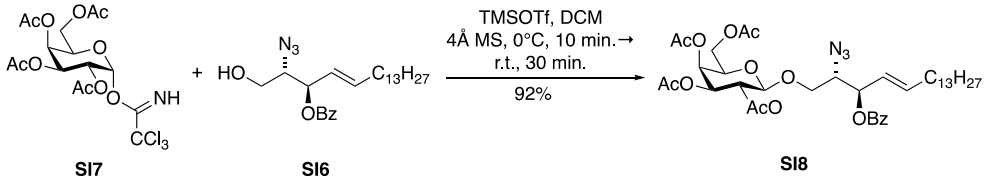

SI7 **SI6** **SI8**

Trichloroacetimidate **SI7**[R1] (225 mg, 0.456 mmol, 2.3 eq.) and acceptor **SI6** (100 mg, 0.198 mmol, 1.0 eq.) were combined and co-evaporated with toluene (3 × 5 mL) and with THF (1 × 5 mL), dried under high vacuum and then dissolved in DCM (0.8 mL). The mixture was stirred with freshly activated 4Å MS at room temperature for 30 min, before the reaction vessel was cooled to 0 °C and TESOTf (0.8 M in DCM, 31.7 µL, 39.6 µmol, 0.2 eq.) was added. After 10 min the reaction was allowed to warm to room temperature and after an additional 30 min the reaction was diluted with DCM and washed with saturated aqueous $NaHCO_3$ solution (10 mL). The aqueous layer was extracted with DCM (3 × 20 mL) and the combined organic phases were dried ($MgSO_4$) and concentrated under reduced pressure. Flash column chromatography (PE/EtOAc, 100:0 to 2:1) afforded protected glycoside (**SI8**, 139 mg, 0.182 mmol, 92%) as a colorless oil.

R_f = 0.50 [PE/EtOAc, 2:1].

$[\alpha]_D^{20}$ = –0.13 (*c* = 1, DCM)

^{1}H NMR (600 MHz, $CDCl_3$): δ = 8.08–8.02 (m, 2H), 7.57 (t, *J* = 7.4 Hz, 1H), 7.45 (t, *J* = 7.6 Hz, 2H), 5.93 (dt, *J* = 13.6, 6.7 Hz, 1H), 5.63–5.51 (m, 2H), 5.38 (d, J = 3.4 Hz, 1H), 5.23 (dd, *J* = 10.5, 7.9 Hz, 1H), 5.01 (dd, J = 10.4, 3.5 Hz, 1H), 4.49 (d, *J* = 8.0 Hz, 1H), 4.17–4.04 (m, 2H), 3.92 (m, 3H), 3.58 (dd, *J* = 9.1, 4.8 Hz, 1H), 2.15 (s, 3H), 2.10 (s, 3H), 2.09–2.03 (m, 3H), 2.02 (s, 3H), 1.98 (s, 4H), 1.37 (q, *J* = 7.0 Hz, 2H), 1.24 (d, *J* = 4.7 Hz, 23H), 0.87 (t, J = 6.7 Hz, 3H).

^{13}C NMR (101 MHz, $CDCl_3$): δ = 170.3, 170.2, 170.1, 169.3, 165.1, 139.1, 133.2, 129.9, 129.7, 128.4, 122.6, 101.0, 74.7, 70.8, 68.5, 68.0, 66.9, 63.5, 61.1, 32.4, 31.9–29.1, 28.7, 22.7, 20.7, 20.7, 20.6, 14.1 ppm.

IR (ATR): $\tilde{\nu}$ = 3428 (w), 3353 (w), 3296 (w), 1926 (m), 2854 (m), 2108 (m), 1726 (s), 1726 (s), 1601 (w), 1452 (w), 1370 (m), 1317 (w), 1252 (s), 1224 (s), 1176 (w), 1070 (m), 1026 (w), 973 (w), 957 (w), 916 (w), 827 (m), 713 (m) cm^{-1}.

HRMS (EI): calcd. for $C_{39}H_{61}N_4O_{12}^+$: 777.4280 $[M+NH_4]^+$
found: 777.4297 $[M+NH_4]^+$.

4-(4-((*E*)-(4-Butylphenyl)diazenyl)phenyl)-*N*-((2*S*,3*R*,*E*)-3-hydroxy-1-(((2*R*,3*R*,4*S*,5*R*,6*R*)-3,4,5-trihydroxy-6-(hydroxymethyl)tetrahydro-2*H*-pyran-2-yl)oxy)octadec-4-en-2-yl)butanamide (SI9)

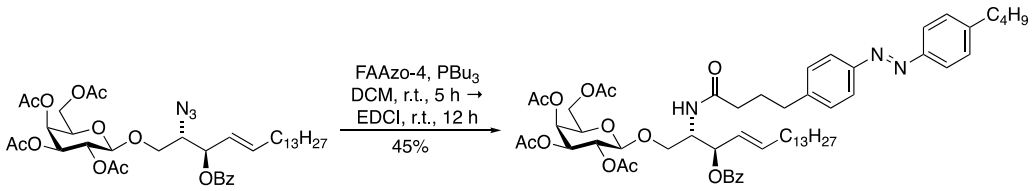

SI8 **SI9**

Glycoside **SI8** (23.9 mg, 31.5 µmol, 1 eq.) and FAAzo-4[R3] (15.3 mg, 47.2 µmol, 1.5 eq.) were dissolved in DCM (1 mL). Bu_3P (11.6 µL, 47.2 µmol, 1.5 eq.) was added and the reaction stirred for 6 h at room temperature. Then EDCI (22.0 mg, 142 µmol, 3 eq.) was added and the reaction mixture stirred at room temperature for another 12 h. The solvent was removed under reduced pressure and purification *via* flash column chromatography [PE/EtOAc, 10:1 to 0:1] afforded amide **SI9** (14.8 mg, 14.2 µmol, 45%) as a yellow oil.

R_f = 0.60 [PE/EtOAc, 1:2].

^{1}H NMR (600 MHz, $CDCl_3$): δ = 8.05–8.01 (m, 2H), 7.83–7.80 (m, 4H), 7.58–7.53 (m, 1H), 7.46–7.42 (m, 2H), 7.33–7.29 (m, 4H), 5.89 (dtd, *J* = 15.2, 6.7, 0.8 Hz, 1H), 5.78 (d, *J* = 9.1 Hz, 1H), 5.59–5.54 (m, 1H), 5.50 (ddt, *J* = 15.3, 7.6, 1.5 Hz, 1H), 5.35 (dd, *J* = 3.4, 1.2 Hz, 1H), 5.15 (dd, *J* = 10.5, 7.8 Hz, 1H), 4.99 (dd, *J* = 10.5, 3.4 Hz, 1H), 4.54–4.48 (m, 1H), 4.44 (d, *J* = 7.9 Hz, 1H), 4.07–4.00 (m, 2H), 3.96 (dd, *J* = 11.3, 6.3 Hz, 1H), 3.85 (ddd, *J* = 7.4, 6.4, 1.3 Hz, 1H), 3.68 (dd, *J* = 10.1, 4.3 Hz, 1H), 2.78–2.71 (m, 2H), 2.71–2.65 (m, 3H), 2.10–2.13 (m, 3H), 2.07–1.99 (m, 4H), 1.97 (s, 2H), 1.96 (s, 3H), 1.94 (s, 3H), 1.68–1.61 (m, 2H), 1.38 (h, *J* = 7.4 Hz, 3H), 1.35–1.17 (m, 27H), 0.94 (t, *J* = 7.4 Hz, 3H), 0.87 (t, *J* = 7.1 Hz, 3H) ppm.

^{13}C NMR (151 MHz, $CDCl_3$): δ = 172.3, 170.4, 170.3, 170.2, 169.7, 165.4, 151.4, 151.1, 146.5, 144.8, 137.7, 133.2, 129.8, 129.3, 129.2, 128.6, 124.8, 123.0, 122.9, 101.1, 74.5, 70.9, 70.8, 69.0, 67.3, 67.0, 61.2, 51.0, 36.0, 35.7, 35.2, 33.6, 32.5, 32.1, 29.8, 29.6, 29.5, 29.4, 29.1, 27.1, 22.8, 22.5, 20.9, 20.8, 20.7, 14.3, 14.1 ppm.

IR (ATR): $\tilde{\nu}$ = 2926 (m), 2854 (w), 1753 (s), 1672 (w), 1602 (w), 1531 (w), 1452 (w), 1369 (m), 1224 (s), 1176 (w), 1071 (m), 968 (w), 846 (w), 714 (m) cm^{-1}.

HRMS (ESI): calcd. for $C_{59}H_{82}N_3O_{13}^+$: 1040.5842 $[M+H]^+$
found: 1040.5880 $[M+H]^+$.

(2*R*,3*S*,4*S*,5*R*,6*R*)-2-(Acetoxymethyl)-6-(((2*S*,3*R*,*E*)-3-(benzoyloxy)-2-(4-(4-((*E*)-(4-butylphenyl)-di-azenyl)phenyl)butanamido)octadec-4-en-1-yl)oxy)tetrahydro-2*H*-pyran-3,4,5-triyl triacetate (Azo-*β*-Gal-Cer)

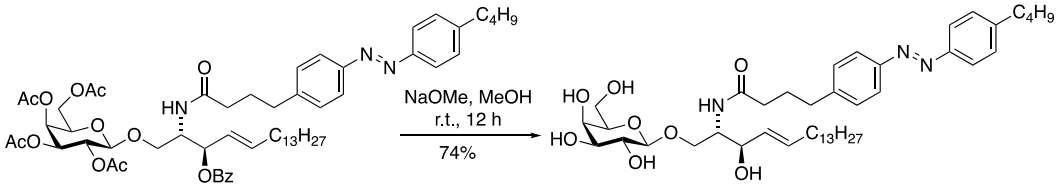

SI9 **Azo-*β*-Gal-Cer**

Protected glycosphingolipid (**SI9**, 13.6 mg, 13.1 µmol, 1.0 eq.) was dissolved in MeOH (1.5 mL) and NaOMe was added until pH 9–10. The reaction mixture was stirred at room temperature for 12 h. The reaction was stopped by the addition of DOWEX 50WX 2-100 (H^+ form) and stirred for another 30 min at room temperature. All solid material was removed by filtration through a pad of Celite®, which was washed with MeOH (5 mL) and the filtrate was concentrated under reduced pressure. Flash column chromatography [$CHCl_3$/MeOH, 10:1] afforded **Azo-β-Gal-Cer** (7.4 mg, 9.63 µmol, 74%) as yellow viscous oil.

R_f = 0.34 [DCM: MeOH 10:1]

^{1}H NMR (800 MHz, CD_3OD): *δ* = 7.85–7.80 (m, 4H), 7.42–7.33 (m, 4H), 5.69 (dtd, *J* = 15.3, 6.7, 0.9 Hz, 1H), 5.46 (ddt, *J* = 15.3, 7.8, 1.5 Hz, 1H), 4.23 (d, J = 7.7 Hz, 1H), 4.18 (dd, J = 10.1, 4.9 Hz, 1H), 4.10 (t, J = 8.1 Hz, 1H), 4.01 (ddd, *J* = 8.3, 4.9, 3.3 Hz, 1H), 3.83 (dd, *J* = 3.4, 1.1 Hz, 1H), 3.77 (dd, *J* = 11.4, 7.0 Hz, 1H), 3.72 (dd, *J* = 11.4, 5.2 Hz, 1H), 3.63 (dd, *J* = 10.2, 3.3 Hz, 1H), 3.59–3.55 (m, 1H), 3.55–3.51 (m, 1H), 3.48 (dd, *J* = 9.7, 3.4 Hz, 1H), 2.76–2.68 (m, 4H), 2.26 (t, *J* = 7.5 Hz, 2H), 2.02–1.93 (m, 4H), 1.71–1.64 (m, 2H), 1.41 (dt, *J* = 15.0, 7.4 Hz, 2H), 1.35–1.16 (m, 33H), 0.97 (t, J = 7.4 Hz, 3H), 0.88 (t, *J* = 7.2 Hz, 3H) ppm.

^{13}C NMR (101 MHz, $CDCl_3$): *δ* = 175.5, 152.5, 152.3, 147.8, 146.7, 135.2, 131.3, 130.3, 130.2, 123.9, 123.8, 105.4 (C-1), 76.8, 74.9, 73.1, 72.7, 70.3, 70.0, 62.6, 54.9, 49.0, 36.8, 36.5, 36.2, 34.8, 33.4, 33.1, 30.8, 30.8, 30.7, 30.5, 30.4, 30.4, 28.8, 23.8, 23.4, 14.5, 14.3 ppm.

IR (ATR): $\tilde{\nu}$ = 3288 (bm), 2924 (s), 2852 (m), 2168 (m), 1745 (m), 1558 (w), 1465 (m), 1003 (s), 727 (m) cm^{-1}.

HRMS (EI): calcd. for $C_{44}H_{70}N_3O_8^+$: 768.5167 $[M+H]^+$
found: 768.5157 $[M+H]^+$.

4-(4-((*E*)-(4-Butylphenyl)diazenyl)phenyl)-*N*-((2*S*,3*S*,4*R*)-1,3,4-trihydroxyoctadecan-2-yl)butanamide (Azo-PhCer)

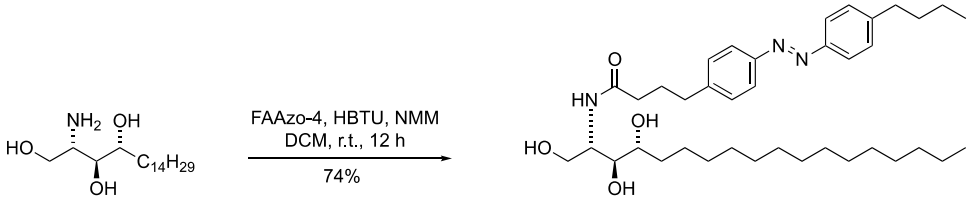

Phytosphingosine (4.3 mg, 14 µmol, 1.0 eq.) was dissolved in DCM (1 mL) and FAAzo-4 (4.4 mg, 14 µmol, 1 eq.) followed by HBTU (7.7 mg, 21 µmol, 1.5 eq.) and *N*-methylmorpholine (22 µL, 0.20 mmol, 15 eq.) were added and the reaction stirred at room temperature. After 12 h the solvent was removed under reduced pressure and the crude product was purified *via* flash column chromatography [DCM/MeOH, 10:0 to 10:1] to give **Azo-PhCer** (8.3 mg, 13 µmol, 93%) as yellow viscous oil.

R_f = 0.82 [DCM: MeOH 10:1]

^{1}H NMR (400 MHz, $CDCl_3$): δ = 7.82 (d, *J* = 8.1 Hz, 4H), 7.31 (d, *J* = 8.1 Hz, 4H), 6.39 (d, *J* = 7.6 Hz, 1H), 4.14 (td, *J* = 5.4, 2.9 Hz, 1H), 3.90 (dd, *J* = 11.5, 2.7 Hz, 1H), 3.71 (dd, *J* = 11.6, 5.5 Hz, 1H), 3.61 (dt, *J* = 8.8, 4.8 Hz, 1H), 3.55 (dd, *J* = 6.8, 3.1 Hz, 1H), 2.73 (t, *J* = 7.4 Hz, 2H), 2.68 (t, *J* = 7.7 Hz, 2H), 2.26 (t, *J* = 7.4 Hz, 2H), 2.02 (p, *J* = 7.5 Hz, 2H), 1.69 – 1.59 (m, 2H), 1.37 (dt, *J* = 14.8, 7.5 Hz, 2H), 1.24 (s, 24H), 0.94 (t, *J* = 7.4 Hz, 3H), 0.87 (t, *J* = 7.1 Hz, 3H) ppm.

^{13}C NMR (100 MHz, $CDCl_3$): δ = 173.8, 151.3, 150.9, 146.4, 144.4, 129.2, 129.1, 122.8, 76.6, 72.6, 61.8, 53.1, 35.6, 35.0, 33.5, 33.3–29.4 (C-6 , 26.8, 25.6, 22.7, 22.3, 14.1, 13.9 ppm.

IR (ATR): $\tilde{\nu}$ = 3295 (bm), 2956 (m), 1919 (s), 2851 (s), 1636 (m), 1603 (w), 1542 (w), 1498 (w), 1468 (m), 1481 (w), 1378 (w), 1156 (w), 1068 (w), 840 (w), 721 (w) cm^{-1}.

HRMS (EI): calcd. for $C_{38}H_{62}N_3O_4^+$: 624.4735 $[M+H]^+$
found: 624.4738 $[M+H]^+$.

References

[R1] Frank, J. A., Franquelim, H. G., Schwille, P. & Trauner, D., *J. Am. Chem. Soc.* **2016**, *138*, 12981–12986.

[R2] V. R. Krishnamurthy, A. Dougherty, M. Kamat, X. Song, R. D. Cummings, E. L. Chaikof, *Carbohydr. Res.* **2010**, *345*, 1541–1547.

[R3] J. A. Frank, M. Moroni, R. Moshourab, M. Sumser, G. R. Lewin, D. Trauner, *Nature Communications* **2015**, *6*, 7118.

NMR data

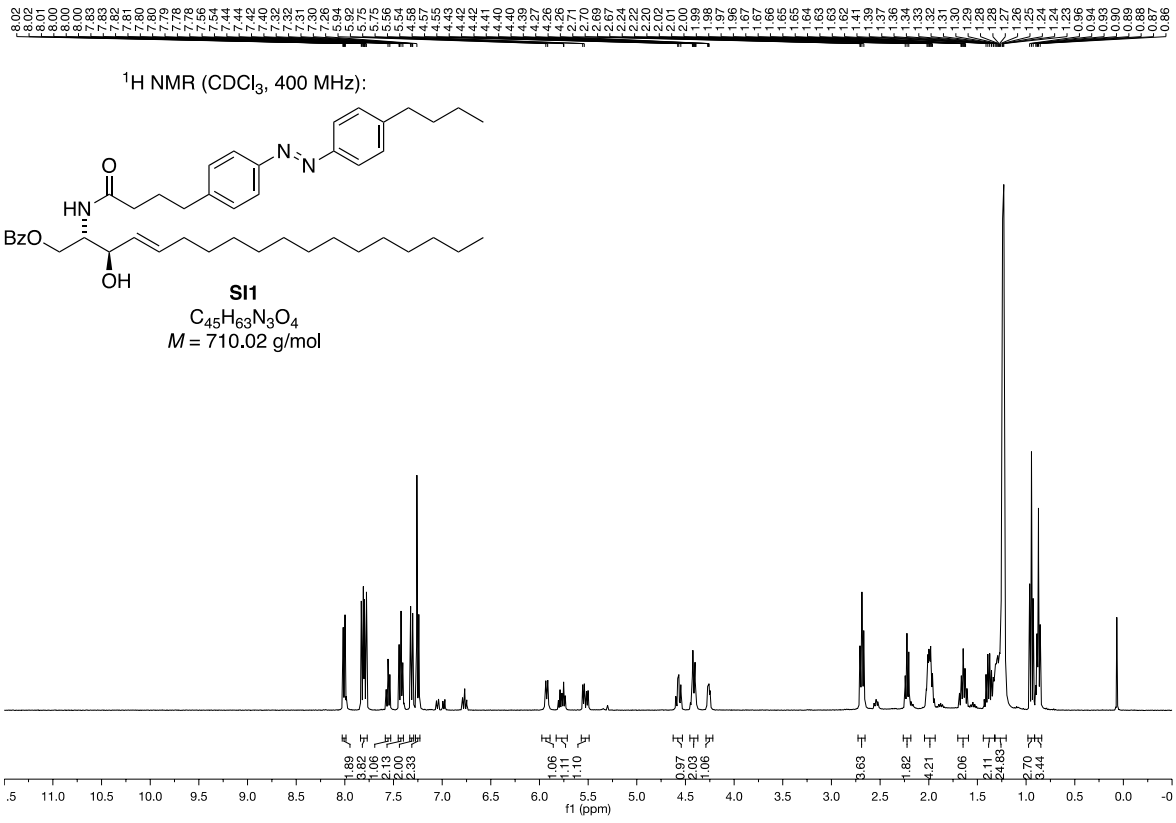
^{1}H NMR ($CDCl_3$, 400 MHz):
SI1
$C_{45}H_{63}N_3O_4$
M = 710.02 g/mol
f1 (ppm)

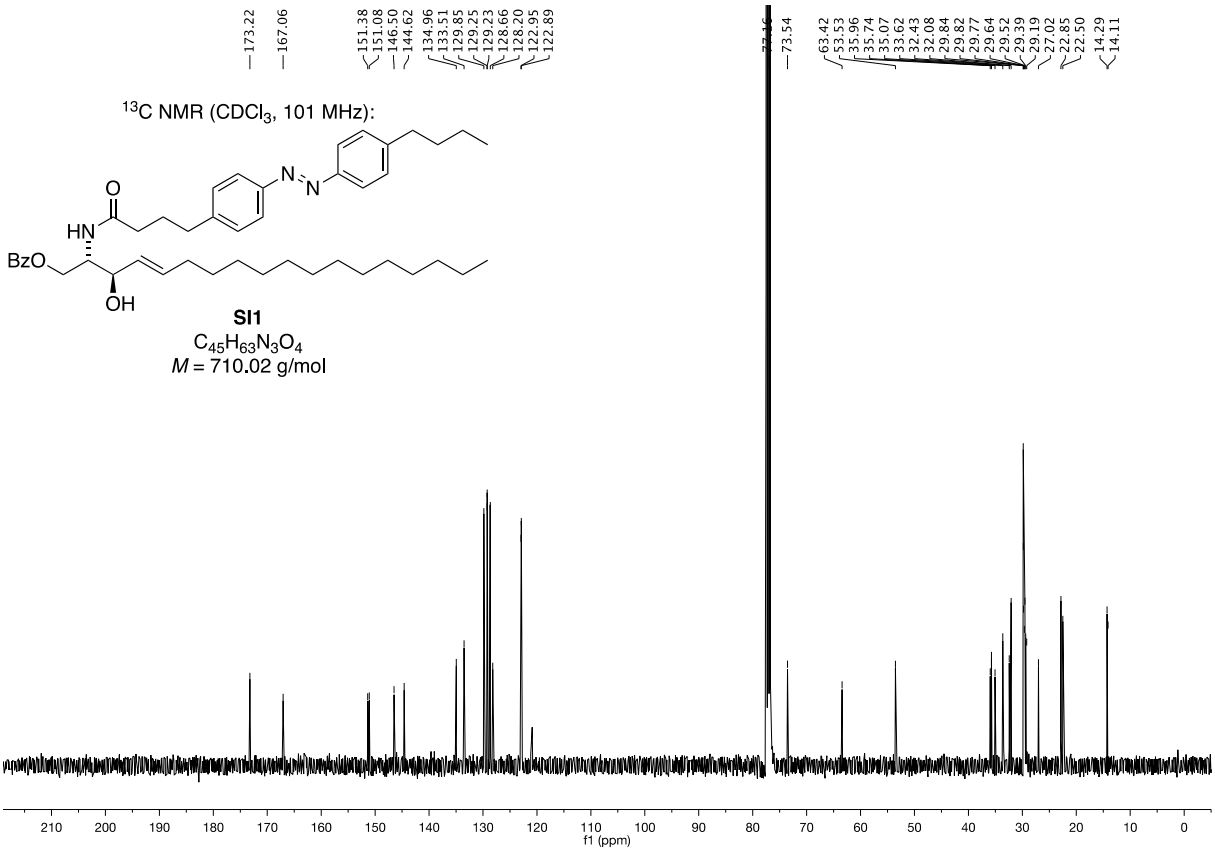
^{13}C NMR ($CDCl_3$, 101 MHz):
SI1
$C_{45}H_{63}N_3O_4$
M = 710.02 g/mol
f1 (ppm)

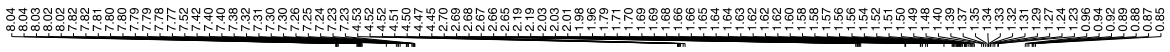

^{1}H NMR ($CDCl_3$, 400 MHz):

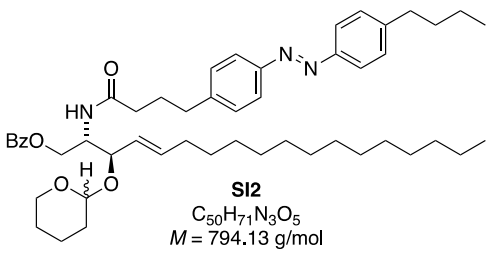

SI2
$C_{50}H_{71}N_3O_5$
M = 794.13 g/mol

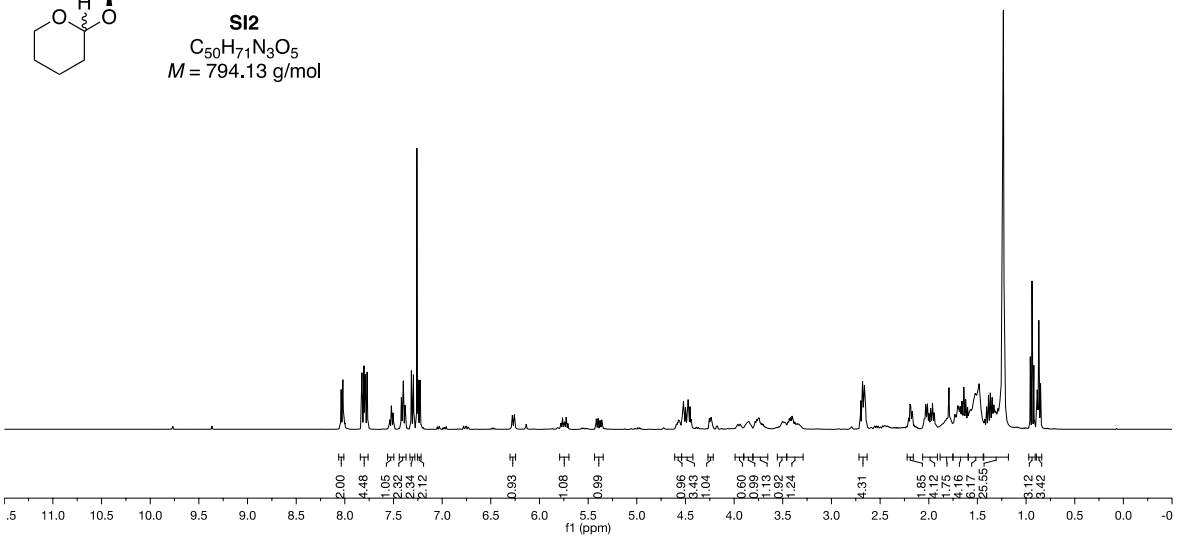

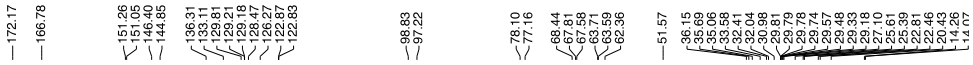

^{13}C NMR ($CDCl_3$, 101 MHz):

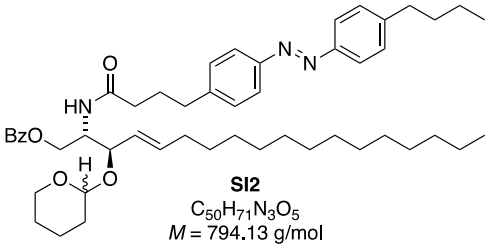

SI2
$C_{50}H_{71}N_3O_5$
M = 794.13 g/mol

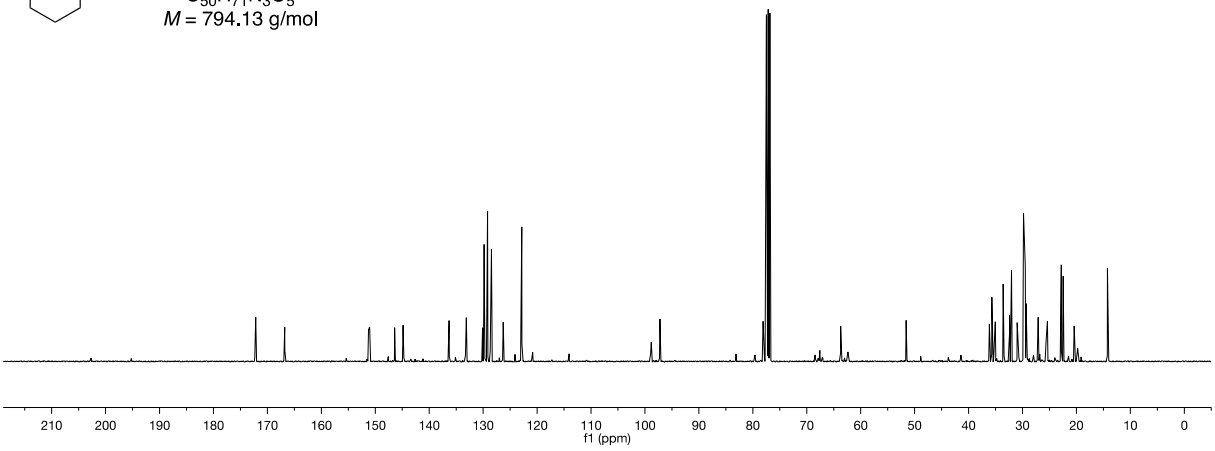

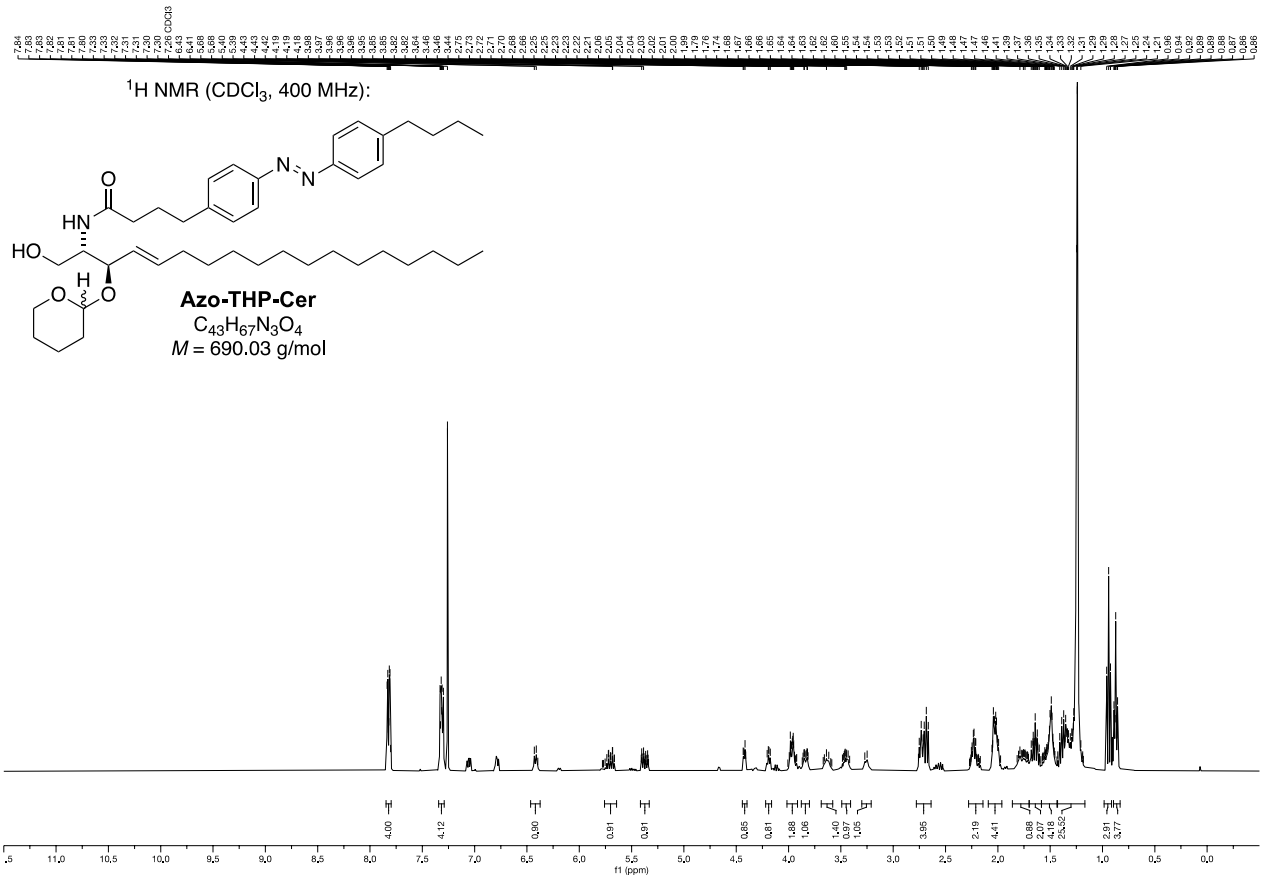
^{1}H NMR ($CDCl_3$, 400 MHz):
Azo-THP-Cer
$C_{43}H_{67}N_3O_4$
M = 690.03 g/mol
f1 (ppm)

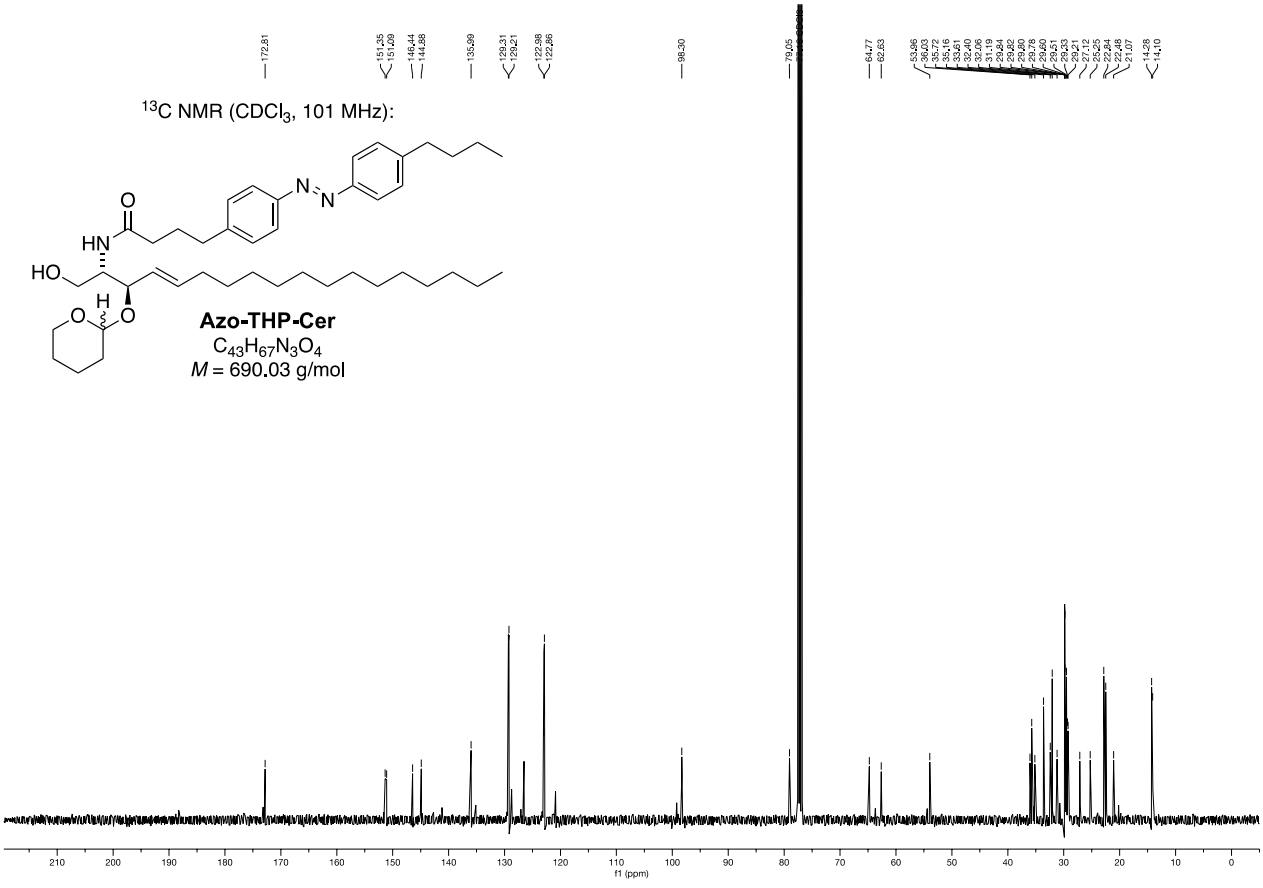
^{13}C NMR ($CDCl_3$, 101 MHz):
Azo-THP-Cer
$C_{43}H_{67}N_3O_4$
M = 690.03 g/mol
f1 (ppm)

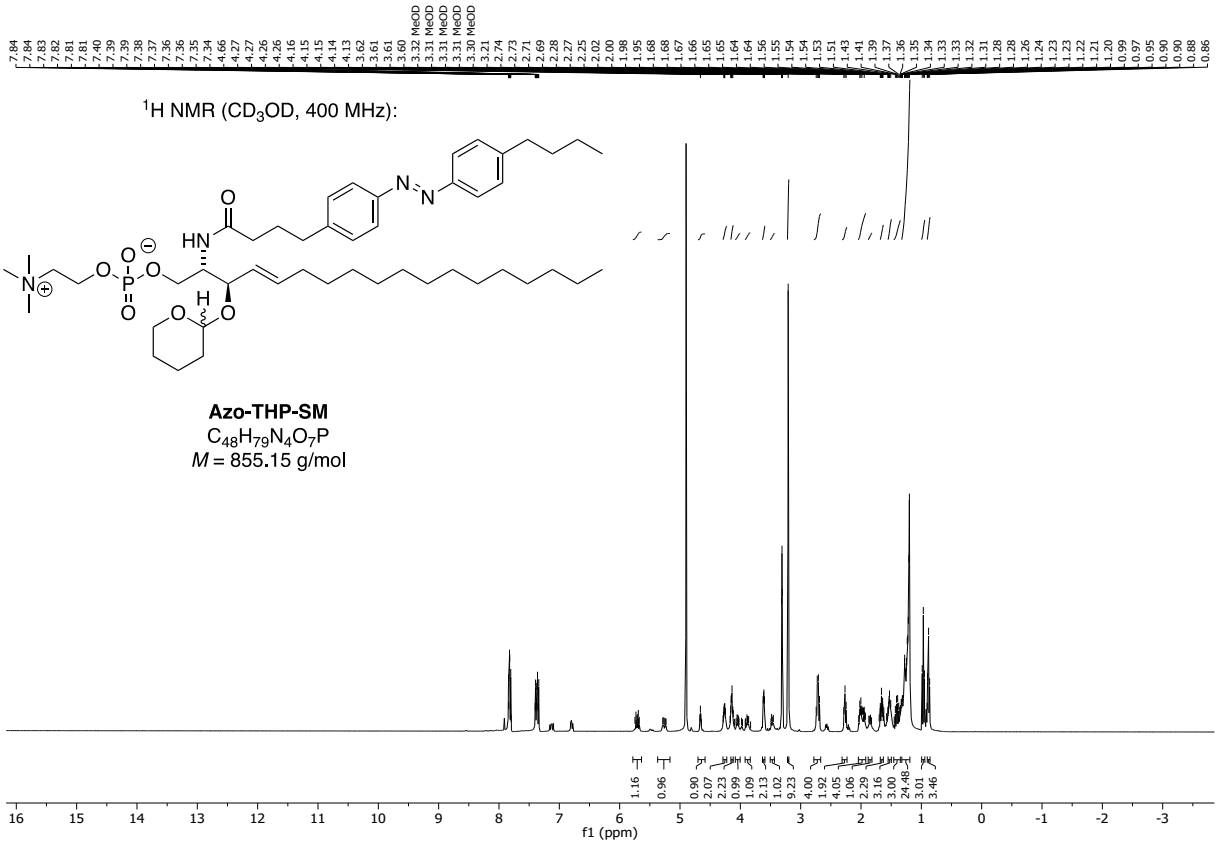
^{1}H NMR (CD_3OD, 400 MHz):
Azo-THP-SM
$C_{48}H_{79}N_4O_7P$
M = 855.15 g/mol
f1 (ppm)

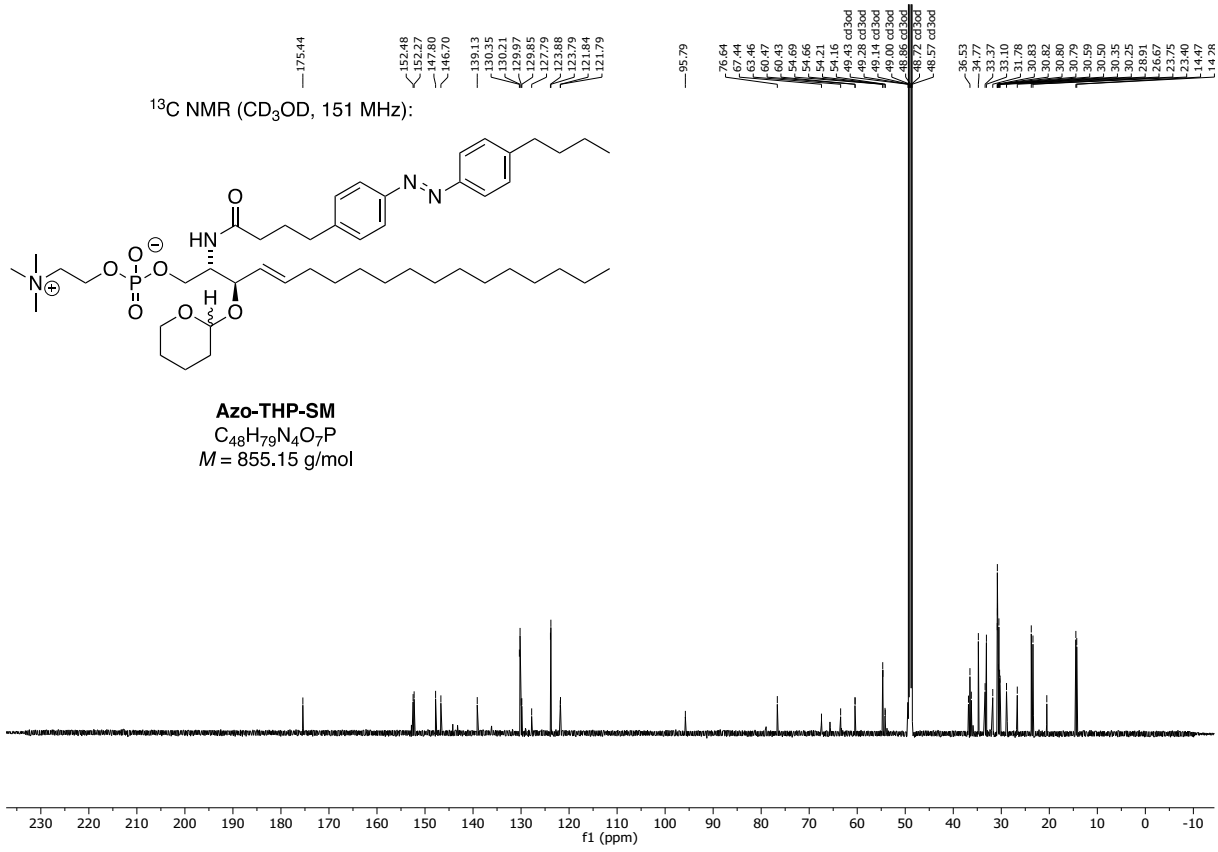
^{13}C NMR (CD_3OD, 151 MHz):
Azo-THP-SM
$C_{48}H_{79}N_4O_7P$
M = 855.15 g/mol
f1 (ppm)

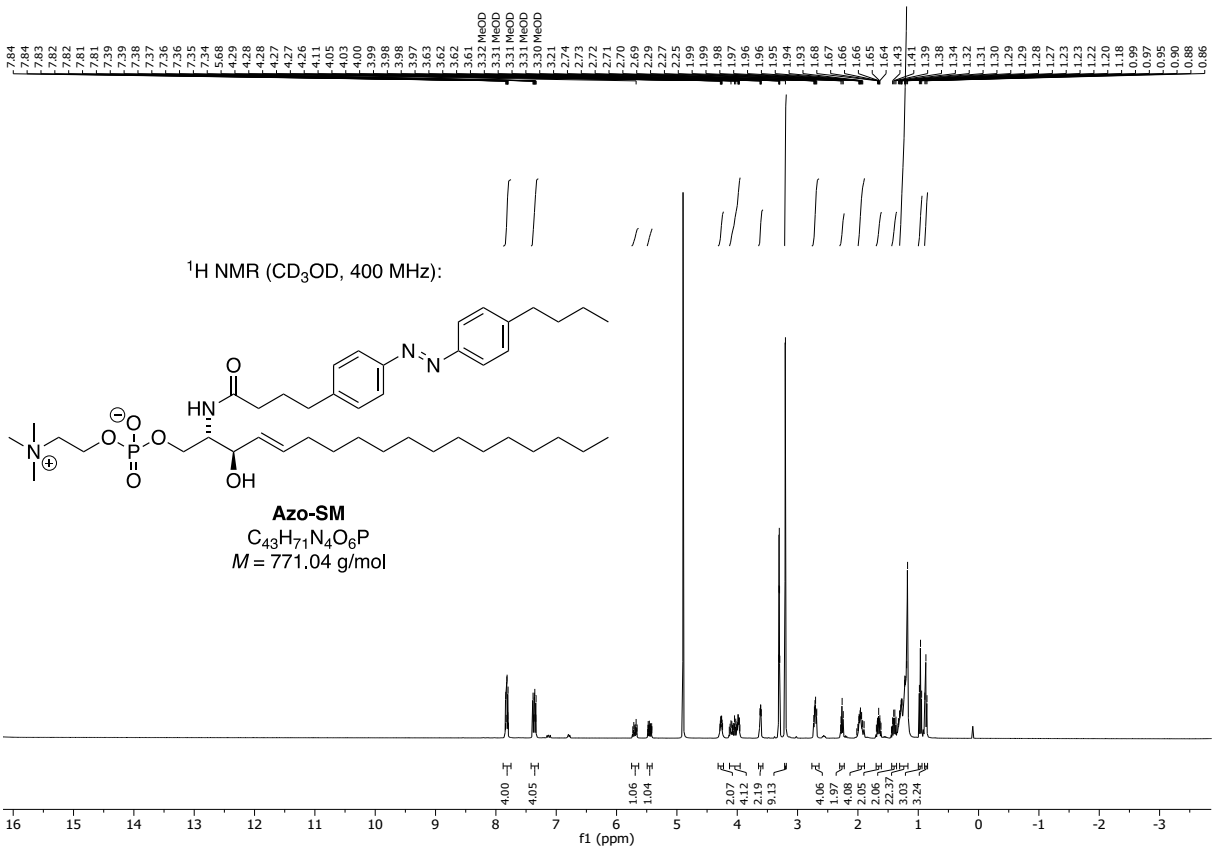

^{1}H NMR (CD_3OD, 400 MHz):

Azo-SM
$C_{43}H_{71}N_4O_6P$
M = 771.04 g/mol

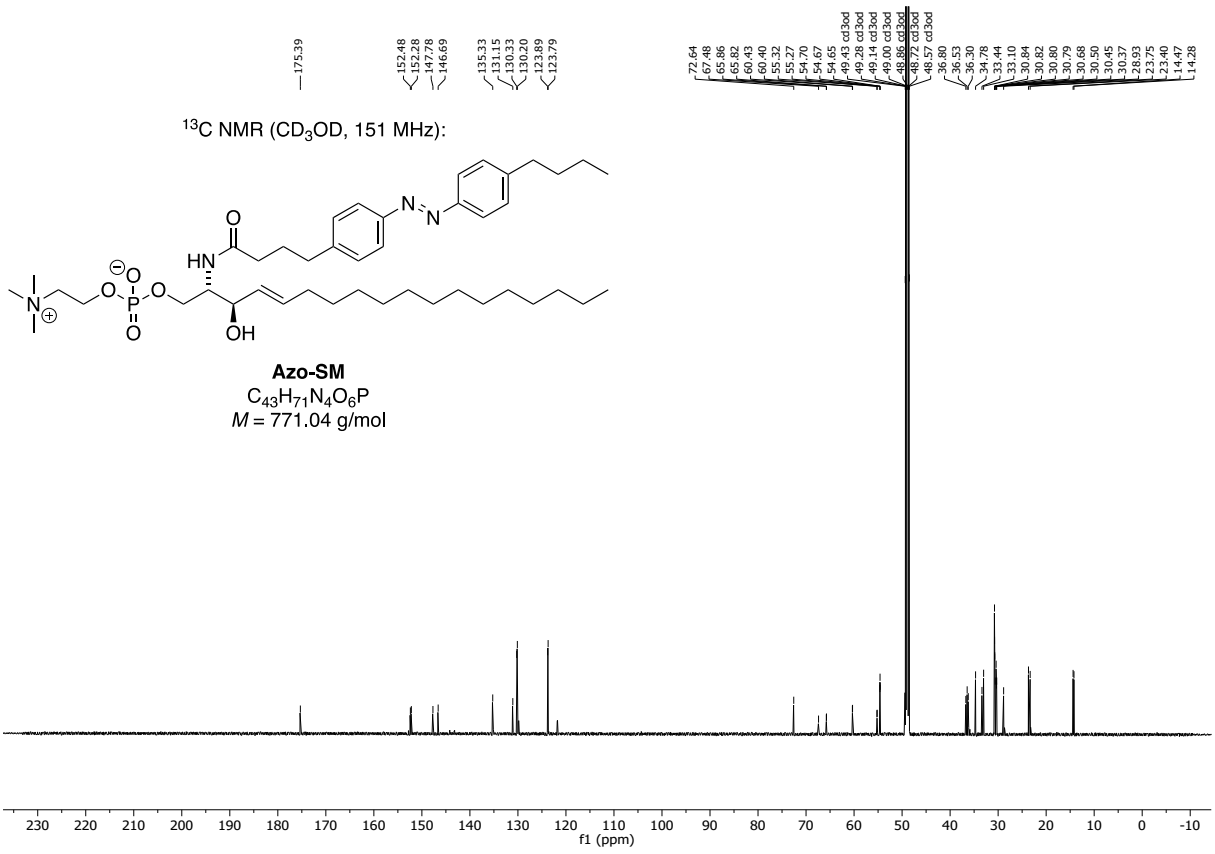

^{13}C NMR (CD_3OD, 151 MHz):

Azo-SM
$C_{43}H_{71}N_4O_6P$
M = 771.04 g/mol

^{1}H NMR ($CDCl_3$, 400 MHz):

SI3

$C_{18}H_{35}N_3O_2$

M = 325.50 g/mol

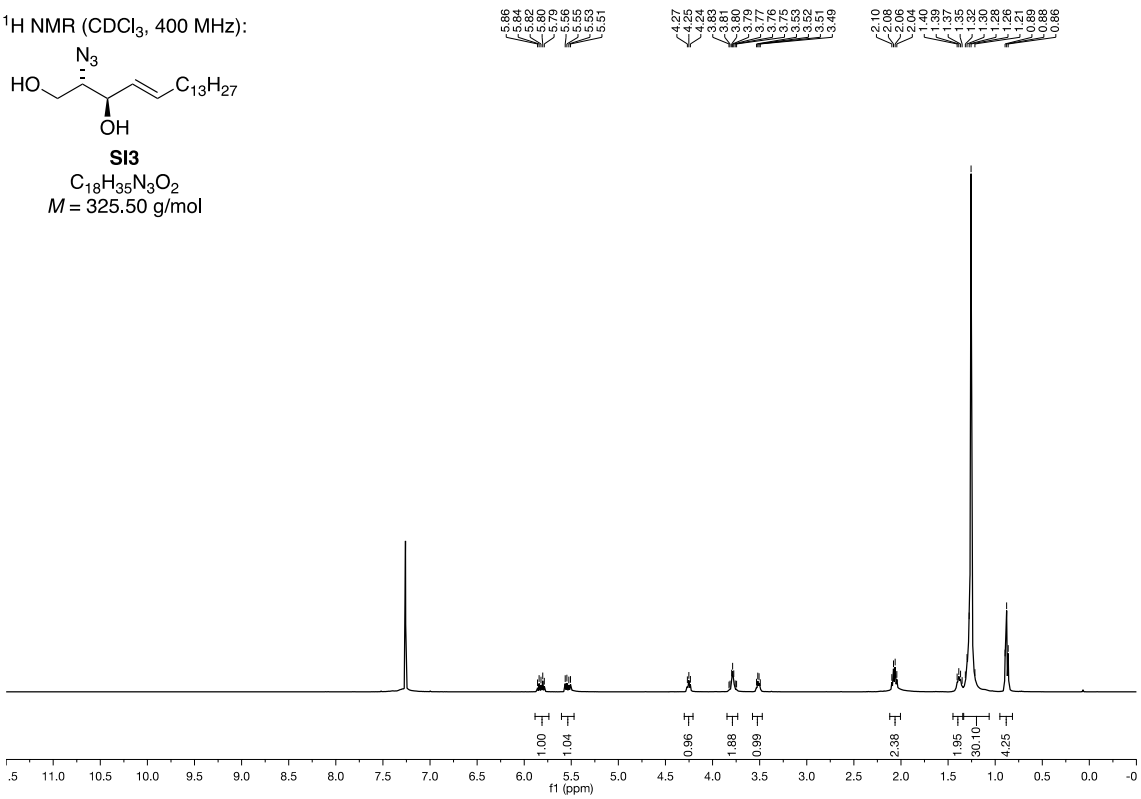

^{13}C NMR ($CDCl_3$, 101 MHz):

SI3

$C_{18}H_{35}N_3O_2$

M = 325.50 g/mol

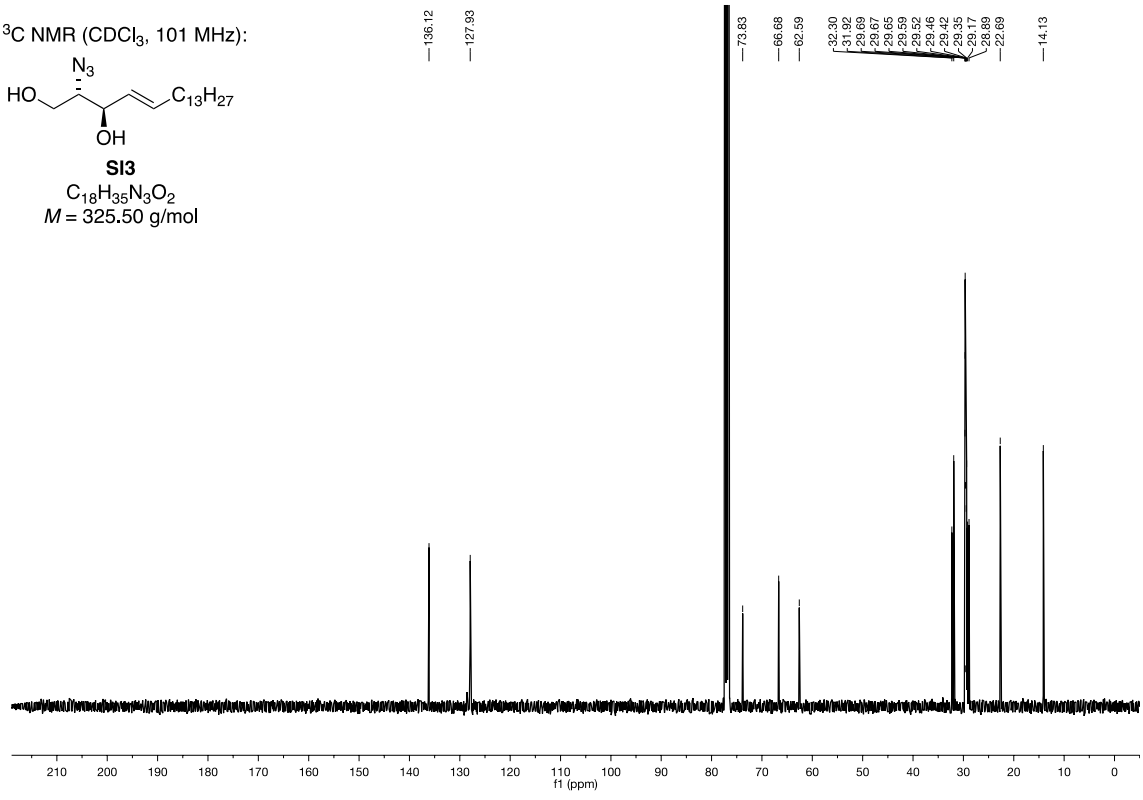

^{1}H NMR (CD_3CN, 400 MHz):

SI4
$C_{37}H_{49}N_3O_2$
M = 567.82 g/mol

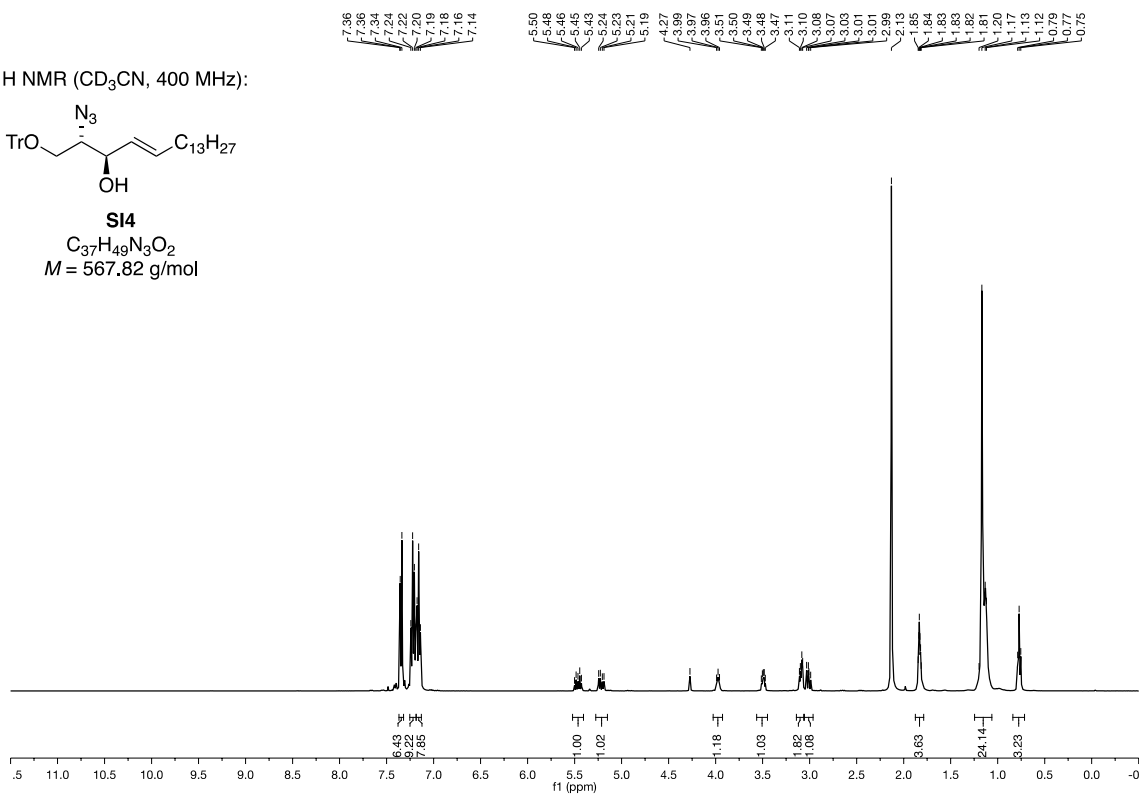

^{13}C NMR (CD_3CN, 101 MHz):

SI4
$C_{37}H_{49}N_3O_2$
M = 567.82 g/mol

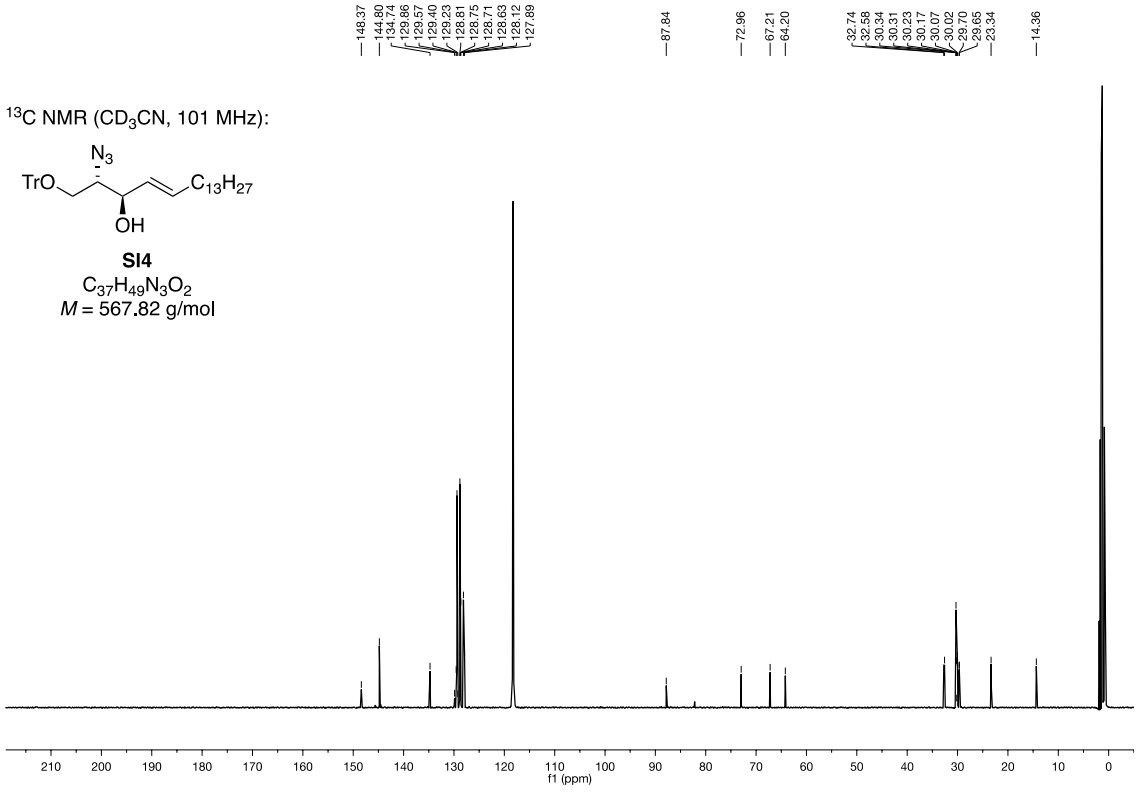

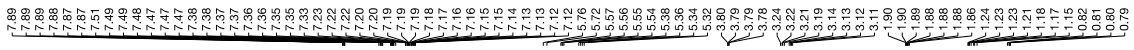

^{1}H NMR ($CDCl_3$, 400 MHz):

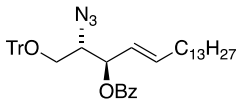

SI5

$C_{44}H_{53}N_3O_3$

M = 671.93 g/mol

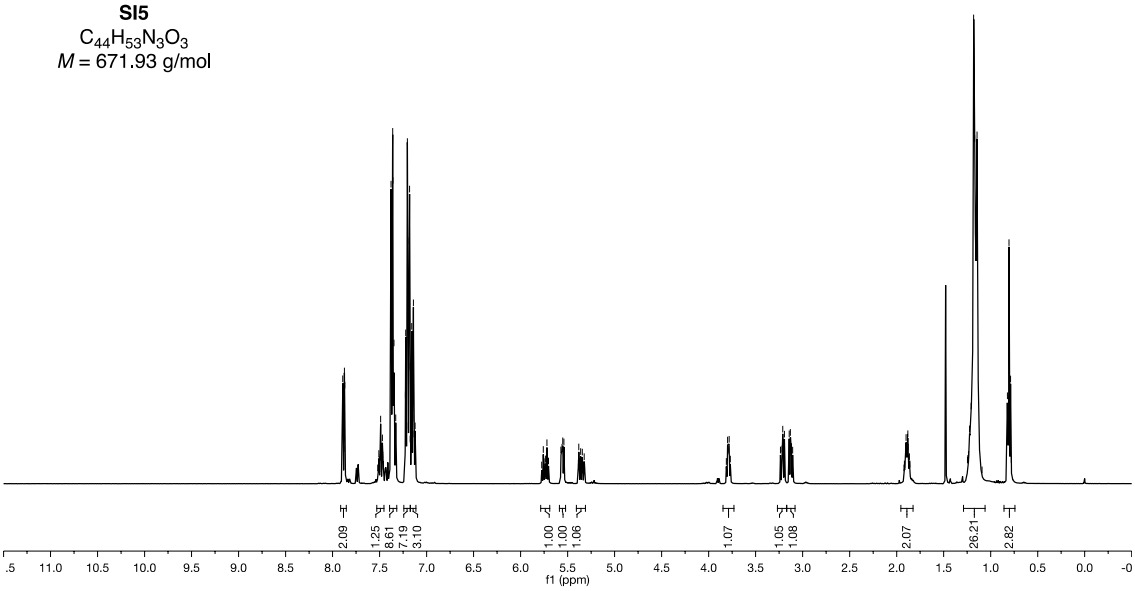

^{13}C NMR ($CDCl_3$, 101 MHz):

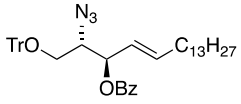

SI5

$C_{44}H_{53}N_3O_3$

M = 671.93 g/mol

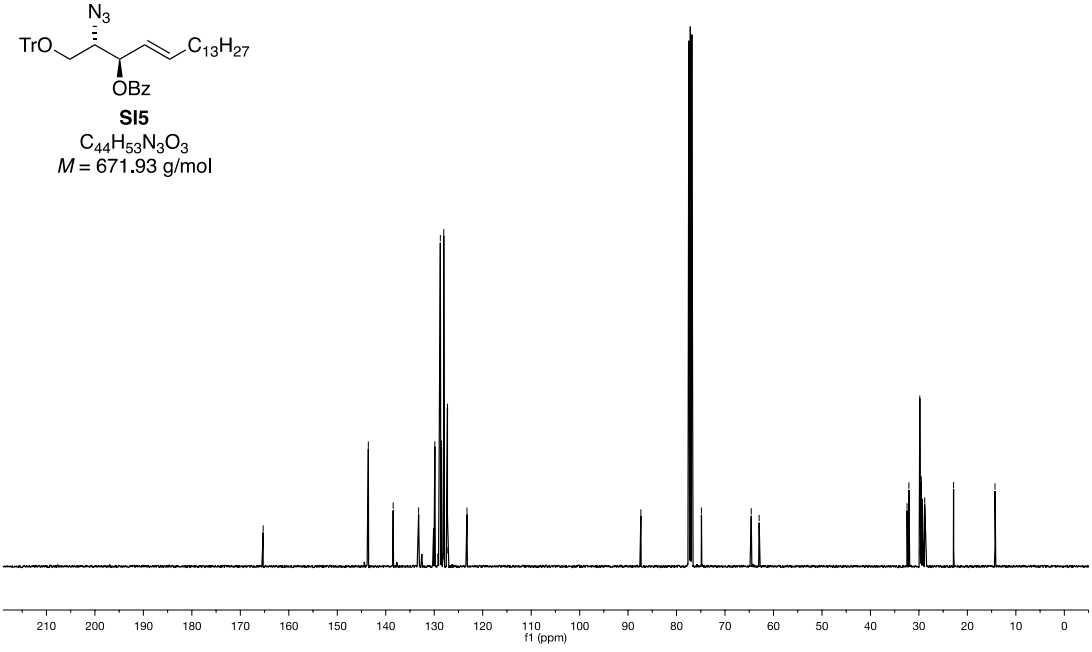

^{1}H NMR ($CDCl_3$, 400 MHz):

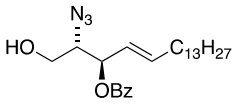

SI6

$C_{25}H_{39}N_3O_3$

M = 429.61 g/mol

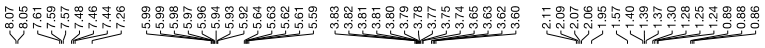

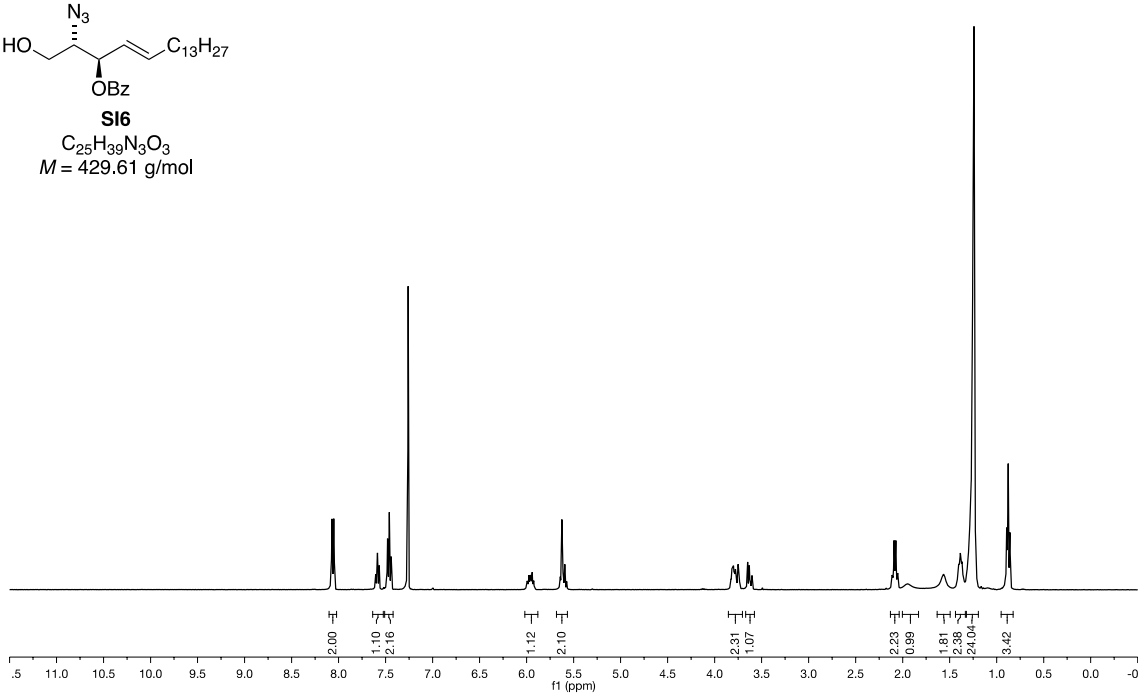

^{13}C NMR ($CDCl_3$, 101 MHz):

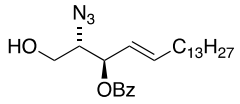

SI6

$C_{25}H_{39}N_3O_3$

M = 429.61 g/mol

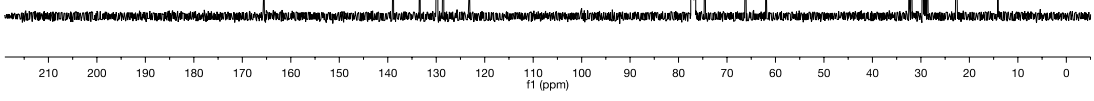

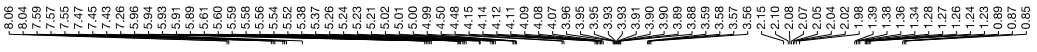

^{1}H NMR ($CDCl_3$, 600 MHz):

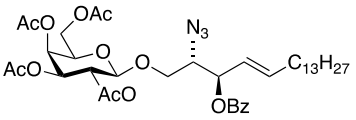

SI8
$C_{39}H_{57}N_3O_{12}$
M = 759.89 g/mol

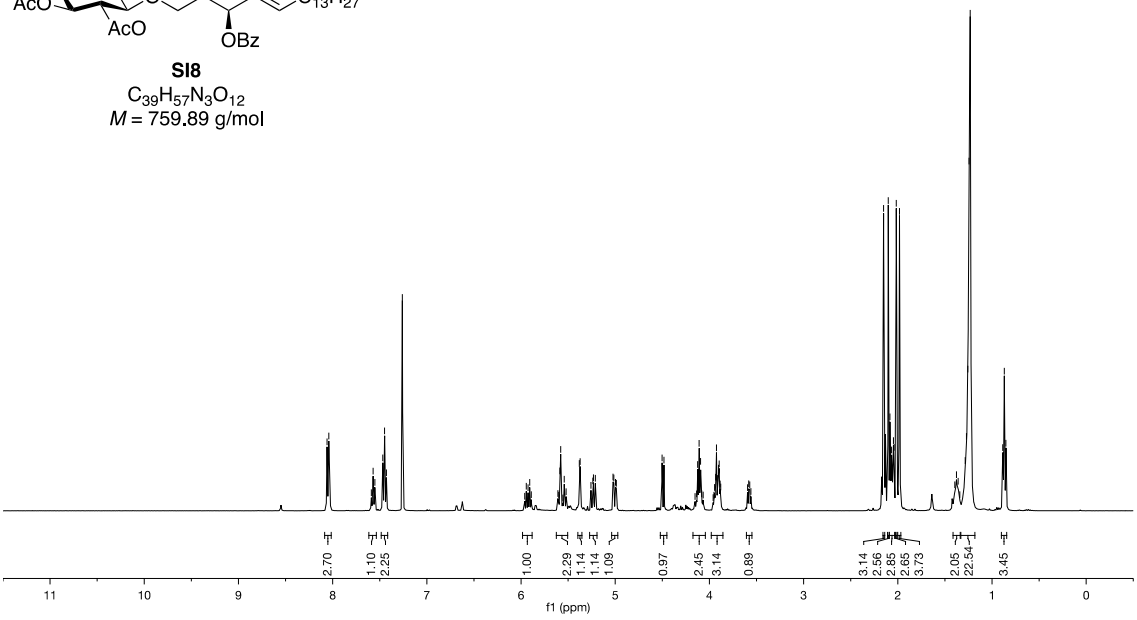

^{13}C NMR ($CDCl_3$, 151 MHz):

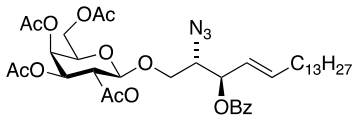

SI8
$C_{39}H_{57}N_3O_{12}$
M = 759.89 g/mol

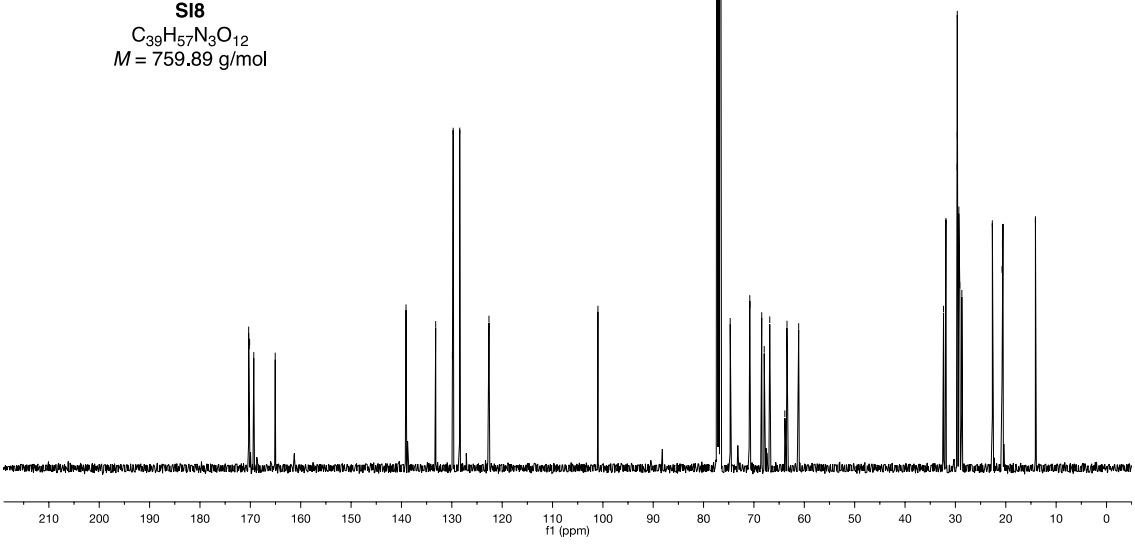

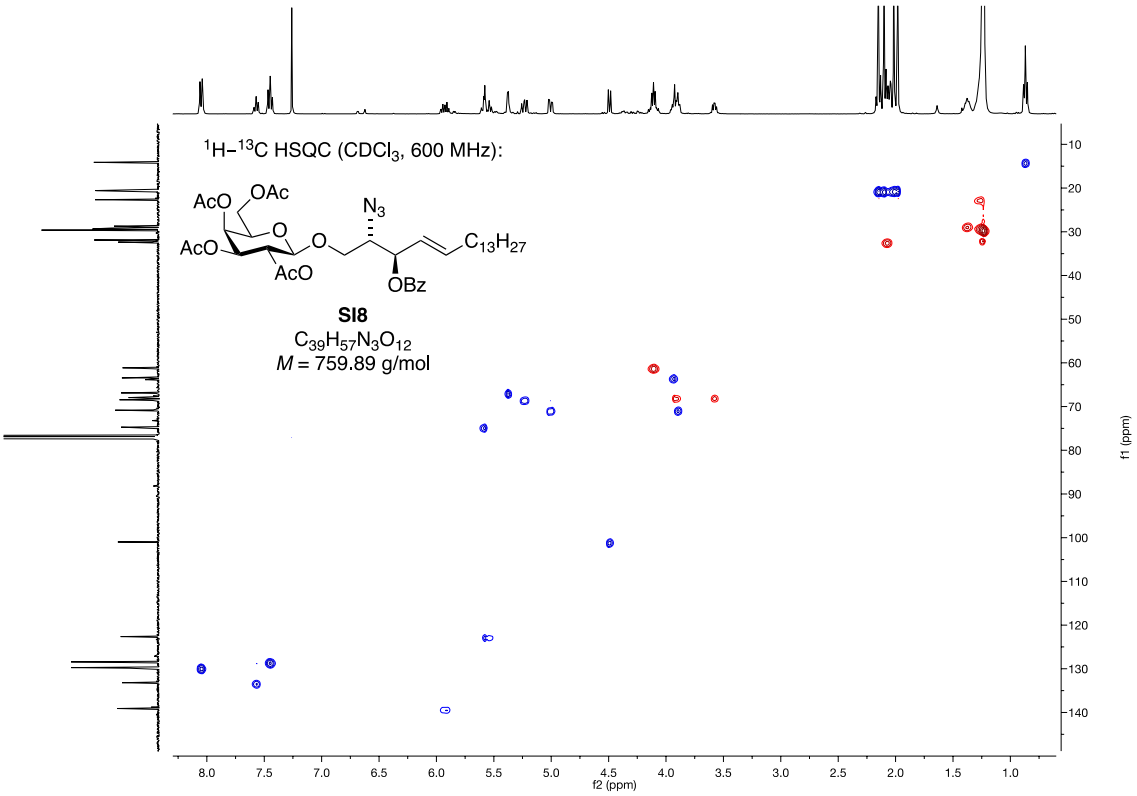
^{1}H–^{13}C HSQC ($CDCl_3$, 600 MHz):
AcO
OAc
AcO
AcO
O
O
N_3
$C_{13}H_{27}$
OBz
SI8
$C_{39}H_{57}N_3O_{12}$
M = 759.89 g/mol
f2 (ppm)
f1 (ppm)

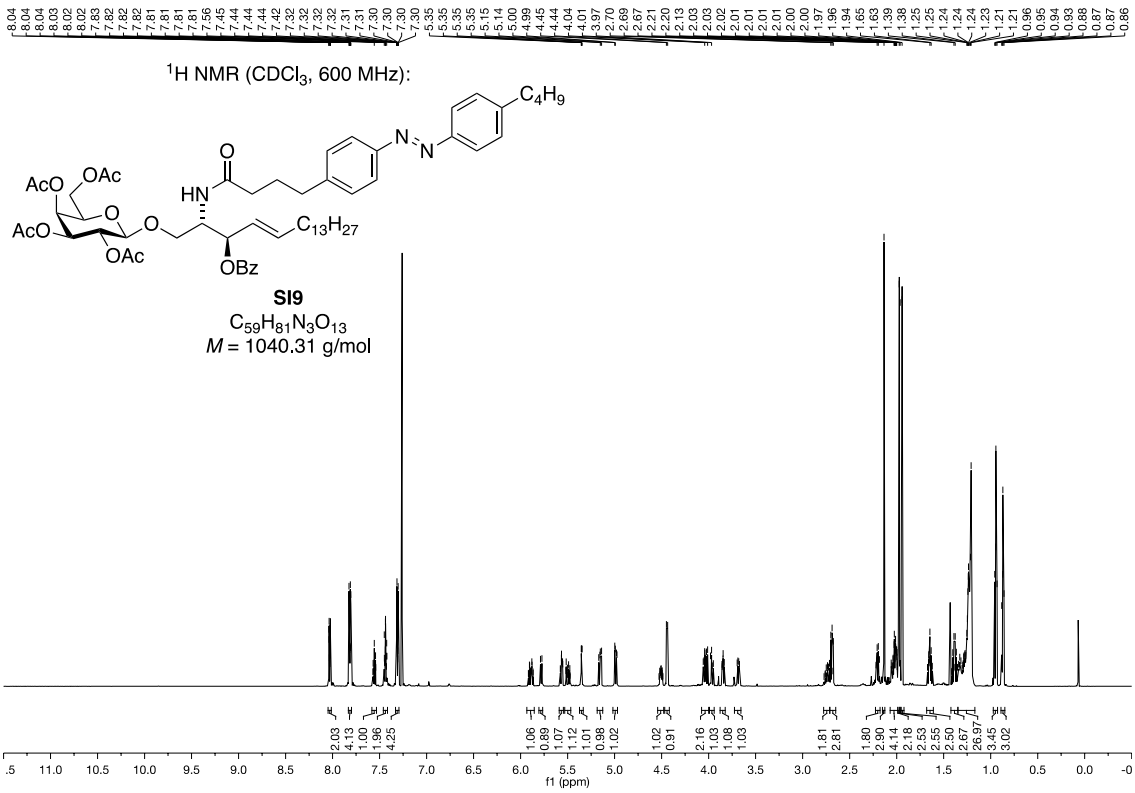
^{1}H NMR ($CDCl_3$, 600 MHz):
C_4H_9
N
N
O
HN
AcO
OAc
AcO
O
O
OAc
$C_{13}H_{27}$
OBz
SI9
$C_{59}H_{81}N_3O_{13}$
M = 1040.31 g/mol
f1 (ppm)

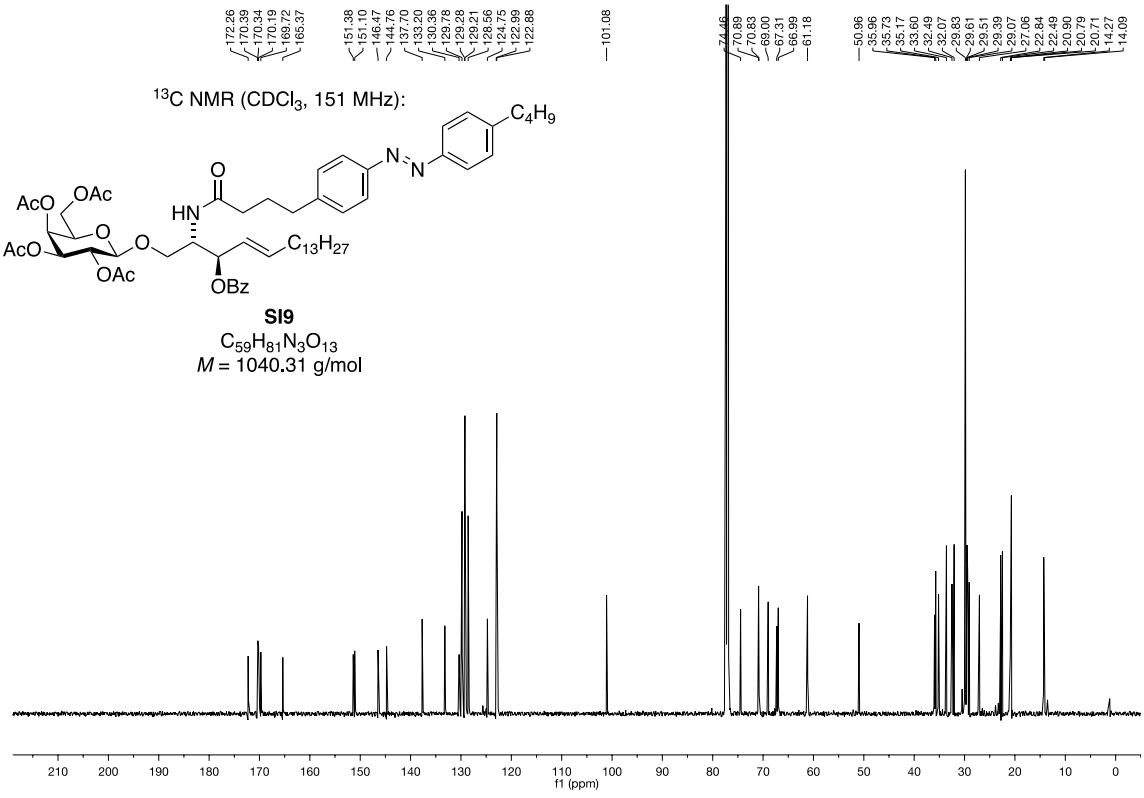
^{13}C NMR ($CDCl_3$, 151 MHz):
C_4H_9
N
N
O
HN
AcO
OAc
AcO
O
O
OAc
$C_{13}H_{27}$
OBz
SI9
$C_{59}H_{81}N_3O_{13}$
M = 1040.31 g/mol
f1 (ppm)

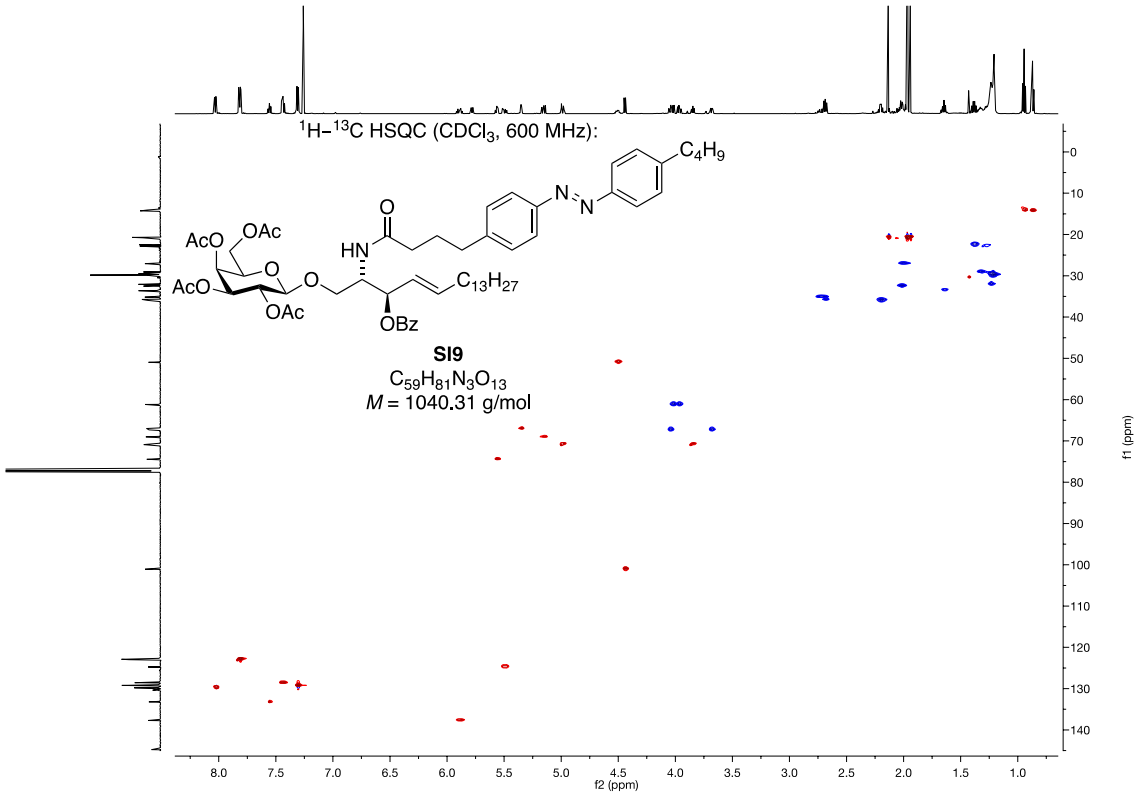
^{1}H–^{13}C HSQC ($CDCl_3$, 600 MHz):
SI9
$C_{59}H_{81}N_3O_{13}$
M = 1040.31 g/mol
f2 (ppm)
f1 (ppm)

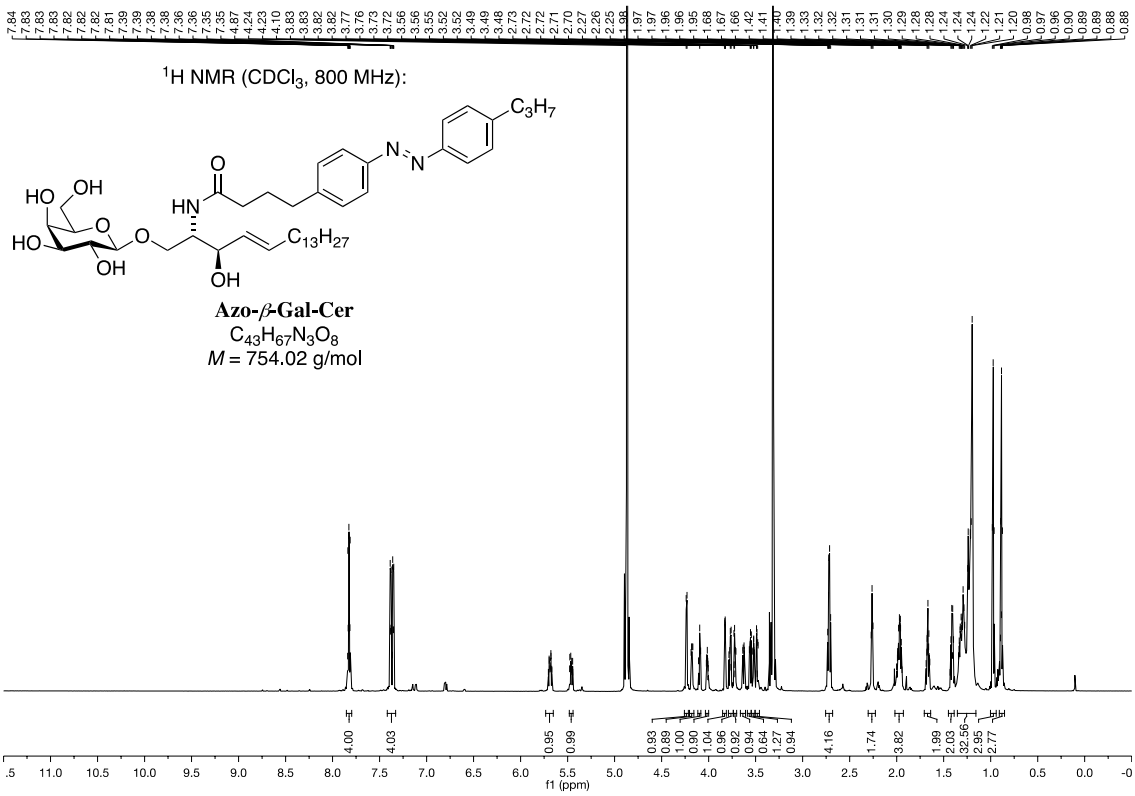

^{1}H NMR ($CDCl_3$, 800 MHz):

Azo-β-Gal-Cer
$C_{43}H_{67}N_3O_8$
M = 754.02 g/mol

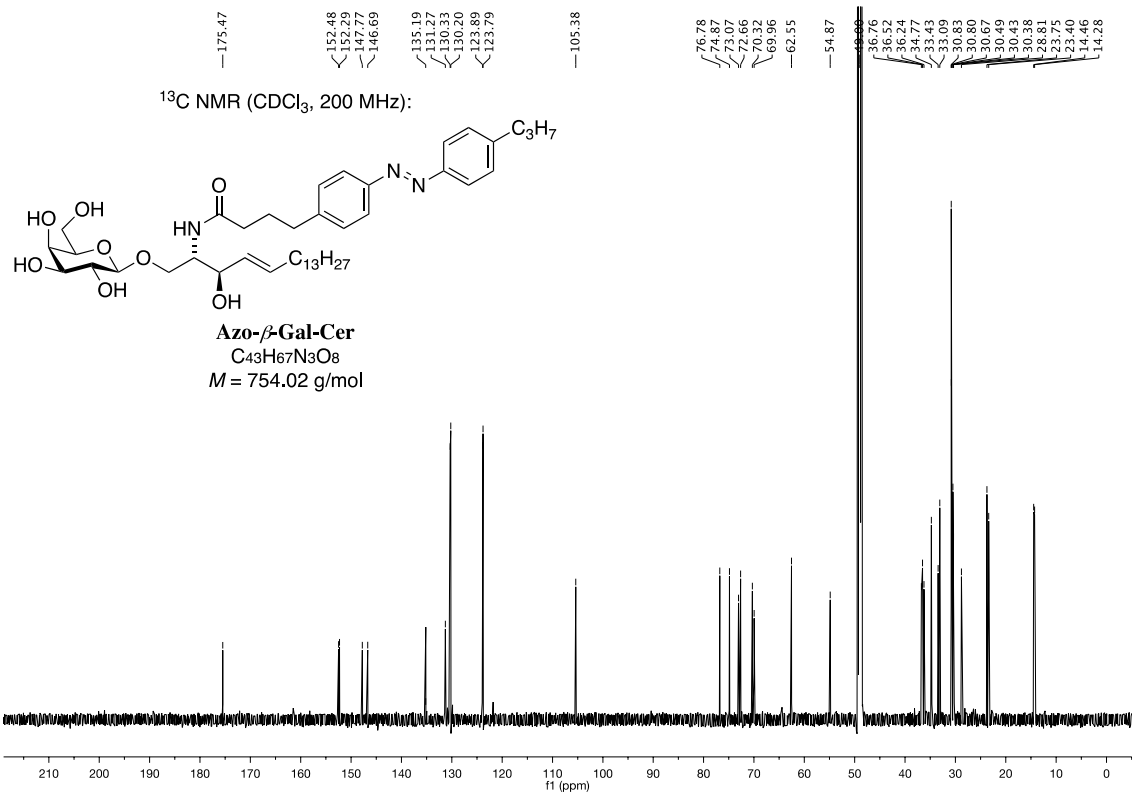

^{13}C NMR ($CDCl_3$, 200 MHz):

Azo-β-Gal-Cer
$C_{43}H_{67}N_3O_8$
M = 754.02 g/mol

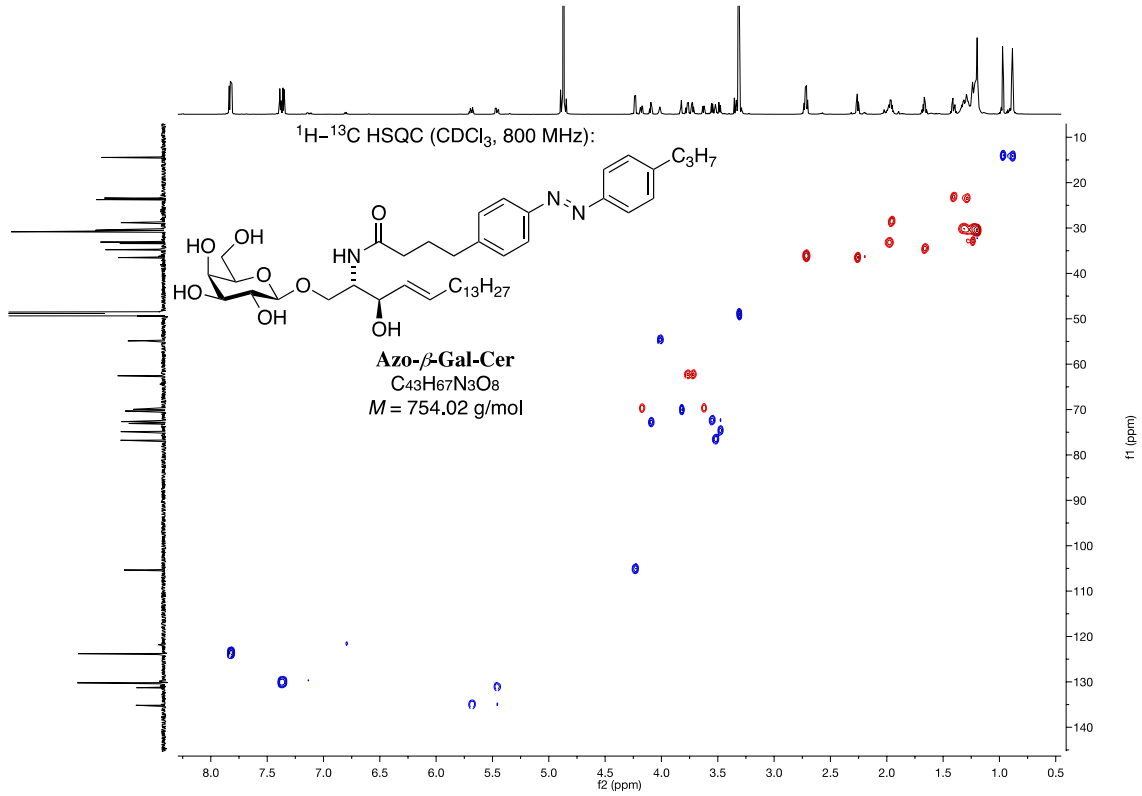
^{1}H–^{13}C HSQC ($CDCl_3$, 800 MHz):
C_3H_7
N
N
O
HN
HO
OH
O
HO
O
OH
$C_{13}H_{27}$
OH
Azo-β-Gal-Cer
$C_{43}H_{67}N_3O_8$
M = 754.02 g/mol
f2 (ppm)
f1 (ppm)

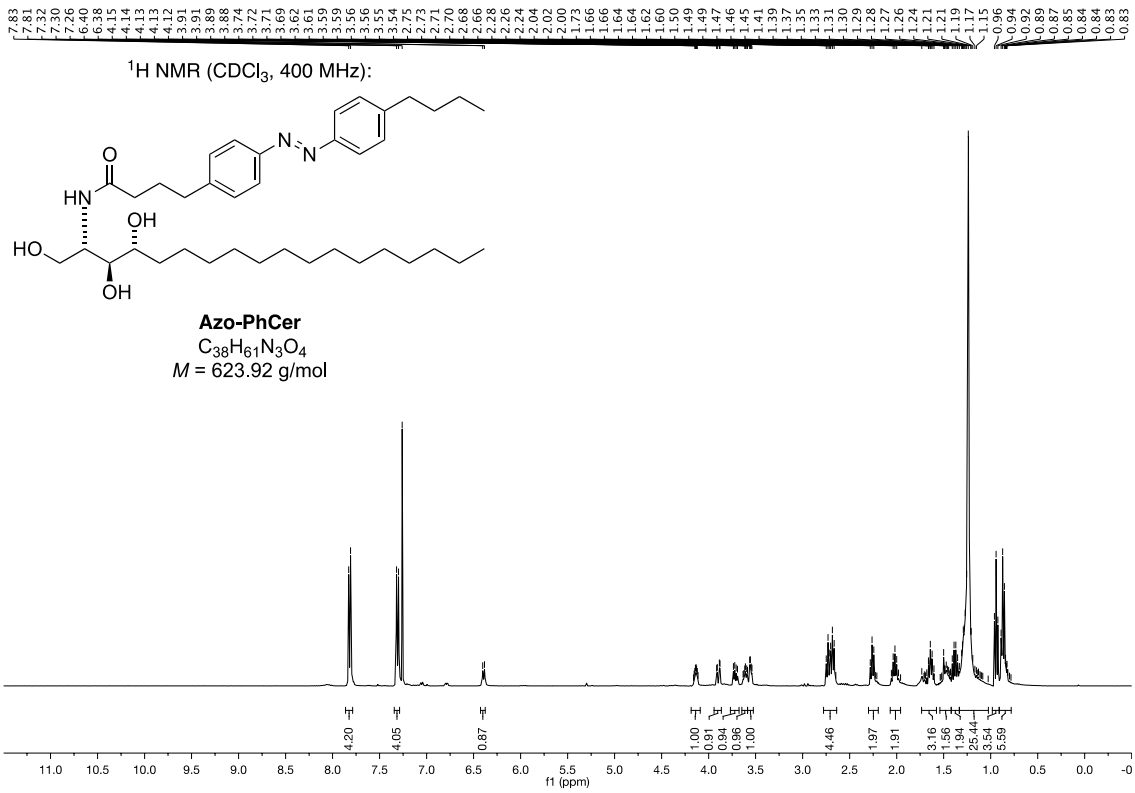
7.83 7.81 7.32 7.30 7.26 6.40 6.38 4.15 4.14 4.13 4.13 4.12 3.91 3.91 3.89 3.88 3.74 3.72 3.71 3.69 3.62 3.61 3.59 3.59 3.56 3.56 3.55 3.54 2.75 2.73 2.71 2.70 2.68 2.66 2.28 2.26 2.24 2.04 2.02 2.00 1.73 1.66 1.66 1.64 1.64 1.62 1.60 1.50 1.49 1.49 1.47 1.46 1.45 1.41 1.39 1.37 1.35 1.33 1.31 1.30 1.29 1.28 1.27 1.26 1.24 1.21 1.21 1.19 1.17 1.15 0.96 0.94 0.92 0.89 0.87 0.85 0.84 0.84 0.83 0.83
^{1}H NMR ($CDCl_3$, 400 MHz):
HO
HN
O
OH
OH
N
N
Azo-PhCer
$C_{38}H_{61}N_3O_4$
M = 623.92 g/mol
4.20 4.05 0.87 1.00 0.91 0.94 0.96 1.00 4.46 1.97 1.91 3.16 1.56 1.94 25.44 3.54 5.59
11.0 10.5 10.0 9.5 9.0 8.5 8.0 7.5 7.0 6.5 6.0 5.5 5.0 4.5 4.0 3.5 3.0 2.5 2.0 1.5 1.0 0.5 0.0 -0
f1 (ppm)

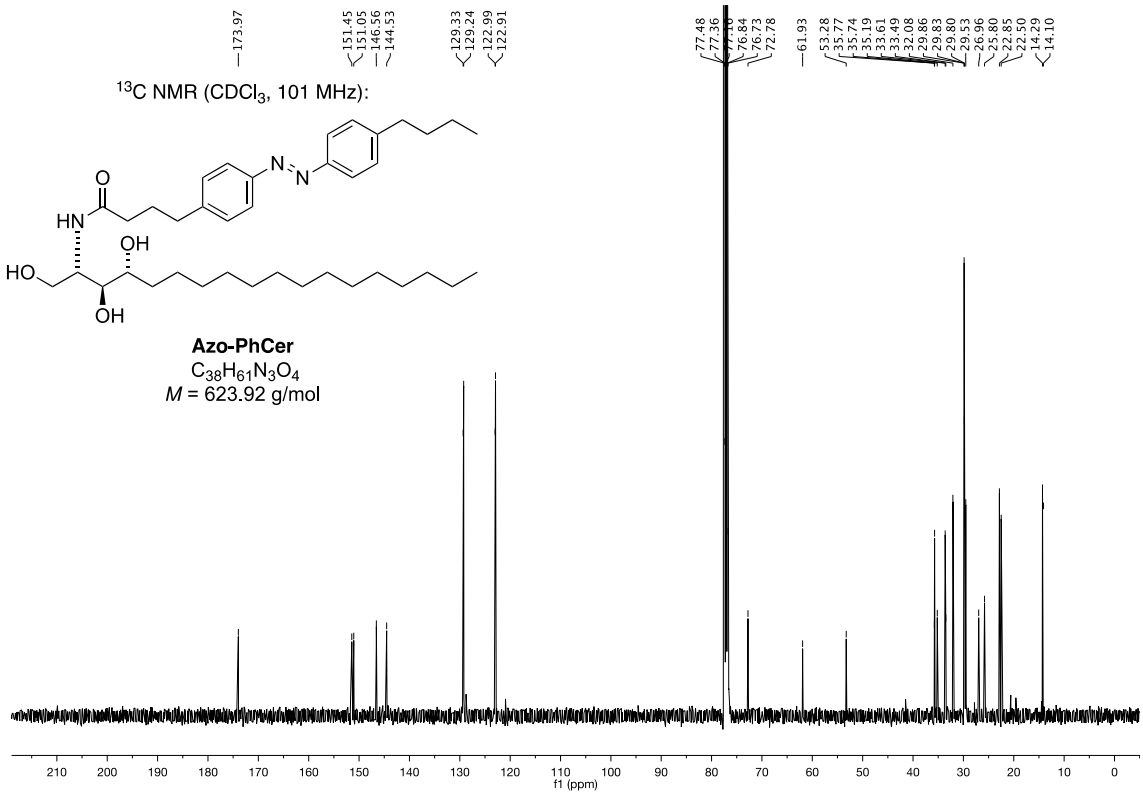
173.97
151.45 151.05 146.56 144.53
129.33 129.24 122.99 122.91
77.48 77.36 77.00 76.84 76.73 72.78
61.93
53.28 35.77 35.74 35.19 33.61 33.49 32.08 29.86 29.83 29.80 29.53 26.96 25.80 22.85 22.50 14.29 14.10
^{13}C NMR ($CDCl_3$, 101 MHz):
HO
HN
O
OH
OH
N
N
Azo-PhCer
$C_{38}H_{61}N_3O_4$
M = 623.92 g/mol
210 200 190 180 170 160 150 140 130 120 110 100 90 80 70 60 50 40 30 20 10 0
f1 (ppm)